ASSESSING THE IMPACT ON HYDROCARBON PRODUCTION FROM TIGHT AND SHALE PLAYS BY DEPLETION AND INJECTION USING THERMODYNAMIC AND TRANSPORT PROPERTIES FROM CONFINED SPACES

A Dissertation

by

TIANYING JIN

Submitted to the Office of Graduate and Professional Studies of
Texas A&M University
in partial fulfillment of the requirements for the degree of

DOCTOR OF PHILOSOPHY

Chair of Committee,	Maria A. Barrufet
Committee Members,	John Killough
	Alfred Daniel Hill
	Yuefeng Sun
Head of Department,	Jeff Spath

May 2021

Major Subject: Petroleum Engineering

ABSTRACT

Unconventional shale and tight reservoirs have contributed over a half of oil and gas of total U.S. production these years. As well known, phase behavior of the fluid in unconventional reservoir is quite different from that in conventional reservoir. And the variation of the thermodynamic and transport properties of fluids has a significant impact on the well performance and ultimate recovery of unconventional reservoirs. Therefore, an effective and reliable method to investigate and predict the impact of confinement on well performance and ultimate recovery of unconventional reservoirs is necessary and of great importance. In this study, a mechanistic model of both depletion and injection for well performance prediction of unconventional reservoirs was developed, incorporating capillary pressure and pore size distribution, to provide a comprehensive approach to simulate the effect of confinement in unconventional reservoirs. With the developed mechanistic model, fluid model and pore size distribution models, a series of sensitivity analysis were conducted to investigate the impact of the variables including: capillary pressure, production modes, pore size distribution, pressure decline steps, wettability angle, injection dose per step, bottom-hole pressure (BHP) and injection fluid distribution. The developed mechanistic model gives a rapid prediction and estimation of the production performance especially for unconventional reservoirs by incorporating the capillary pressure and pore size distribution. It also can predict the production performance changing with different operation conditions, which is of vital importance in the field operation to optimize production. Furthermore, this mechanistic model provides

the best and the worst extreme boundaries of the production performance, and two different injection fluid distribution models, which can be used as a guidance for other reservoir simulation methods.

ACKNOWLEDGEMENTS

I would like to express my greatest acknowledgements to my supervisor Dr. Maria A. Barrufet. She offered me great help and I will always remember her as the best mentor. Also, thanks to her encouragement and patience which greatly impacted my life.

Thanks to Dr. John Killough, Dr. Alfred Daniel Hill, and Dr. Yuefeng Sun for providing valuable advice. Thanks also go to the research program provided by Marathon Oil Company, for providing the financial support for this study.

I also appreciate my research group team members: Jingwei Huang, Bartosz T. Czernia, Gonzalo Hernandez, Xiaona Cui, and Zheng Sun for the valuable discussions and good time together during my PhD.

Thanks to my husband, Dr. Yue Zhou, and my daughter, Yolanda Zhou, who support me through ups and downs during my PhD. Thanks to my family and friends for all support and love for me.

CONTRIBUTORS AND FUNDING SOURCES

Contributors

This work was supported by a dissertation committee consisting of Professor Maria A. Barrufet from Petroleum Engineering Department, Dr. John Killough and Dr. Alfred Daniel Hill from Petroleum Engineering Department, and Dr. Yuefeng Sun from Department of Geology and Geophysics. All work for the dissertation was completed independently by the student.

Funding Sources

Great thanks to the financial support from Marathon Oil Company.

NOMENCLATURE

a^l	attraction parameter of liquid phase
b^l	van der Waals co-volume of liquid phase
f_v	Molar fraction of the vapor phase
f_i^v	fugacity of component i in vapor phase
f_i^l	fugacity of component i in liquid phase
k_{ij}	Binary coefficient between component i and j
k_{ro}	Oil relative permeability
k_{rg}	Gas relative permeability
K_i	Equilibrium constant for component i
Mw_i	Molecular weight of component i
n_c	Number of components
p^l	Pressure of liquid phase
p^v	Pressure of vapor phase
$p_{c,i}$	Critical pressure for each component i
P_c	Capillary pressure
P_i	Parachor of component i
R	Universal gas constant
r	Radii of curvature
S_o^*	Normalized oil saturation

S_o	Oil saturation
S_{oi}	Irreducible oil saturation
s_i	Dimensionless shift parameter for each component i
T	Temperature
$T_{c,i}$	Critical temperature for each component i
V_{dep_oil}	Volume of depleted oil
V_{dep_gas}	Volume of depleted gas
V_{excess}	Excess volume
V_m^l	Molar volume of liquid phase
x_i	Mole fraction of the i-th component in the liquid phase
y_i	Mole fraction of the i-th component in the gas phase
z_i	Mole fraction of the i-th component in the mixture
Z^l	Compressibility
ω_i	Acentric factor
$\hat{\phi}_i^v$	Fugacity coefficient of component i in vapor phase of the mixture
$\hat{\phi}_i^l$	Fugacity coefficient of component i in liquid phase of the mixture
σ	Interfacial tension
σ_{std}	Standard deviation
θ	Oil-gas wettability angle
ϵ	Tolerance error for convergence
μ_l	Viscosity of liquid phase

μ^*	Viscosity of the mixture at atmospheric pressure
μ_{std}	mean
ρ_r	Reduced density
ξ_m	The mixture viscosity parameter
λ_o	Mobility of oil
λ_g	Mobility of gas
γ_i	Gravity for each component i
BHP	Bottom hole pressure
CC	Constant composition
CDF	cumulative distribution function
EOS	equation of state
GOR	Gas-oil ratio
LBC	Lohrenz, Bray and Clark coefficients
PDF	probability density function
PG	Preferential gas
PR	Peng-Robinson
QC	Quality control
RF	Recovery factor
RP	Relative permeability

TABLE OF CONTENTS

Page

LIST OF FIGURES

Page

LIST OF TABLES

Page

CHAPTER I

INTRODUCTION

With the technology breakthrough and wide application of hydraulic fracturing and horizontal drilling, the industry has made considerable efforts to produce gas and oil economically from unconventional shale and tight reservoirs in the past decades. These unconventional reservoirs generally have ultralow permeability (in the order of 1 to 100 nd) and extremely small pore throat sizes (a few nanometers to 100 nm) compared with conventional reservoirs. Such small pore sizes induce significant fluid phase behavior changes compared to conventional reservoirs due to confinement. As widely known, phase behavior and fluid properties play an important role in both upstream and downstream sections of the petroleum industry. The variation of the thermodynamic and transport properties of fluids has a significant impact on the well performance and ultimate recovery of unconventional reservoirs. Therefore, an effective and reliable method to investigate and predict the impact of confinement effect on well performance and ultimate recovery of unconventional reservoirs is necessary and of great importance.

Most of the recent studies on well performance for unconventional reservoirs are conducted using molecular simulation or compositional simulation, which is with a high computation cost. The approaches to model confinement effects are quite different. Three common approaches used are adsorption, capillary pressure model and critical shift model. Adsorption models have many assumptions which limit their application, and the required parameters depend on the experimental settings. Most common used critical shift models

are based on the observations for the pure components; however, the critical shift model for the mixtures has not been validated by experiments yet. To reduce the computation cost and to incorporate confinement effect with a reasonable model, a mechanistic model for well performance prediction of unconventional reservoir is developed in this study using capillary pressure models coupled with and EOS to predict phase equilibrium.

Although production from unconventional resources has achieved tremendous achievement in the U.S. and changed the whole world's energy blueprint in only a few years, most of the current primary production in tight oil reservoirs is still very low, within 4-10% depending on the specific formation properties and production completion techniques (Pankaj 2018; Hamdi 2018). To increase the oil recovery factor and reservoir energy, miscible fluid injection is expected to be a promising method. Hence, the mechanistic model developed in this study also includes the injection process modeling to investigate the impact of the confinement effect on the enhanced oil recovery (EOR) processes.

1.1 Objectives and Chapter Overview

The objectives of this work are as follows:

- Develop fluid models for a given fluid sample, which include quality control analysis for the given PVT data to check the uncertainties in the given report, and calibration of a reduced equation of state (EOS) to reduce the computational cost in reservoir simulation.
- Develop a mechanistic model of depletion for well performance prediction of unconventional reservoirs. The model considers confinement by incorporating capillary

pressure and pore size distribution. Thus, pore size distribution models for a reservoir sample need to be developed.

- Generate unique relative permeability curves using mechanistic model to provide a consistent and more realistic behavior.
- Develop the mechanistic model to simulate the injection for EOR prediction of unconventional reservoirs in confinement by incorporating capillary pressure and pore size distribution.
- Conduct a sensitivity analysis to investigate the impact of depletion variables used in the mechanistic model, such as effect of capillary pressure, production modes, pore size distribution and pressure decline steps to provide a comprehensive discussion on the impact of these variables.
- Conduct a sensitivity analysis to investigate the impact of the injection variables used in the mechanistic model, such as capillary pressure, production modes, pore size distribution, injection dose per step, bottom-hole pressure (BHP) and injection fluid distribution to provide a comprehensive discussion on the determination for the values of variables.
- Compare mechanisms with a commercial simulator or an in-house compositional simulator, build a bridge connecting the mechanistic model and the field-scale simulation. Thus, a comprehensive mechanistic model is to be develop for performance prediction in the field.

The organization of the dissertation is as follows:

The first chapter provides the general introduction for the background and areas of this study, lists the main objectives of this work, and gives a detailed review of the published works on impacts of confined space on hydrocarbon phase behavior, pore size distribution of unconventional reservoirs, enhanced oil recovery with gas injection for unconventional oil reservoirs; the second chapter introduces the methodology used in this study, including phase behavior model, pore size distribution implementation and generation of relative permeability curves; the third chapter describes the mechanistic model including the depletion process for well performance prediction of unconventional reservoir, and injection process for huff-n-puff EOR prediction of unconventional reservoirs; the fourth chapter gives a comprehensive procedure for fluid model and pore size distribution model development using experimental data; the fifth chapter conducts sensitivity analysis for both depletion and injection processes to investigate the impacts of the depletion variables, such as effect of capillary pressure, pore size distribution and pressure decline steps, and injection variables, such as pore size distribution, injection rate, bottom-hole pressure (BHP), injection fluid distribution and injection fluid composition; the sixth chapter provides a method to build the bridge connecting mechanistic model developed in this study to a field-scale simulation and prediction, as well as discussions on the assumption and application of this proposed method.

1.2. Literature Review

1.2.1 Impacts of Confined Space on Hydrocarbon Phase Behavior

Experimentally, fluid phase behavior in nanopores has been widely studied using adsorption/desorption measurements at constant temperature with several typical fluid-

adsorbent systems (Ball and Evans 1989; Thommes and Findenegg 1994; Zhu 1999; Carrott 2001; Thommes 2002; Qiao 2004; Kittaka et al. 2009; Russo 2012). Recently, approaches such as nanofluidic chips (Parsa et al. 2015; Alfi et al. 2016, 2017; Yang et al. 2019), differential scanning calorimetric (DSC) (Luo et al. 2016a, 2016b, 2018, 2019) have been developed to study the nano-confinement effect on hydrocarbons. The results of these experiments show that the boiling point and bubble point temperatures increase with a decrease in nanopore radius at atmospheric pressure.

Since the existing experiments are limited to low pressure or few components, the molecular-level approaches, such as molecular dynamics (MD) simulation (Walton and Quirke 1989; Singh et al. 2009; Wang et al. 2015; Jin and Nasrabadi 2016, 2017, 2018) and density function theory (DFT) (Peng and Yu 2008; Li et al. 2014; Jin and Firoozabadi 2016a; Liu et al. 2018) are applied in studying the confined fluid. The results from these molecular simulations confirmed the phase behaviors of both pure components and mixtures are greatly altered in the nanopores.

Theoretically, the fluid phase behavior in nanopores is governed by interactions of fluid-fluid and fluid-pore wall interactions within the confining geometry. The fluid-fluid interactions are well defined by the bulk-state thermodynamics, thus the evaluation of fluid-pore wall interaction along with the pore geometry is needed. Equations of state (EOS) are one of the most used and studied approaches in thermodynamic modeling and, in particular the PR EOS has accomplished tremendous success in modeling bulk-state fluid behavior. To model the confined fluid behavior, the EOS system requires the description of fluid-pore wall interaction. Some researchers proposed modification or

extension on the van der Waals EOS to model confined fluid phase behavior (Derouane 2007; Travalloni et al. 2010a, 2010b). Then some similar studies on the extension of the PR-EOS (Travalloni et al. 2014; Barbosa 2016; Dong et al. 2016; Luo et al. 2019). However, the parameters required by these models need to be determined from experiments. The fluid-pore wall interaction within the confining geometry has been studied with several theoretical approaches, such as adsorption model, critical shift model and capillary pressure model.

Langmuir adsorption isotherm (Langmuir 1918) is one of the easiest models for studying the effect of adsorption on phase behavior. However, Langmuir adsorption model assume a surface that is flawlessly flat and homogeneous with an ideal adsorbed gas monolayer at the considered temperature, and the adsorbed gas and surface are in equilibrium. Thus, Langmuir adsorption model is only applicable for single component adsorbate at lower temperature and lower pressures. Ambrose et al. (2010) applied the Langmuir adsorption isotherm to estimate gas in place in shale reservoirs considering a multicomponent reservoir fluid. They proposed an extended Langmuir model (ELM) to determine the composition and amounts of the adsorbed phase, and took the effect of volumetric/free gas into consideration based on the assumption including ideal-gas mixtures and the interactions between gas molecules are negligible. Jin and Firoozabadi (2016a) showed a comparison between the results from ELM and the measured data. The ELM showed good agreement for methane but significantly underestimated CO_2 and N_2 fluid content. Thus, adsorption models are only applicable to some components and situations.

Evans and Tarazona (1986) proposed that the critical properties are altered in small pores. The critical temperature of a confined fluid is generally lower than the bulk critical temperature and approaches the bulk value in large pores. Zarragoicoechea and Kuz (2004) derived an equation for the shift in the critical temperature under confinement from a generalized van der Waals EOS characterized only by the Lennard-Jones size parameter. Many studies applied the shifted critical temperature and pressure from Singh et al. (2009) to the conventional EOS to estimate fluid phase behavior in nanopores (Devegowda et al. 2012; Alharthy et al. 2013; Jin et al. 2013; Zhang et al. 2013). However, their correlations cannot be reduced to the bulk phase if the porous medium is removed. In addition, the calculated bubble-point pressure can be higher or lower than those in the bulk, whereas the dew-point pressure is lower than those in the bulk phase, which contradicts the observation from experimental data.

Capillary pressure is the difference in pressure between two phases across a curved interface at equilibrium. Curvature of the interface is the consequence of preferential wetting of the capillary walls to the fluid phases. Brusllovsky (1992) studied the effect of capillary pressure on phase equilibrium of a multicomponent system by use of a thermodynamic model. He measured the dew-point and bubble-point pressures in the presence of small pores for different values of pore radius at a given temperature, and reported that the surface curvature and dew-point pressure increased while the bubble-point pressure decreased as the pores became smaller. He also found that in porous media with varying pore sizes, the bubble-point pressure is reached first in the larger pores whereas the dew-point pressure occurs first in smaller pores. Wang et al. (2013) developed

a tight oil compositional simulator that models the effect of capillary pressure in nanopores on fluid properties using the Peng-Robinson equation of state and Leverett J-function. But their simulator appears to only be applicable to a particular type of rock. Xiong et al. (2015) also proposed a coupled method using the Leverett-J-function to include capillary pressure. This method updated interfacial tension (IFT) based on composition but did not include pore diameter. Young-Laplace equation is a widely used model to describe capillary pressure (Nojabaei et al. 2013; Stimpson and Barrufet 2016a, 2016b). Nojabaei et al. (2013) numerically modeled the capillary pressure effect on phase behavior for several binary mixtures and Bakken reservoir oil. They evaluated capillary pressure by Young-Laplace equation with Macleod-Sugden correlation of IFT calculation. They concluded that by considering the effect of capillary pressure caused by small pores, bubble-point pressure decreases and there is either a decrease or increase in dew-point pressure, depending on the location on the phase envelope. Stimpson and Barrufet (2016a) proposed a fast-mechanistic approach for estimating phase boundaries and fluid properties of pure substances in a single pore, or collection of uniform pores. They use Young-Laplace equation and Weinaug and Katz parachor method to calculate the capillary pressure and IFT. This method showed a decrease in saturation pressure and an increase in saturation temperature due to capillarity, consistent with experimental and molecular simulated data. Stimpson and Barrufet (2016b) then extended their work and proposed a fully coupled rigorous method for phase equilibrium calculations for use in compositional reservoir simulation. Results from modeling show changes in fluid behavior due to confinement, which may lead to higher oil production in the reservoir simulation.

In this study, a fully coupled rigorous method for phase equilibrium calculations for reservoir fluid in confined space proposed by Stimpson and Barrufet (2016a, 2016b) will be used to incorporated confinement effect by couple PR-EOS with capillary pressure. Young-Laplace equation and Weinaug and Katz parachor method were used to calculate the capillary pressure and IFT.

1.2.2 Pore Size Distribution (PSD) of Unconventional Reservoirs

Compared to conventional reservoirs, unconventional reservoirs have complex pore networks and distinct scales for fluid to flow, especially those in the kerogen pore space. Pore size distribution of porous media can be subdivided into three classes using International Union of Pure and Applied Chemistry (IUPAC) pore size (radius) classification standard, which are nanopores (<2 nm), mesopores (2-50 nm) and macropores (>50 nm). Bustin et al. (2008) presented a bimodal pore size distribution and suggested that small pore volume occurs in the 10 nm to 1000 nm range based on the results from a methodology referred as MARIO for the Barnett shale. Nelson (2009) described the pore size of different types of sedimentary rocks. The pore throats diameter of the shales and tight sandstones is around 1nm to 100nm, which is very small comparing to that of the sandstones.

Kuila and Prasad (2013) reported that the shale matrix is mainly composed of pores in the range of 2-50 nm and has a considerable percentage of pores less than 2 nm in diameter. And Pommer (2014) evaluated pore size distributions for samples collected from the Eagle Ford formation. Based on his experimental data, he found in most cases the pore sizes result in a lognormal distribution. Stimpson (2017), Czernia (2019) applied

lognormal distribution functions to model the pore size distribution for shale reservoirs and then selected a set of representative pore sizes for the study of confinement effects. In this study, lognormal distribution functions are used to model the pore size distribution for shale reservoirs and then to select a set of representative pore sizes for the study of confinement effects.

1.2.3 Enhanced Oil Recovery with Gas Injection for Unconventional Reservoirs

Ren et al. (2016) monitored on CO_2 migration in a tight oil reservoir during CCS-EOR (Carbon Capture and Storage-Enhanced Oil Recovery) in China which proved that CO_2 injection is a feasible method to improve oil recovery in tight oil reservoirs. Alfarge et al. (2017) reviewed many reports and studies to investigate the applicability of different EOR methods in unconventional formations of North America. Different methods have been used in the reviewed studies such as experimental investigations, numerical simulations, pilot tests and mathematical approaches. Their review showed that the most feasible EOR techniques for these unconventional reservoirs are miscible gases, surfactant, and low-salinity water flooding. Most of the previous studies recommended that miscible gas EOR is the best technique. The gases which have been investigated are CO_2, N_2 and natural gases. CO_2, surfactant, and natural gas are the most applicable EOR method, where CO_2 is in the top of the miscible gases EOR category to be applied in shale reservoirs because of high miscibility at low pressure. Pilot tests apparently approved success of natural gas due to its high compressibility and availability in the field. However, there is a clear gap between lab-works conclusions and pilot test performance for CO_2-EOR due to the misleading diffusion mechanism. And large mass of CO_2 is not always

available in the field. Thus CO_2-EOR for unconventional reservoir is still under investigate. Two common injection schemes are often used in the field for CO_2 injection: continuous CO_2 injection (CO_2 flooding) and CO_2 huff-n-puff. In the continuous CO_2 flooding, CO_2 is injected at the injector and oil is produced at the producer continuously. While in CO_2 huff-n-puff, one well goes through three stages: injection, soaking (shut-in) and production. In tight oil reservoirs, it is very challenging to determine the best injection-production strategy which depends on many uncertain parameters such as the fluid properties, formation porosity, permeability, and natural fractures distribution etc.

Experimentally, Li et al. (2018) studied four injection schemes, which are CO_2 continuous gas injection, gas injection and soaking, pulse injection, and injection-alternating-production, for high-temperature and pressure CO_2 immiscible flooding in low-permeability formations. They found that soaking is an important step for the CO_2-EOR at the immiscible conditions. And they also suggested a low injection rate for any CO_2 injection scheme in the low-permeability formations. Zhang et al. (2018) conducted experiments to investigate the potential of combining both CO_2 huff-n-puff and surfactant imbibition techniques to optimize oil recovery in unconventional liquid reservoirs of Eagle Ford. The results of their CO_2 injection experiments demonstrated that CO_2-EOR in unconventional liquid reservoir through a hydraulic fracture could lead to high recovery of the oil in the rock matrix and the recovery factors will increase as the experimental pressure of CO_2 huff-n-puff experiments increase.

Numerically, Yu et al. (2015) built a reservoir model by including multiple hydraulic fractures for the Bakken formation to simulate the CO_2 huff-n-puff process and

concluded that the CO_2 molecular diffusion effect is an important physical mechanism to improve oil recovery in the formation with low permeability. Pu et al. (2016) introduced a new model which considers capillarity and adsorption of the small pores for shale reservoirs. They found that model with capillarity would predict higher oil recovery by CO_2 injection than that without capillarity. Zuloaga et al. (2017) performed CO_2 injection numerical simulations in the Bakken formation and tested the feasibility of CO_2 flooding and huff-n-puff process. They found that there exists a threshold value of the matrix permeability that determines whether the CO_2 huff-n-puff or flooding is more favorable: CO_2 huff-n-puff process achieves higher oil recovery when the matrix permeability is lower than 0.03 mD. They also found that the presence of natural fractures has more important impact during CO_2 huff-n-puff process with a low matrix permeability. Alfarge, Wei and Bai (2018) combined numerical simulation methods with the production data analysis of field data to investigate the more dominated mechanisms to control CO_2-EOR performance in huff-n-puff operations in conventional reservoirs versus unconventional formations. They found that the molecular diffusion mechanism is the main mechanism controlling performance of CO_2-EOR huff-n-puff process in shale oil formations. Lino et al. (2018) presented a rapid and efficient approach for optimization of CO_2 and gas injection EOR in unconventional reservoirs using the Fast Marching Method (FMM)-based flow simulation. The optimization using their simulation can quickly assist designing and evaluating the huff-n-puff EOR in unconventional reservoirs in several hours. Tian et al. (2019) presented a general compositional model for gas injection EOR to investigate the complex multiphase and multicomponent behaviors under coupled

nanopore confinement and geomechanics in tight oil reservoir. Their simulation revealed that huff-n-puff would improve the recovery factor of each component versus the depletion. Considering the nanopore confinement in the simulation will reduce the light component recovery factor but increase the heavy component recovery factor after huff-n-puff.

Most of the simulation studies are using numerical simulation with field data history matching. For such simulation studies including reservoir heterogeneity and complex fracture geometry, compositional simulation is a powerful and versatile tool because of the capability to incorporate multi-phase and multi-component effects in nano-porous rocks. However, flow simulation accounting for such complex physics can be computationally expensive. Although Fast Marching Method (FMM) can significantly reduce the computation time which is still several hours for a 2000'×2800'×150'reservoir gridded using Cartesian cells of 400×560×5 (total 1,120,000) with 20 hydraulic fractures. Thus, a rapid and efficient approach for optimization of CO_2 injection EOR in unconventional reservoirs is desired.

CHAPTER II

METHODOLOGY

2.1. Vapor-Liquid Equilibrium Model

The volumetric behavior of multi-component systems is described by equations of state (EOS). Peng-Robinson EOS (Peng and Robinson, 1976) and the Soave RK EOS (Soave, 1972) are, by far, the most widely used cubic EOS used in petroleum engineering. Peng-Robinson (PR) EOS shown below solving for the pressure of phase $\mathcal{L}$, which can be either liquid or vapor is used in this study.

$$p^{\mathcal{L}} = \frac{RT}{V_m^{\mathcal{L}} - b^{\mathcal{L}}} - \frac{a^{\mathcal{L}}}{V_m^{\mathcal{L}}\left(V_m^{\mathcal{L}} + b^{\mathcal{L}}\right) + b^{\mathcal{L}}\left(V_m^{\mathcal{L}} - b^{\mathcal{L}}\right)} \tag{2.1}$$

Where, a is a parameter that takes intermolecular attraction forces into account, and b also known as co-volume, takes repulsion forces into account, for each individual component are calculated using following equations.

$$a_i = 0.45724 \frac{R^2 T_{c,i}^2}{p_{c,i}} \alpha_i \tag{2.2}$$

$$b_i = 0.0778 \frac{RT_{c,i}}{p_{c,i}} \tag{2.3}$$

The value of α for component i is calculated using Eq. 2.4 or Eq. 2.5 depending on the acentric factor of that component. The acentric factor takes the non-sphericity of molecules into account.

$$\alpha_i = \left(1 + (0.374640 + 1.54226\omega_i - 0.26992\omega_i^2)\left(1 - \sqrt{\frac{T}{T_{c,i}}}\right)\right)^2, \quad if \ \ \omega_i \leq 0.49 \tag{2.4}$$

$$\alpha_i = \left(1 + (0.379642 + 1.48503\omega_i - 0.164423\omega_i^2 + 0.016666\omega_i^3)\left(1 - \sqrt{\frac{T}{T_{c,i}}}\right)\right)^2, if\omega_i > 0.49 \tag{2.5}$$

When working with a multi-component mixture, the attraction parameter and co-volume for the phase $\mathcal{L}$ of the mixture are calculated using the mixing rules in the following equations:

$$a^{\mathcal{L}} = \sum_i^{n_c}\sum_j^{n_c} c_i c_j (1 - k_{ij})\sqrt{a_i a_j} \tag{2.6}$$

$$b^{\mathcal{L}} = \sum_{i=1}^{n_c} c_i b_i \tag{2.7}$$

Several studies have shown that all cubic EOS's can be represented by single general formulations. One of the most useful generalized formulations is the one presented by Coats (1985), which is shown below.

$$(Z^{\mathcal{L}})^3 + (1 - B^{\mathcal{L}})(Z^{\mathcal{L}})^2 + [A^{\mathcal{L}} - 3(B^{\mathcal{L}})^2 - 2B^{\mathcal{L}}]Z^{\mathcal{L}} - [A^{\mathcal{L}}B^{\mathcal{L}} - (B^{\mathcal{L}})^2 - (B^{\mathcal{L}})^3] = 0 \tag{2.8}$$

Where,

$$A^{\mathcal{L}} = \frac{a^{\mathcal{L}} p^{\mathcal{L}}}{(RT)^2} \tag{2.9}$$

$$B^{\mathcal{L}} = \frac{b^{\mathcal{L}} p^{\mathcal{L}}}{RT} \tag{2.10}$$

The equilibrium constant (K_i) play a key role during two-phase splitting prediction problems. The equilibrium constant, K_i, is defined as the ratio of the mole fraction of the i-th component in the gas phase (y_i) to the mole fraction of the same component in the liquid phase (x_i), which is shown below.

$$K_i = \frac{y_i}{x_i} \tag{2.11}$$

From a molar material balance applied to a two-phase system in equilibrium and the definition of K_i, we can derive the following expression [49]:

$$g(f_v) = \sum_{i=1}^{n_c} \frac{z_i(K_i - 1)}{1 + f_v(K_i - 1)} = 0 \tag{2.12}$$

Eq. 2.12 is widely used and known as the Rachford-Rice Objective Function. Note that if all the $K_i's$ values were known, the only unknown left to solve for is f_v. And Wilsons's correlation is used to get the initial estimation of Ki-values as following:

$$K_i = \frac{1}{p_{ri}} exp\left[5.37(1 + \omega_i)\left(1 - \frac{1}{T_{r,i}}\right)\right] \tag{2.13}$$

As mentioned in the previous section, reliable values for the equilibrium constants ($K_i's$) must be obtained before we can solve the Rachford-Rice Objective Function. For a system to be in equilibrium, any mass net transfer must be zero. For this, all the chemical potentials for each component must be the same in all the phases. Therefore, the temperature and pressure of both phases are the same and a zero-net transfer for all

components in the mixture results when all chemical potential are the same. This is the thermodynamic phase equilibrium equation is written as:

$$f_i^v = f_i^l \qquad for\ i = 1, \dots, n_c \tag{2.14}$$

Since "fugacity" is a measure of the potential for transfer of a component between two phases, equal fugacities of a component in both phases results in a zero-net transfer. The fugacity coefficient is defined as the ratio of the fugacity of a material to its partial pressure. For a two-phase system which consists of n_c -components, the fugacity coefficient of component i for both vapor and liquid phases can be written, respectively, as:

$$\hat{\phi}_i^v = \frac{f_i^v}{y_i p^v} (i = 1,2, \dots, n_c) \tag{2.15}$$

$$\hat{\phi}_i^l = \frac{f_i^l}{x_i p^l} (i = 1,2, \dots, n_c) \tag{2.16}$$

For the case of the Peng Robinson cubic EOS, the fugacity coefficient of the component i in a mixture is given by:

$$\ln \hat{\phi}_i^{\mathcal{L}} = -\ln\left(Z^{\mathcal{L}} - B^{\mathcal{L}}\right) + \frac{A^{\mathcal{L}}}{2\sqrt{2}B^{\mathcal{L}}}\left(\frac{2\sum_{j=1}^{n_c} c_j(1-k_{ij})\sqrt{a_i a_j}}{a^{\mathcal{L}}} - \frac{b_i}{b^l}\right)\ln\left[\frac{Z^{\mathcal{L}}+(1+\sqrt{2})B^{\mathcal{L}}}{Z^{\mathcal{L}}+(1-\sqrt{2})B^{\mathcal{L}}}\right] + \frac{b_i}{b^l}\left(Z^{\mathcal{L}} - 1\right) \tag{2.17}$$

Since liquid molar volumes calculated using the PR EOS were not as accurate, Peneloux et al. (1982) proposed a volume translation, which was applied after VLE has been solved since the change in volume does not affect phase boundaries and the phase compositions obtained from VLE computations for a specified condition. The volume translation coefficient is computed using the following equation.

$$\tilde{V}_m^l = V_m^{l\,EOS} - \sum_{i=1}^{n_c} \left(x_i^l s_i b_i\right) \tag{2.18}$$

Where, s_i is the dimensionless shift parameter for each component i, estimated by the correlations with Rackett compressibility factor (Pedersen and Thomassen, 1989).

Young and Laplace (1805) proposed a quantitively description of the capillary pressure equation dependent on interfacial tension (IFT) and principal radii of curvature, which is shown in the following equations:

$$P_c = p^v - p^l = \frac{2\sigma \cos\theta}{r} \tag{2.19}$$

The interfacial tension is calculated with Weinaug and Katz (1959) parachor model as follows:

$$\sigma^{1/4} = \sum_{i=1}^{n_c} P_i \left(\frac{x_i}{\tilde{V}_m^l} - \frac{y_i}{\tilde{V}_m^v}\right) \tag{2.20}$$

Where, P_i is the parachor of each component, whose values are estimated based on the known parachors of the pure components and correlations for pseudo-components (Schechter and Guo, 1998).

To incorporate capillary pressure into flash calculation, a rigorous methodology proposed by Stimpson and Barrufet (2016) was applied. In their method, capillary pressure is updated within each loop, parallel to the calculation of fugacity. Flash calculation is first conducted with an initial guess of capillary pressure, $P_c^{old,n}$, which is zero usually for first loop. With calculated $x_i, y_i, \tilde{V}_m^l, \tilde{V}_m^v$, a new capillary pressure, $P_c^{new,n}$, can be obtained in

current loop. And capillary pressure used for next loop will be updated by the following equation:

$$P_c^{old,n+1} = 0.5\left(P_c^{old,n} + P_c^{new,n}\right) \tag{2.21}$$

This is a slow method which can be updated using any numerical technique. A convergence criterion is needed to determine the equilibrium:

$$\left|P_c^{old,n} - P_c^{new,n}\right| < \epsilon \tag{2.22}$$

A general flow chart of the VLE calculation of PR EOS coupled with capillary pressure is shown in **Fig. 1**.

To calculate the mobility of each phase in the system, viscosities of each phases are needed. Lohrenz, Bray and Clark (1964) proposed an empirical correlation for the prediction of the viscosity of a hydrocarbon mixture from its composition with five coefficients, $LBC_1\ to\ LBC_5$, which is used for viscosity calculation for both phases in this study. The equation is shown below:

$$\mu_l = \mu^* + \xi_m^{-1}[(LBC_1 + LBC_2\rho_r + LBC_3\rho_r^2 - LBC_4\rho_r^3 + LBC_5\rho_r^4)^4 - 10^{-4}] \tag{2.23}$$

where, μ^* represents the viscosity of the mixture at atmospheric pressure, ρ_r represents reduced density, and ξ_m represents the mixture viscosity parameter.

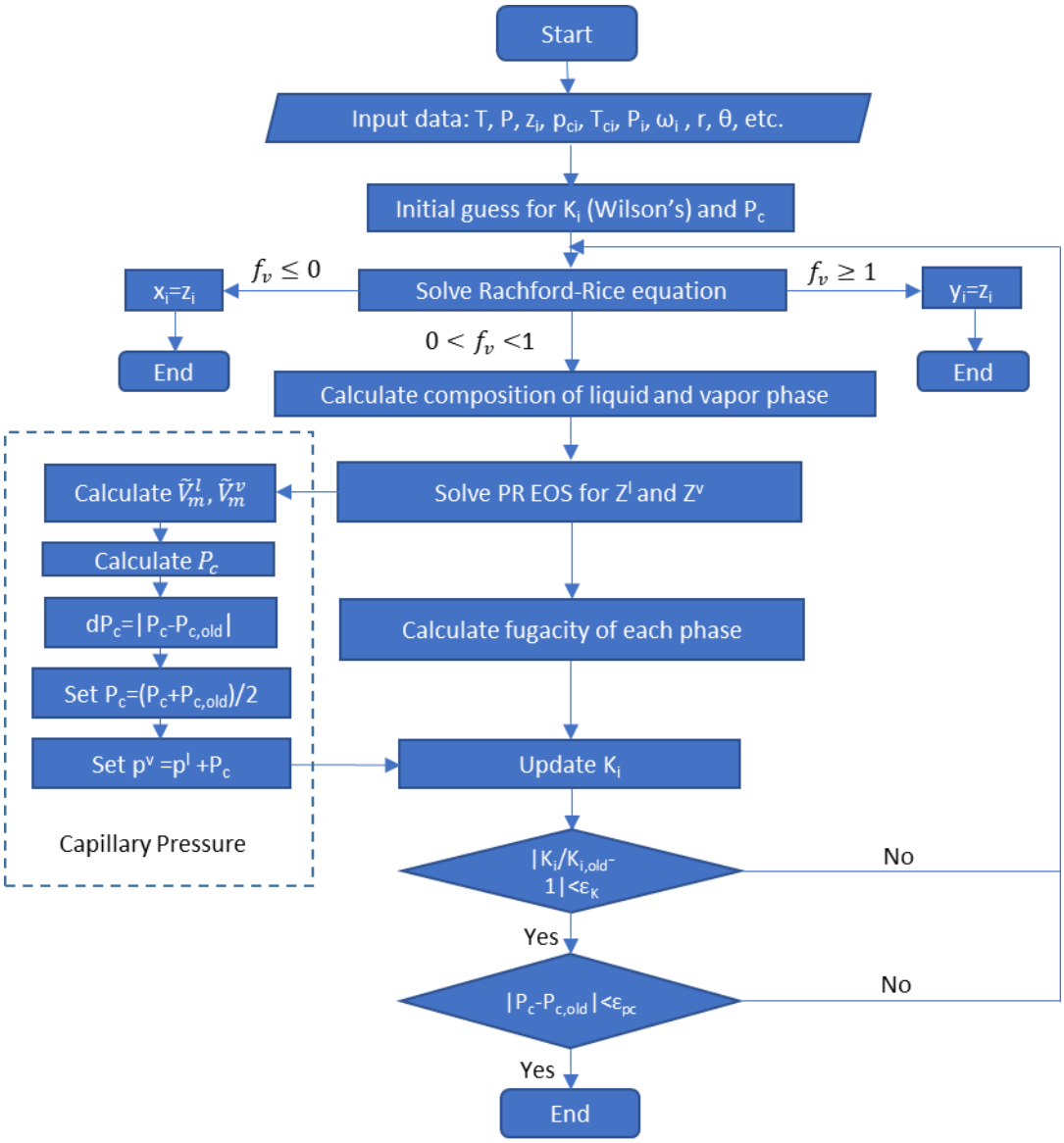

Fig. 1 Flow chart of VLE calculation of PR EOS coupled with P_c (adapted from Stimpson, 2016)

2.2. Pore Size Distribution Function

To model the phase behavior and production performance for a specific unconventional reservoir with given pore size distribution data for a rock sample, the pore size distribution function is needed to obtain a mathematical expression of the pore size

distribution. Based on the work of Pommer (2014) which evaluated pore size distributions from multiple Eagle Ford core samples, it is found that in most cases the pore sizes resulted in a lognormal distribution. For a lognormal distribution which is defined as a data set has a normal distribution of the natural logarithms, the probability density function is defined as follows, with a mean value, μ_{std}, and a standard deviation for the data set, σ_{std}.

$$PDF = \frac{1}{x}\frac{1}{\sigma_{std}\sqrt{2\pi}}\exp\left(-\frac{(\ln x - \mu_{std})^2}{2\sigma_{std}^2}\right) \tag{2.24}$$

The cumulative distribution function for a lognormal distribution is expressed as follows:

$$CDF = \frac{1}{2}\left[1 + \text{erf}\left(\frac{\ln x - \mu_{std}}{\sigma_{std}\sqrt{2}}\right)\right] \tag{2.25}$$

To obtain a mathematical expression of the pore size distribution, cumulative and incremental pore volume fraction are calculated using experimental data and the given pore volume of the samples. Next a cumulative distribution function of lognormal distribution is fitted to the data to obtain the mean (μ_{std}) and standard deviation (σ_{std}). Finally, the incremental pore volume fraction distribution is calculated using the fitted model.

2.3. Generation of Relative Permeability Curves

To model oil production performance under realistic condition, relative permeability curves for the specific fluid and condition are needed. In the oil and gas industry, reservoir simulation often uses relative permeability curves that are frequently obtained by history matching the production which do not or have no relation to capillary pressures. In this work, we will derive the permeability curves from the capillary pressure.

Here, the generation of relative permeability curves relies on the integration of capillary pressure data and is based on the work of Nakornthap and Evans (1986), Stimpson and Barrufet (2017) Czernia and Barrufet (2019). The relative permeability curves for the oil and gas phase are calculated using the following equations.

$$k_{ro}(S_o^*) = (S_o^*)^2 \frac{\int_0^{S_o^*} \frac{1}{P_c^2} dS_o^*}{\int_0^1 \frac{1}{P_c^2} dS_o^*} \tag{2.26}$$

$$k_{rg}(S_o^*) = (1 - S_o^*)^2 \frac{\int_{S_o^*}^1 \frac{1}{P_c^2} dS_o^*}{\int_0^1 \frac{1}{P_c^2} dS_o^*} \tag{2.27}$$

The integrations are based on normalized oil saturation as defined by Eq. 2.28, which by definition has a range of 0 to 1. The normalized oil saturation has a value of zero at the irreducible oil saturation, $S_{o,min}$.

$$S_o^* = \frac{S_o - S_{o,min}}{1 - S_{o,min}} \tag{2.28}$$

CHAPTER III

GENERAL DESCRIPTION OF MECHANISTIC MODEL

3.1. Mechanistic Model for Depletion

The mechanistic model for depletion is to simulate a constant volume depletion process incorporating pore size distribution, by coupling PR-EOS with capillary pressure, and different production modes which will be described later. For a specific pressure drop, the volume of the fluid in the pore will expand. Since the total volume of the pores is assumed to be a constant, the excess volume is being produced. The volumetric and phase equilibrium relations for each pore size are evaluated with VLE model coupled with capillary pressure. From these, the excess volume, gas and liquid densities and compositions are evaluated as the excess volume is specified according to the three production modes: constant composition (CC), relative permeability (RP), and preferential gas (PG). The constant composition production mode assumes the total molar composition within the pore remains constant, which means saturation of produced volume is equal to saturation of remaining volume in the pore. This is the most optimistic or highest expected production boundary. The volumes of oil and gas depleted are functions of excess volume and the oil saturation in the pore, which are shown in the following equations. And the saturation of the remaining fluid in the pores is the same as the saturation of the produced fluid.

$$V_{dep\_oil} = V_{excess} S_o \tag{3.1}$$

$$V_{dep\_gas} = V_{excess}(1 - S_o) \tag{3.2}$$

The preferential gas production mode is based on the assumption that the gas will be depleted first. Only the gas phase will be depleted if the gas volume is greater than the excess volume, otherwise, oil will be depleted to make up the remaining of the excess volume. This is the most conservative or pessimistic production boundary.

The relative permeability production mode is used to simulate actual production from an oil reservoir, which is also the mode between two production boundaries, CC and PG. The volumes of oil and gas depleted are functions of excess volume and the mobility (λ) of each phase in the pore. The definition of the mobility and equations to calculate depleted oil and gas volumes are shown below.

$$\lambda_o = \frac{k_{ro}}{\mu_o} \tag{3.3}$$

$$\lambda_g = \frac{k_{rg}}{\mu_g} \tag{3.4}$$

$$V_{dep\_oil} = V_{excess} \frac{\lambda_o}{\lambda_o + \lambda_g} \tag{3.5}$$

$$V_{dep\_gas} = V_{excess} \frac{\lambda_g}{\lambda_o + \lambda_g} \tag{3.6}$$

The relative permeability curves can either be directly specified or be calculated from capillary pressure data using relative permeability generation method mentioned before. The general flow chart of the mechanistic model for depletion process is shown in **Fig. 2**.

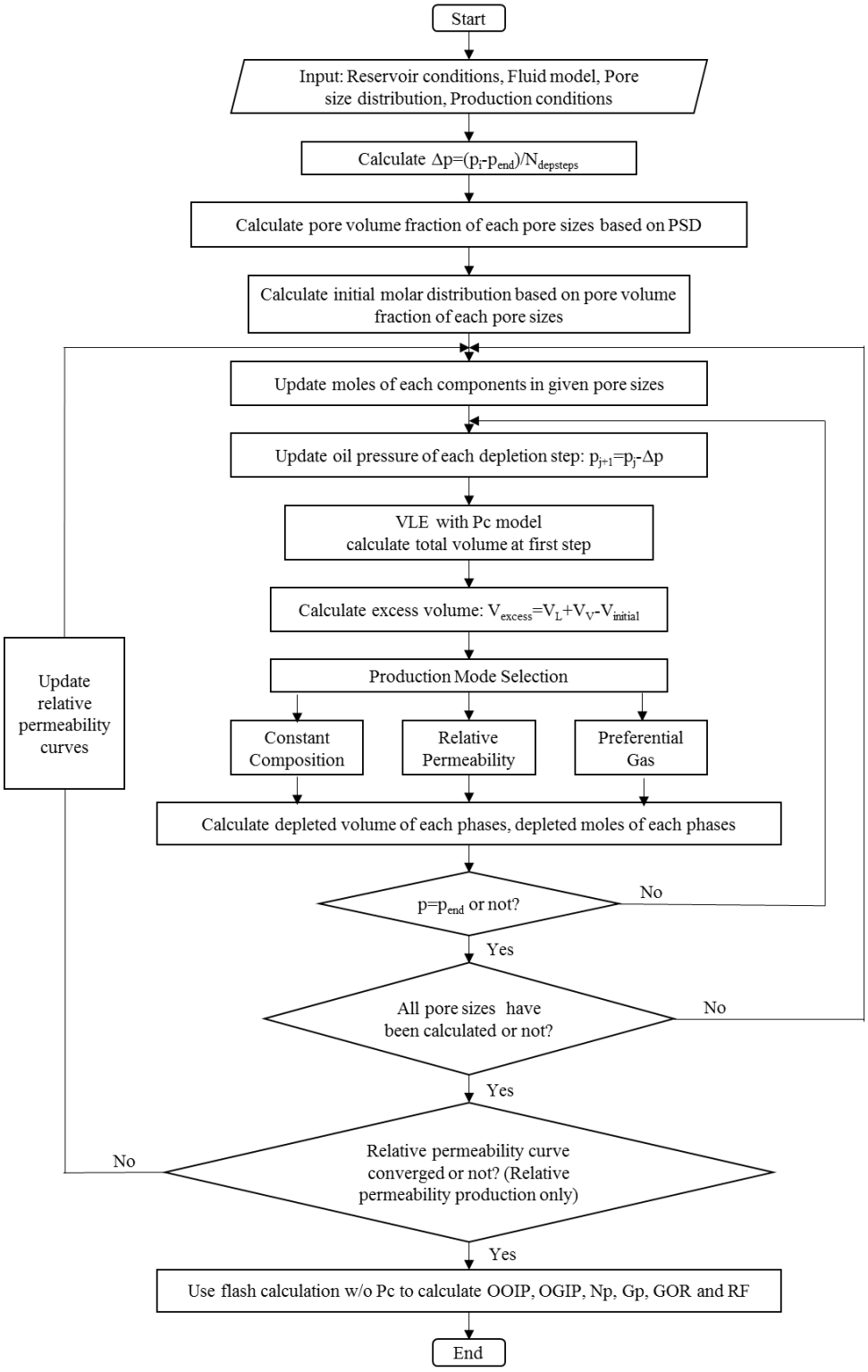

Fig. 2 General flow chart of the mechanistic model proposed for depletion

3.2. Mechanistic Model for Injection

The mechanistic model for injection is to simulate a huff-n-puff injection followed by a constant volume depletion process incorporating pore size distribution, coupled PR-EOS with capillary pressure, different injection fluid distribution modes to be discussed in this chapter and the different production modes discussed before. Given a certain ratio of injection fluid to fluid (oil) in the pore, the volume of the pores would expand at the specified constant pressure. Since the total volume of the pores is assumed to be a constant, the excess volume is being depleted. The exact composition of the produced excess volume fluid depends on the production mode selection. The mechanistic model in this study treats the reservoir as a combination of independent tubes with same height (h) but different pore sizes as shown in **Fig. 3**.

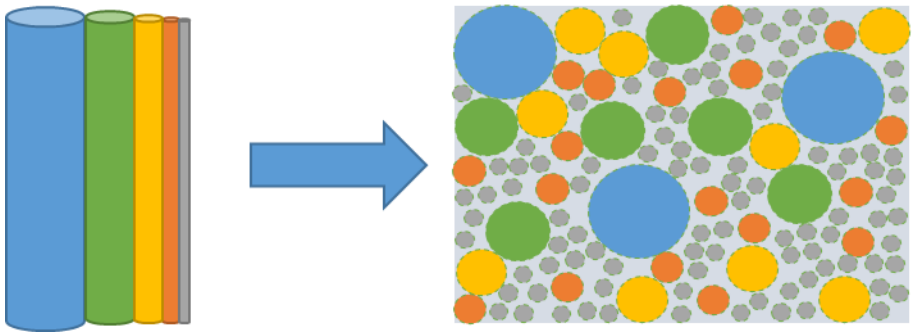

Fig. 3 Diagram of pore network in the mechanistic model

The amount of fluid injected into each pore depends on the injection fluid distribution modes selection. Two different injection fluid distribution modes are built in the model, these are pore volume distribution and pore opening distribution. Since the tubes in the model are with same height (h), the pore volume ratio is as same as the pore

area ratio. The pore volume mode assumes the moles of injected fluid into each pore sizes are proportional to the volume fraction of that size of pores as shown in equation 3.7.

$$n_{inj,j} = n_{inj,total}\frac{V_j}{V_{total}} = n_{inj,total}\frac{N_j \pi h D_j^2}{\sum_{j=1}^{N_p} N_j \, \pi h D_j^2} \tag{3.7}$$

Where, $n_{inj,j}$ represent the moles of injection fluid into the pore type j with diameter D_j, $n_{inj,total}$ is the total moles of injection fluid into the system, N_j is the number of pore type j, N_p is the number of pore sizes. While the pore opening mode assumes the moles of injection fluid into each pore sizes depend on the ratio of summation of pore diameters of that size of pores to the summation of all pore diameters in the system. The equations used to determine injection fluid distribution by pore opening mode are shown below:

$$n_{inj,j} = n_{inj,total}\frac{D_j f_{n,j}}{D_{avg}} \tag{3.8}$$

$$f_{n,j} = \frac{N_j}{\sum_{j=1}^{N_p} N_j} = \frac{\frac{f_{Vj} V_{total}}{\pi D_j^2 h}}{\sum_{j=1}^{N_p} \frac{f_{Vj} V_{total}}{\pi D_j^2 h}} = \frac{\frac{f_{Vj}}{D_j^2}}{\sum_{j=1}^{N_p} \frac{f_{Vj}}{D_j^2}} \tag{3.9}$$

$$D_{avg} = \sum_{j=1}^{N_p} D_j f_{n,j} \tag{3.10}$$

Where, D_{avg} is the average pore diameter of the whole system with the unique height (h), $f_{n,j}$ represents the ratio between the number of pores type j over the total number of pores, and f_{Vj} represents the ratio between the volume occupied by pores j over the total pore volumes.

For example, if 30% of the pore volume is made of pores with a diameter of 10nm for a 1 cm^3 sample with 1cm height.

$$N_{10nm} = \frac{0.3 \times 1}{\pi(10^{-7})^2 \times 1} = 9.55 \times 10^{12}$$

If 30% of the pore volume is made of pores with a diameter of 100nm for a 1 cm^3 sample with 1cm height.

$$N_{100nm} = \frac{0.3 \times 1}{\pi(10^{-6})^2 \times 1} = 9.55 \times 10^{10}$$

The general flow chart of the mechanistic model for injection process is shown in **Fig. 4**.

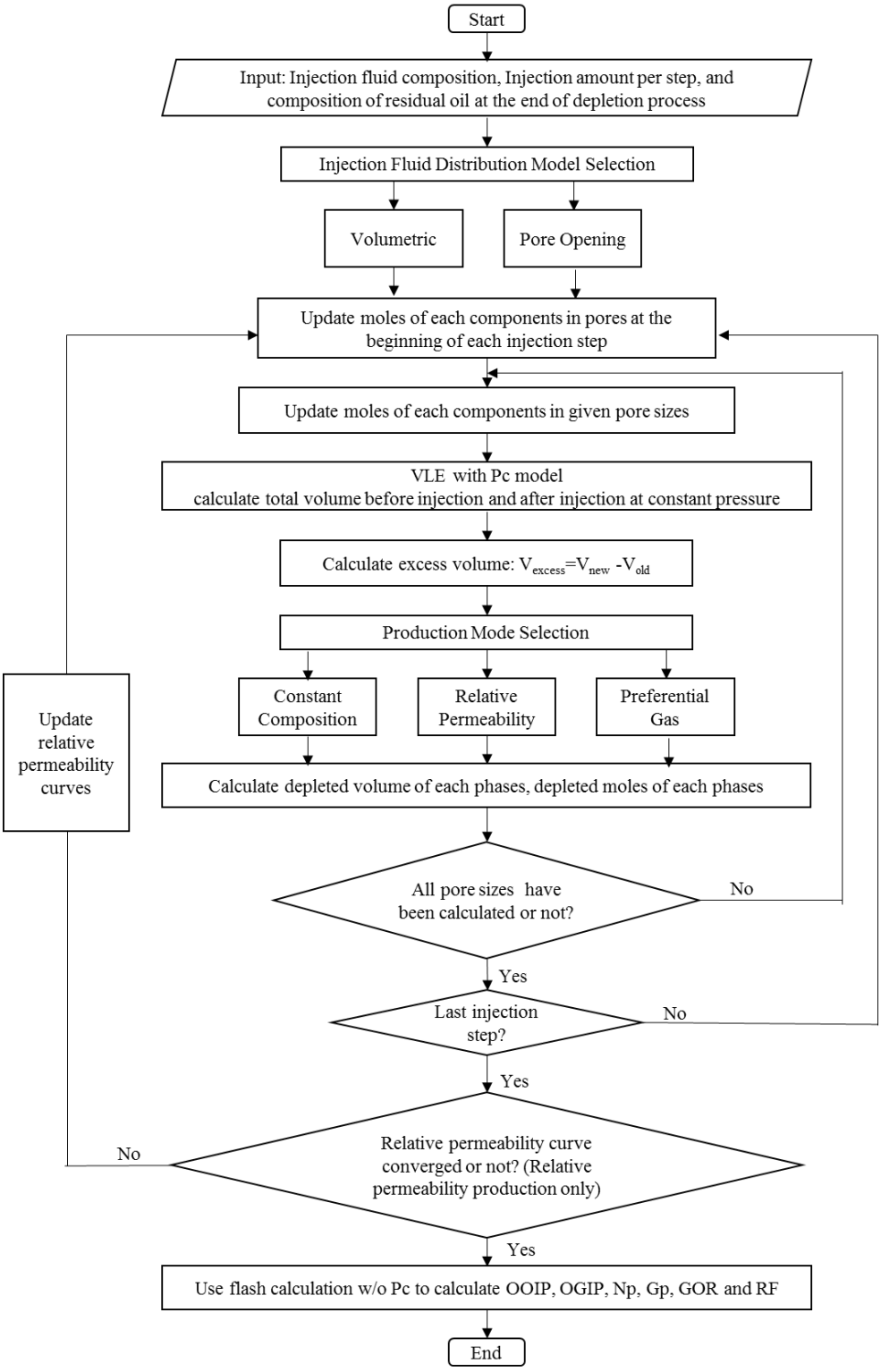

Fig. 4 General flow chart of the mechanistic model for injection

CHAPTER IV

DEVELOPMENT OF FLUID MODEL AND PORE SIZE DISTRIBUTION MODELS

The reservoir fluid sample used for this work was a volatile oil from an anonymous oilfield in North America, with more than 40 components, such as N_2, CO_2, C_1 to C_{36}^+. The reported PVT data for this fluid includes compositional analysis of initial oil and residual oil, a constant composition expansion (CCE), differential liberation (DL) and separator tests.

4.1. Quality Control (QC) Test

The quality control of the experimental data is important and been studied for a while. Most existing QC methods are material balance methods for evaluating constant volume depletion (CVD) experimental data (Bashbush 1981, Whitson and Torp 1983, Drohm et al. 1988, Whitson and Brule, 2000, Imo-Jack, 2010). In this study, to examine the laboratory data and determine the main contributors to the uncertainty, a new protocol for QC test of differential liberation experiments was developed based on material balance.

For the differential liberation (DL) process, the solution gas liberated from an oil sample during a pressure decline is continuously removed from contact with the oil, and after establishing equilibrium with the liquid phase. Thus, the DL experiments provide the composition of gas liberated in each stag and liberated cumulative GOR. With these data

and the properties of the initial fluid, we can calculate the composition of the oil in each stage; or with these data and the residual oil, we can recombine the liberated gas and oil of each stage to obtain the composition of oil in the previous stage. Therefore, this QC test protocol has two different schemes which are forward scheme and backward scheme as shown in **Fig. 5**. The input data for the quality test are temperature, properties of the residual oil such as molecular weight, volume and density, composition of initial fluid and residual oil, the characterizations of components and DL experiments data.

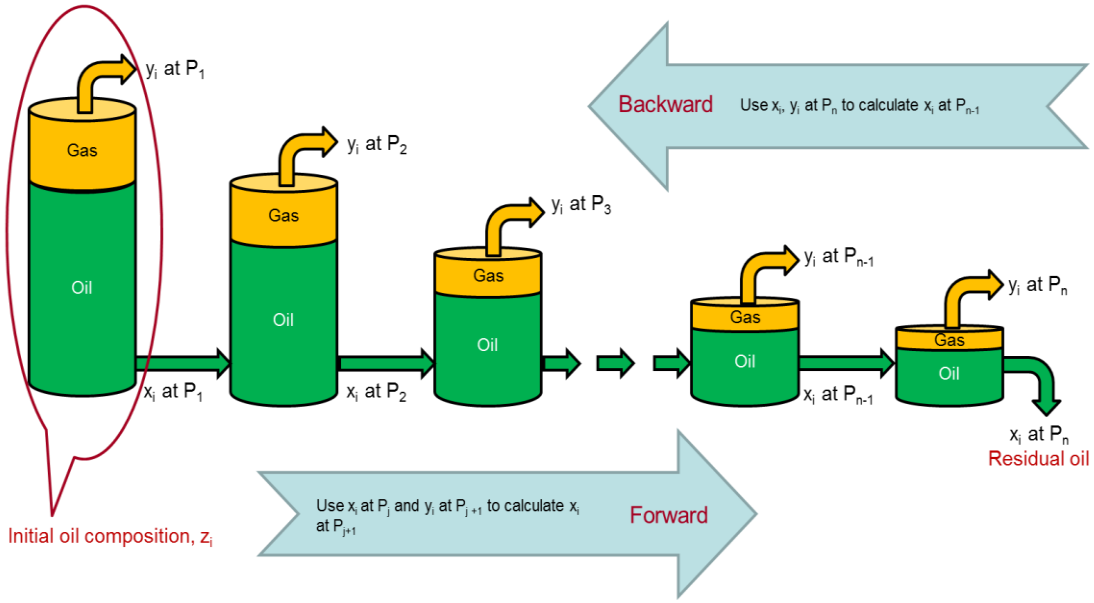

Fig. 5 Diagram of quality control (QC) test for differential liberation (DL) process

4.1.1 Forward Scheme

The forward method for QC test of DL experiments is explained from equation 4.1 to 4.5.

$$n_{initial}^{1} = moles\ of\ gas\ liberated + moles\ in\ residual\ oil$$

$$= \frac{GOR^{ns} V_{res.oil} p_{sc}}{RT_{sc}} + \frac{V_{res.oil} \rho_{res.oil}}{5.615 MW_{res.oil}} \tag{4.1}$$

$$n_g^k = V_{res.oil}(GOR^k - GOR^{k-1}) \frac{p_{sc}}{RT_{sc}} \tag{4.2}$$

$$n_o^k = n_{initial}^k - n_g^k \tag{4.3}$$

$$f_{ng}^k = \frac{n_g^k}{n_{initial}^k} \tag{4.4}$$

$$n_{initial}^{k+1} = n_o^k \tag{4.5}$$

Where, $n_{initial}^1$ represents the mole number of the initial fluid at 1st stage, GOR^{ns} represents the cumulative gas-oil ratio at the final stage (number of the stage), which is the ratio of volume of liberated gas to the volume of residual oil, $V_{res.oil}$ represents the volume of residual oil, $\rho_{res.oil}$ represents the density of the residual oil, $MW_{res.oil}$ represents the molecular weight of the residual oil, note that both $\rho_{res.oil}$ and $MW_{res.oil}$ are given from the PVT report which are the uncertainties here, p_{sc} and T_{sc} represent the pressure and temperature at the standard condition, which are 14.7 psia and 520 °R, respectively. n_g^k, n_o^k and $n_{initial}^k$ represent the mole number of gas, oil and mixture at the k-th stage respectively. And f_{ng}^k represents the mole fraction of the gas at the k-th stage.

Then to calculate the composition of remaining oil with the given liberated gas composition for each stage forward from the initial stage to the final stage by the following equations.

$$x_j^k = \frac{z_j^k - y_j^k f_{ng}^k}{1 - f_{ng}^k} \tag{4.6}$$

$$z_j^{k+1} = x_j^k \tag{4.7}$$

Where, x_j^k, y_j^k and z_j^k represent the mole fraction of j-th component in the oil, gas and mixture, respectively.

Finally, to compare the calculated residual oil composition with that from the experiment by the equation below, the subscription cal and obs represent calculation and observation, respectively.

$$error_j = \frac{x_{j,cal} - x_{j,obs}}{x_{j,obs}} \times 100\% \tag{4.8}$$

Table 1 shows the given and computed properties of each stage in forward scheme. And the flow chart of the forward scheme is shown in **Fig. 6**.

Table 1 Given and computed properties of each stage in forward scheme

#Stage	Given properties	Computed properties
1	$p_1, n_o^0, GOR^1, GOR^{ns}, V_{res.oil}, y_j^1, z_j^1$	$n_g^1, n_o^1, f_{ng}^1, x_j^1$
2	$p_2, n_o^1, GOR^1, GOR^2, V_{res.oil}, y_j^2, x_j^1$	$n_g^2, n_o^2, f_{ng}^2, x_j^2$
…	…	…
k	$p_k, n_o^{k-1}, GOR^{k-1}, GOR^k, V_{res.oil}, y_j^k, x_j^{k-1}$	$n_g^k, n_o^k, f_{ng}^k, x_j^2$
…	…	…
ns	$p_{ns}, n_o^{ns-1}, GOR^{ns-1}, GOR^{ns}, V_{res.oil}, y_j^{ns}, x_j^{ns-1}$	$n_g^{ns}, n_o^{ns}, f_{ng}^{ns}, x_j^{ns}$

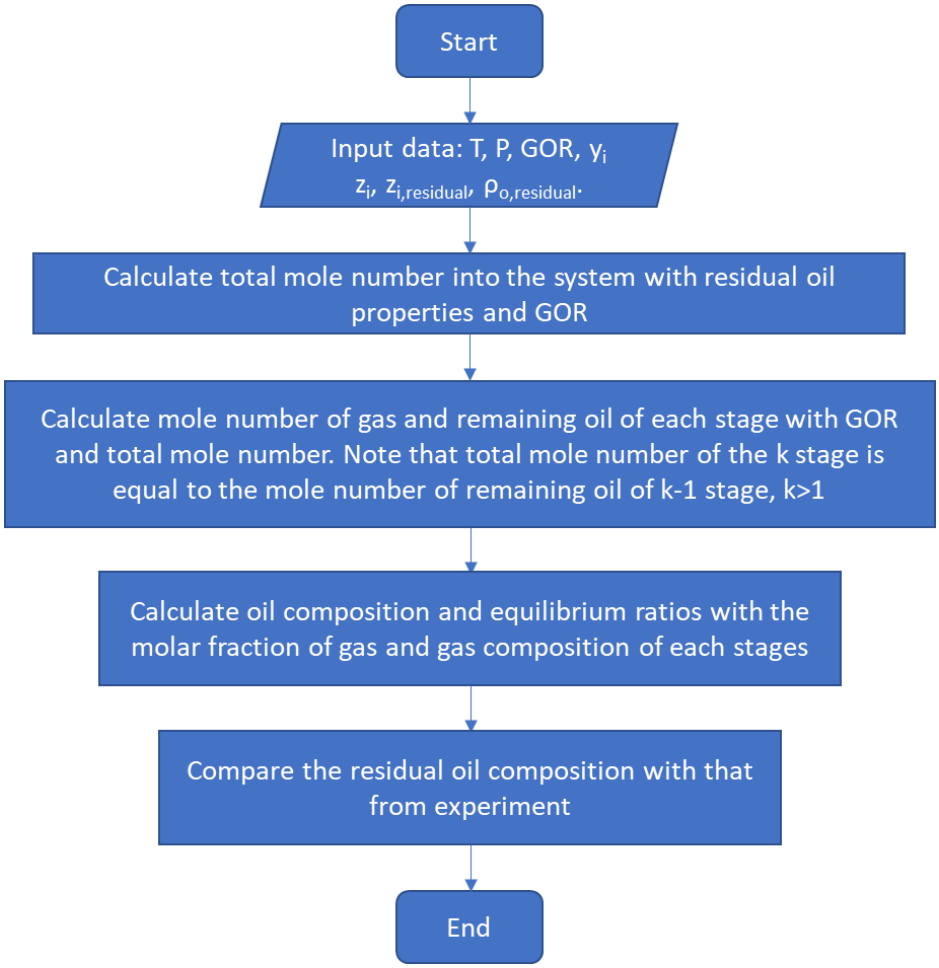

Fig. 6 Flow chart of forward scheme for QC test for DL experiments.

4.1.2 Backward Scheme

The backward method for QC test of DL experiments consists in evaluating the moles of remaining oil at each stage with GOR and given residual oil volume, and then calculating the composition of remaining oil with the given liberated gas composition for each stage back from the final stage to the initial stage. The equations used are below:

$$n_g^k = V_{res.oil}(GOR^k - GOR^{k-1})\frac{p_{sc}}{RT_{sc}} \tag{4.2}$$

$$n_o^{ns} = \frac{V_{res.oil}\rho_{res.oil}}{5.615MW_{res.oil}} \tag{4.9}$$

$$n_o^k = n_o^{k+1} + n_g^{k+1} \tag{4.10}$$

$$f_{ng}^k = \frac{n_g^k}{n_o^k + n_g^k} \tag{4.11}$$

$$x_j^k = x_j^{k+1}\left(1 - f_{ng}^{k+1}\right) + y_j^{k+1} f_{ng}^{k+1} \tag{4.12}$$

Finally, to compare the calculated initial oil composition with that given by the experiment. **Table 2** shows the given and computed properties of each stage in backward scheme. And the flow chart of the backward scheme is shown in **Fig. 7**.

Table 2 Given and computed properties of each stage in backward scheme

#Stage	Given properties	Computed properties
ns	$p_{ns}, n_o^{ns}, GOR^{ns}, GOR^{ns-1}, V_{res.oil}, y_j^{ns}, z_j^{ns}$	$n_g^{ns}, n_o^{ns-1}, f_{ng}^{ns}, x_j^{ns}$
ns-1	$p_{ns-1}, n_o^{ns-1}, GOR^{ns-1}, GOR^{ns-2}, V_{res.oil}$, y_j^{ns-1}, x_j^{ns}	$n_g^{ns-1}, n_o^{ns-2}, f_{ng}^{ns-1}, x_j^{ns-1}$
…	…	…
k	$p_k, n_o^k, GOR^{k-1}, GOR^k, V_{res.oil}, y_j^k, x_j^{k+1}$	$n_g^k, n_o^{k-1}, f_{ng}^k, x_j^k$
…	…	…
1	$p_1, n_o^1, GOR^1, V_{res.oil}, y_j^1, x_j^2$	$n_g^1, n_{initial}^1, f_{ng}^1, x_j^1$

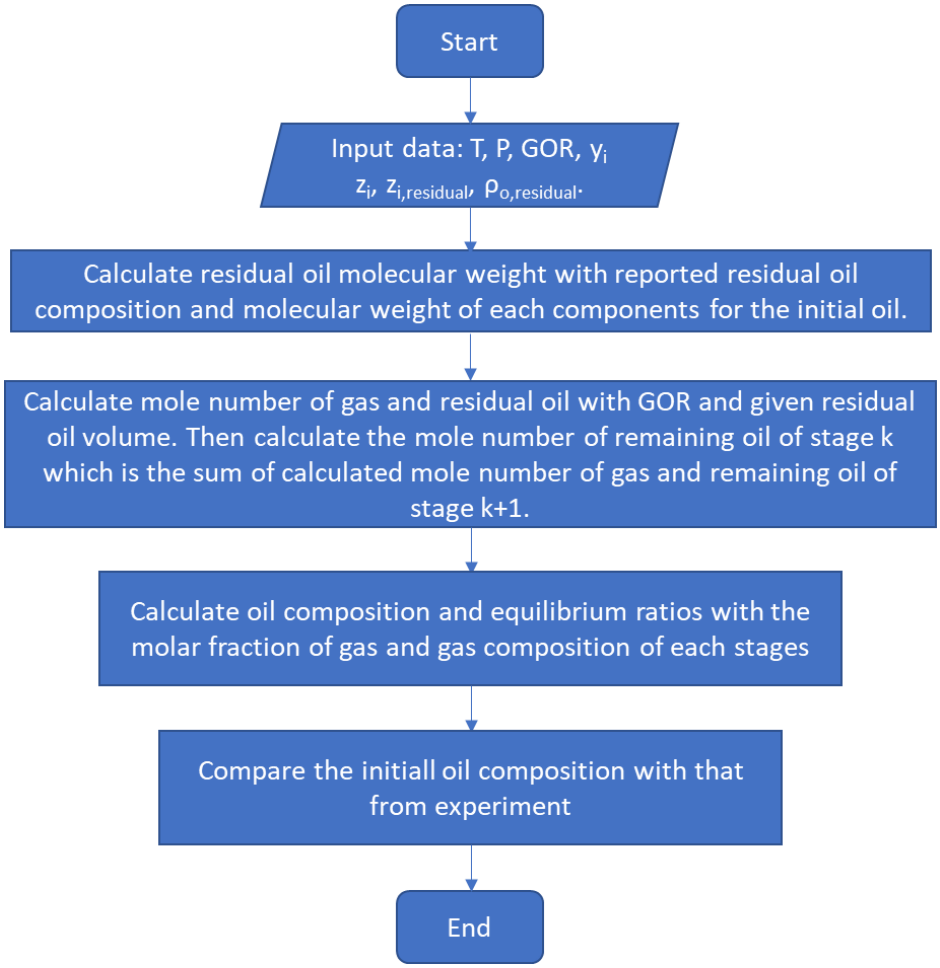

Fig. 7 Flow chart of backward scheme for QC test for DL experiments.

By using the developed QC test protocol in this study, the comparison between the experimental data and the calculated data using forward or backward scheme are shown in **Table 3** and **Table 4**, respectively. Significant discrepancies are observed when comparing the residual oil composition as shown in **Table 3**, which illustrate uncertainties in the reported residual oil molecular weight mostly due to the plus fraction molecular weight. While reasonable errors of most components except N_2 and the plus fraction are observed in the comparison of initial fluid composition as shown in **Table 4**, which

illustrate uncertainties in the reported plus fraction molecular weight and measurement of N_2. Since N_2 usually comes from the sampling technique, N_2 can be combined with CH_4 as a pseudo-component to eliminate the uncertainty from the measurement of N_2.

Table 3 Comparison of residual oil composition between experimental data and calculated data using forward scheme

Components	*Observed*	*Calculated*	*Error%*
N_2	0.0000	0.0000	0.00
CO_2	0.0000	0.0000	0.00
X_1	0.0000	0.0000	0.00
X_2	0.0044	0.0000	-100.00
X_3	0.0208	0.0243	17.06
X_4	0.0096	0.0105	9.88
X_5	0.0398	0.0425	6.68
X_6	0.0247	0.0248	0.36
X_7	0.0423	0.0410	-3.16
X_8	0.0688	0.0628	-8.77
C_{X^+}	0.7895	0.7941	0.59

Table 4 Comparison of initial fluid composition between experimental data and calculated data using backward scheme

Components	*Observed*	*Calculated*	*Error%*
N_2	0.0090	0.0097	6.99
CO_2	0.0019	0.0020	5.47
X_1	0.4941	0.5179	4.82
X_2	0.0821	0.0832	1.35
X_3	0.0571	0.0546	-4.49
X_4	0.0112	0.0105	-5.91
X_5	0.0346	0.0325	-6.16
X_6	0.0137	0.0130	-5.21
X_7	0.0204	0.0197	-3.31
X_8	0.0247	0.0250	0.94
C_{X^+}	0.2510	0.2319	-7.62

4.1.3 Hoffman Consistence checks

Hoffman et al.(1953) found that for a reservoir gas condensate, the trend of log ($K_i p$) vs. F_i is linear for components C_1 through C_3 at all pressures, while the function turns downward for heavier components at low pressure. Thus, using Hoffman plots was suggested to check the experimental error for quality control test. A typical Hoffman plots are log ($K_i p$) vs. F_i for each component. The definition of the F_i is shown below:

$$F_i = b_i \left(\frac{1}{T_{bi}} - \frac{1}{T} \right) \tag{4.13}$$

$$b_i = \frac{\log\left(\frac{p_{ci}}{14.7}\right)}{\left(\frac{1}{T_{bi}} - \frac{1}{T_{ci}}\right)} \tag{4.14}$$

Where, T_{bi} represents the boiling temperature at atmospheric pressure of the i-th component, which can be obtained from reference table or correlations, T represents the experiment temperature, T_{ci} represents the critical temperature of the i-th component, and p_{ci} represents the critical pressure of the i-th component. The calculated F values of the components in the given fluid are shown in **Table 5**.

Table 5 Calculated *F* values of each components

Components	F
N_2	7.06
CO_2	5.23
X_1	6.25
X_2	4.59
X_3	3.33
X_4	2.46
X_5	2.17
X_6	1.35
X_7	1.12
X_8	0.16
C_X^+	-7.86

The Hoffman plots of the given fluid calculated with forward scheme and backward scheme are shown in **Fig. 8** and **Fig. 9**, respectively.

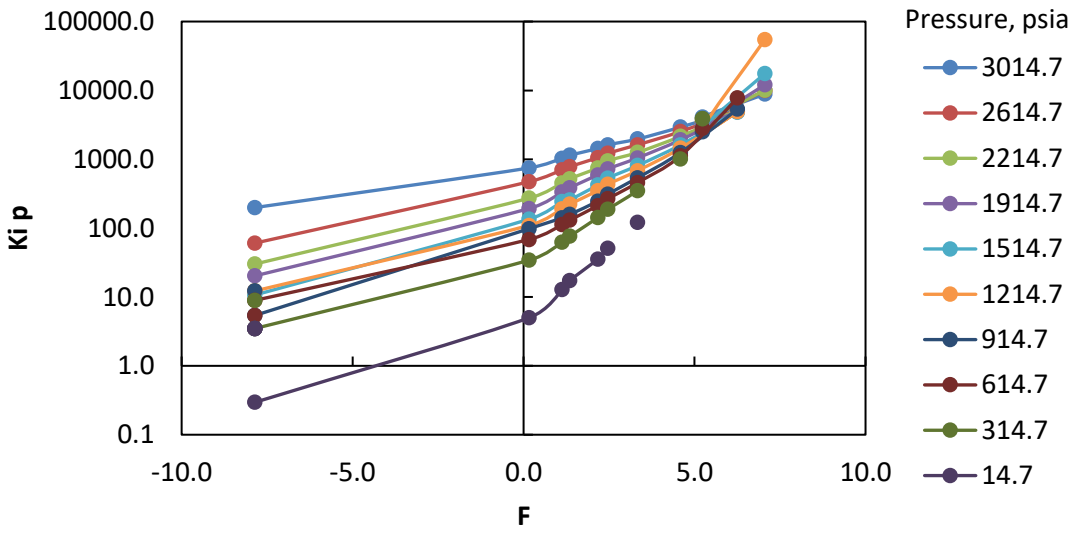

Fig. 8 Hoffman plot of calculated data using forward scheme

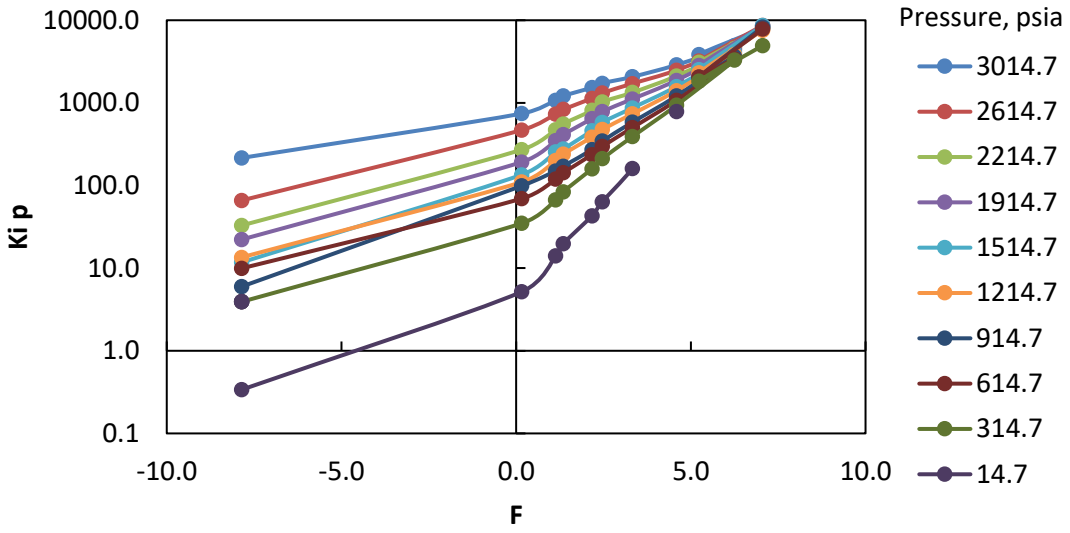

Fig. 9 Hoffman plot of calculated data using backward scheme

Nearly straight-lines in the Hoffman plots indicate that the liquid and vapor samples are reasonably in equilibrium at the separator conditions, and the measurement of the liquid and vapor compositions generally error free for components X1-X8. Some crossovers are observed in the Hoffman plots of the data both using forward scheme and backward scheme at large values of *F*, which represents the components N_2 and CO_2. Since the nonhydrocarbon components, such as N_2 and CO_2 may not follow the similar trend as hydrocarbon components, which are usually excluded from the Hoffman plots. And the points at negative *F* value represent the component C_x^+. It can be observed that C_X^+ is the pseudo-component that damages the straight-line trend. Usually, the plus fraction is not included in Hoffman consideration because the properties of it are generally not measured accurately. The *F* value of the plus fraction will be a negative or a positive

as the boiling temperature of the plus fraction higher or lower than the experiment temperature.

With these findings from the QC test, we can re-run the QC test for a modified fluid sample, where the N_2 is combined with X_1 as a pseudo-component (N2X1), X2 to X3 are combined as X2-3, X4 to X8 are combined as X4-8 and the Hoffman plots are shown excluding CO_2 and C_x^+. The results with forward scheme are shown in **Table 6** and **Fig. 10**, and those with backward scheme are in **Table 7** and **Fig, 11**. As shown, the results of the modified fluid sample are better.

Table 6 Comparison of residual oil composition between experimental data and calculated data using forward scheme for modified fluid sample

Components	*Observed*	*Calculated*	*Error%*
N_2X_1	0.0000	0.0000	0.00
CO_2	0.0000	0.0000	0.00
X_{2-3}	0.0252	0.0194	-23.21
X_{4-8}	0.1853	0.1824	-1.58
C_X^+	0.7895	0.7983	1.11

Table 7 Comparison of initial fluid composition between experimental data and calculated data using backward scheme for modified fluid sample

Components	*Observed*	*Calculated*	*Error%*
N_2X_1	0.5032	0.5268	4.69
CO_2	0.0019	0.0020	5.30
X_{2-3}	0.1392	0.1376	-1.17
X_{4-8}	0.1047	0.1008	-3.65
C_X^+	0.2510	0.2328	-7.27

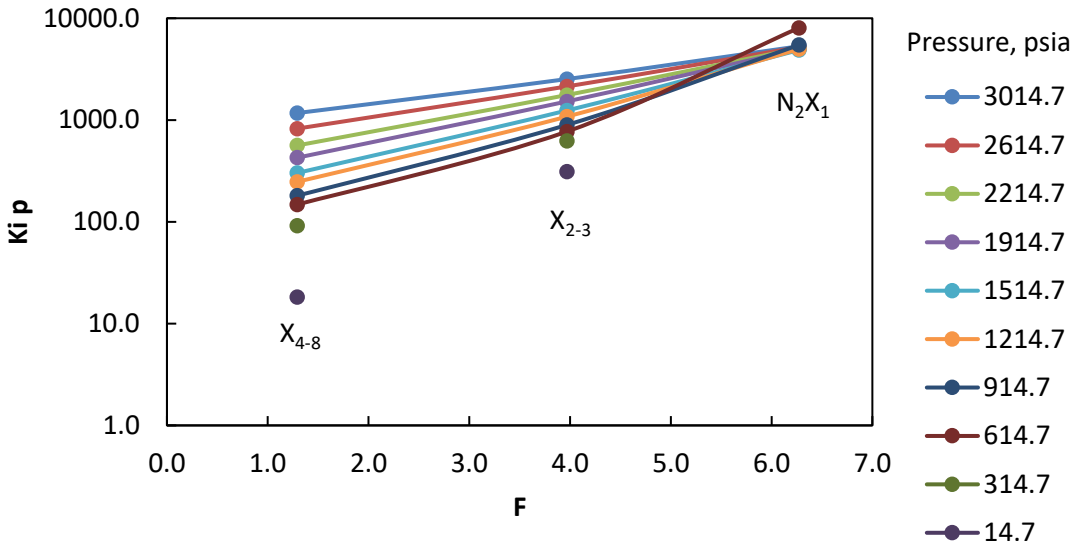

Fig. 10 Hoffman plot of calculated data using forward scheme for modified fluid sample

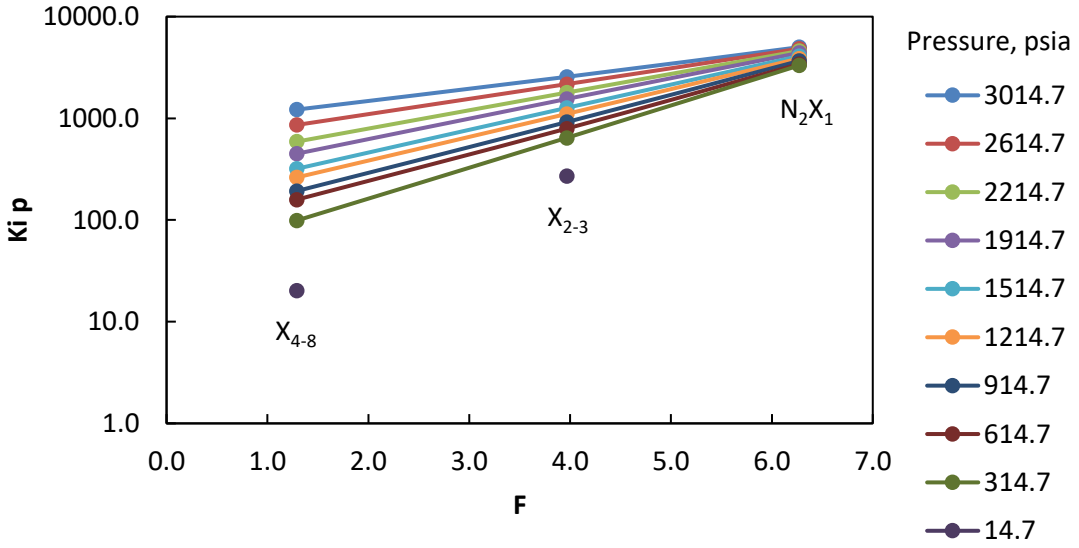

Fig. 11 Hoffman plot of calculated data using backward scheme for modified fluid sample

4.2. Hydrocarbons Calibration

Based on the quality control results, molecular weight and specific gravity of the plus fraction provided by the laboratory experiments may have a significant error. A

proper description of the physical properties of the plus fractions is essential for reliable phase behavior calculations and compositional modeling studies. To better describe the plus fraction, the first step in this study is splitting the plus fraction. There are several existing methods proposed for splitting the plus fraction. Three important requirements must be satisfied for any splitting method. These requirements are as follows: (assuming that the plus fraction is C_7^+)

$$\sum_{i=7}^{n_c} z_i = z_{C_7^+} \tag{4.15}$$

$$\sum_{i=7}^{n_c} z_i Mw_i = z_{C_7^+} Mw_{C_7^+} \tag{4.16}$$

$$\sum_{i=7}^{n_c} \frac{z_i Mw_i}{\gamma_i} = \frac{z_{C_7^+} Mw_{C_7^+}}{\gamma_{C_7^+}} \tag{4.17}$$

In this study, Behrens and Sandler (1988) splitting scheme was used to calibrate the fluid model.

The step-by-step procedure for the Behrens and Sandler splitting scheme is shown below:

Step 1: Assume the starting and ending carbon numbers, CN_s and CN_e, respectively. Since the endpoints of the distribution are assumed to start and end at the midpoint between the two carbon numbers, the effective endpoints become:

$$A = CN_s - 0.5 \tag{4.18}$$

$$B = CN_e + 0.5 \tag{4.19}$$

Step 2: Calculate the average carbon number $\overline{CN}$ and solve the equation for α and determine the slope of distribution.

$$\overline{CN} = \frac{Mw_{C_7^+} + 4}{14} \tag{4.20}$$

$$\frac{1}{\alpha} = \overline{CN} - A + \left[\frac{(B-A)\exp(-B\alpha)}{\exp(-A\alpha) - \exp(-B\alpha)}\right] \tag{4.21}$$

Step 3: Evaluate the range of integration c and find the weights from the roots and weights table for two-point integration.

$$c = (B - A)\alpha \tag{4.22}$$

Step 4: Find pseudo-component carbon numbers and mole fractions.

$$CN_i = \frac{r_i}{\alpha} + A \tag{4.23}$$

$$z_{CN_i} = w_i z_{C_7^+} \tag{4.24}$$

In this study, the plus fraction is split into two pseudo-components named F1 and F2. The properties of these two pseudo-components are obtained by interpolation from hydrocarbon properties table for aromaticity is zero, based on the carbon numbers calculated with splitting scheme.

To reduce CPU time in compositional reservoir simulations, a minimum number of components should be used in the equation of state (EOS) to describe the fluid phase and volumetric behavior. Usually, the fluid model contains only 6-9 lumped components based on the purpose of the simulation. The molecular weight and specific gravity of the lumped compound are determined by reverse application of the constraints defined in the splitting procedures. Thus, three requirements must be satisfied for any lumping method

as well. These requirements are as follows: (assuming lumping the components from C_4 to C_6)

$$\sum_{i=4}^{6} z_i = z_{C_4-C_6} \tag{4.25}$$

$$\sum_{i=4}^{6} z_i Mw_i = z_{C_4-C_6} Mw_{C_4-C_6} \tag{4.26}$$

$$\sum_{i=4}^{6} \frac{z_i Mw_i}{\gamma_i} = \frac{z_{C_4-C_6} Mw_{C_4-C_6}}{\gamma_{C_4-C_6}} \tag{4.27}$$

The selection of which components to lump together is not unique because of many possible combinations. The success of lumping strategies relies on the accuracy of the reduced model relative to the detailed EOS model in capturing the phase behavior of the mixtures that developed during a displacement process. In this study, to model CO_2 injection, CO_2 is treated as a single component. Other components, such as N_2 and C_1-C_6, are grouped into three lumped-components named N2C1, C2-3 and C4-6, respectively. The original properties of each components in this 6-component fluid model are shown in **Table 8** and **Table 9**.

Table 8 Original properties of components in 6-component fluid model

Components	Mol%	Mw	Tc, °F	Pc, psia	ω	Vc, ft^3/mol	Volume shifts	Parachor, $(dyn/cm)^{1/4}$ ×(cm^3/mol)
CO_2	0.198	44.01	87.89	1069.87	0.22	1.51	-0.04	78.00
N2C1	49.41	16.26	-120.18	661.78	0.01	1.58	-0.15	76.18
C2-3	13.83	35.83	148.59	661.59	0.13	2.82	-0.09	130.62
C4-6	10.87	69.32	371.24	492.99	0.24	4.91	-0.04	227.18
F1	20.75	152.5	718.06	312.63	0.47	12.43	0.05	556.16
F2	4.942	469.0	1173.84	146.24	1.15	36.81	0.03	1649.8

Table 9 Original binary interaction coefficients of 6-component fluid model

Components	CO_2	N2C1	C2-3	C4-6	F1	F2
CO_2	-	0	0	0	0	0
N2C1	0	-	0	0	0	0
C2-3	0	0	-	0	0	0
C4-6	0	0	0	-	0	0
F1	0	0	0	0	-	0
F2	0	0	0	0	0	-

Currently, the industry approach to improve the prediction capabilities of an EOS model is to tune it with experimental data obtained at specific pressures and temperatures in the PVT laboratory. Although the industry has no consensus on single standard method of tuning, the various approaches carry some similarities (Coats and Smart 1986, Christensen 1999, Whitson and Brule 2000, Al-Meshari 2004). In this study, tuning is conducted using PVTsim Nova3 (2019) to minimize the difference between the predicted values by calculation and measured values by experiments. The adjusting parameters according to most of the literatures include properties of pseudo-components split from the plus fraction, binary interaction coefficients between pseudo-components and components with larger molar fractions, and Lohrenz-Bray-Clark viscosity coefficients. The tuned properties of components in 6-component fluid model are shown in **Table 10** and **Table 11**, the values in red are the properties which have been tuned, which are properties of F1 and F2, binary interaction coefficients between F1 and N2C1, between F2 and N2C1, and between F2 and CO_2, and Lohrenz-Bray-Clark viscosity coefficients.

Table 10 Tuned properties of components in 6-component fluid model

Comp-onents	Mol %	Mw	Tc, °F	Pc, psia	ω	Vc, ft^3/mol	Volume shifts	Parachor, $(dyn/cm)^{1/4} \times (cm^3/mol)$
CO_2	0.198	44.01	87.89	1069.87	0.22	1.51	-0.04	78.00
N2C1	49.41	16.26	-120.18	661.78	0.01	1.58	-0.15	76.18
C2-3	13.83	35.83	148.59	661.59	0.13	2.82	-0.09	130.62
C4-6	10.87	69.32	371.24	492.99	0.24	4.91	-0.04	227.18
F1	20.75	142.5 (-6.5%)	680.89 (-5.2%)	367.14 (17.4%)	0.47 (0.1%)	10.32 (-17.0%)	0.01 (-80.0%)	533.08 (-4.1%)
F2	4.942	410.5 (-12.6%)	1064.2 (-9.3%)	150.05 (2.6%)	1.27 (10%)	24.37 (-33.8%)	0.18 (500%)	1479.3 (-10.3%)

Table 11 Tuned binary interaction coefficient of 6-component fluid model

Components	CO_2	N2C1	C2-3	C4-6	F1	F2
CO_2	-	0	0	0	0	0.001
N2C1	0	-	0	0	0.05	0.05
C2-3	0	0	-	0	0	0
C4-6	0	0	0	-	0	0
F1	0	0.05	0	0	-	0
F2	0.001	0.05	0	0	0	-

Lohrenz-Bray-Clark viscosity coefficients (LBC_1 *to* LBC_5) after tuning are 0.101878, 0.019268, 0.065420, -0.039850 and 0.008169. Under reservoir temperature (165 °F), the simulated bubble point pressure for the original 6-component fluid model is 2731 psia, and that for the tuned 6-component fluid model is 3511 psia, compared to experimental result which is 3406 psia. Other properties, such as relative volume, solution gas-oil ratio, density of the oil and gas, and viscosity of the oil and gas, can be well reproduced using this tuned 6-component fluid model, comparing to those from constant composition expansion (CCE) and differential liberation (DL) experiments and those calculated using original 6-component fluid model. The comparisons are shown in **Fig.**

12. The predicted data with the tuned 6-component fluid model show a better match with the experimental data than that with the original 6-component fluid model.

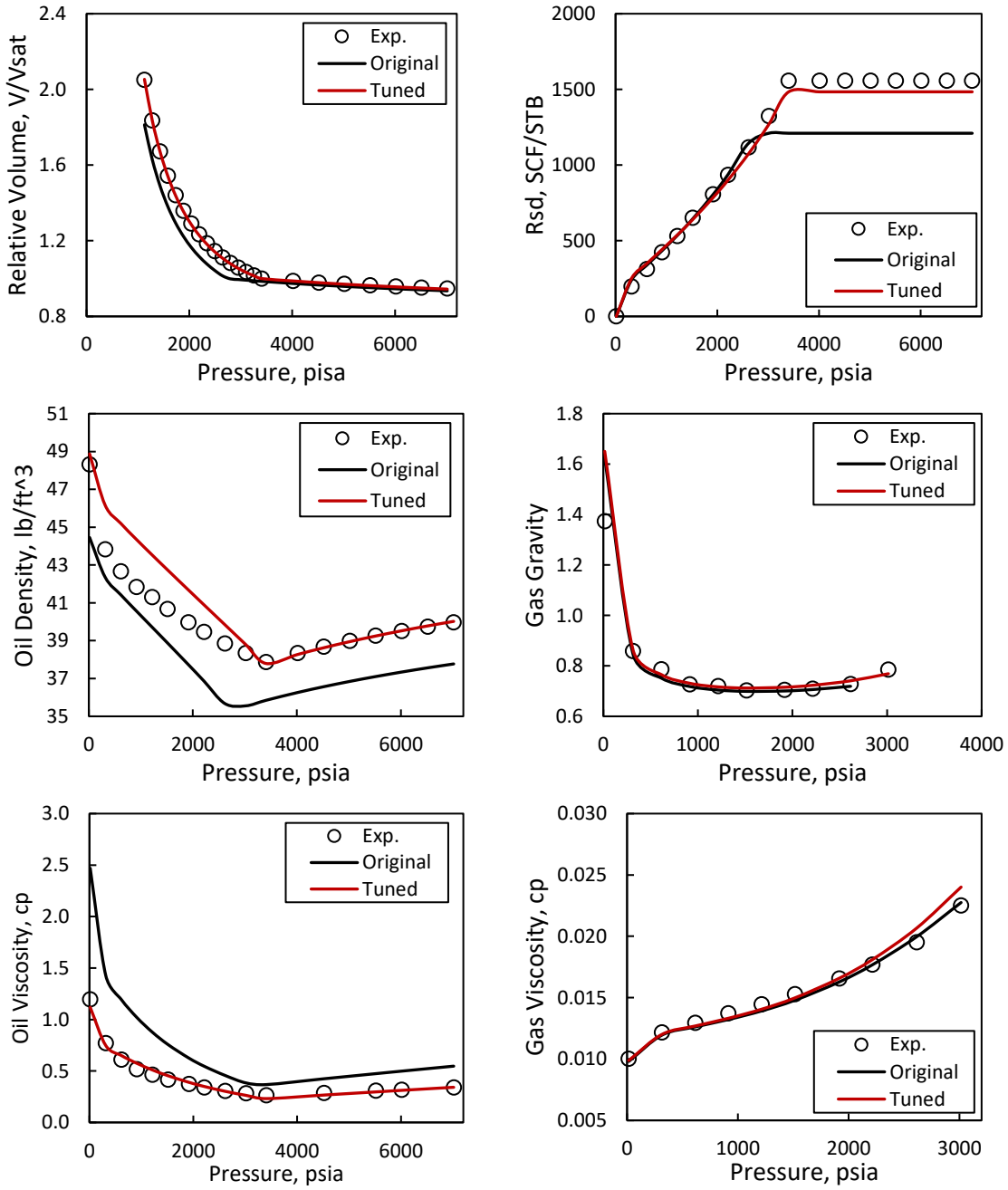

Fig. 12 Comparison of PVT results from experiment and simulation for both original and tuned 6-component fluid model

4.3. Pore Size Distribution Models

With given experimental pore size distribution data, a data regression process was conducted using either a probability density lognormal function or a cumulative lognormal distribution function. The mean and standard deviations were obtained by minimizing the sum of the squared residual (R^2). In this study, the cumulative pore volume fraction distribution data are coming from Brunauer-Emmett-Teller (BET) analysis of an anonymous oilfield in North America. After cumulative pore size distribution been fitted, the incremental pore volume fraction distribution can be calculated using the fitted model to compare with the experimental data. **Fig. 13** shows the fitting results for the pore size distributions of one sample of this oilfield. The mean and standard deviation are shown in the **Fig.13** caption.

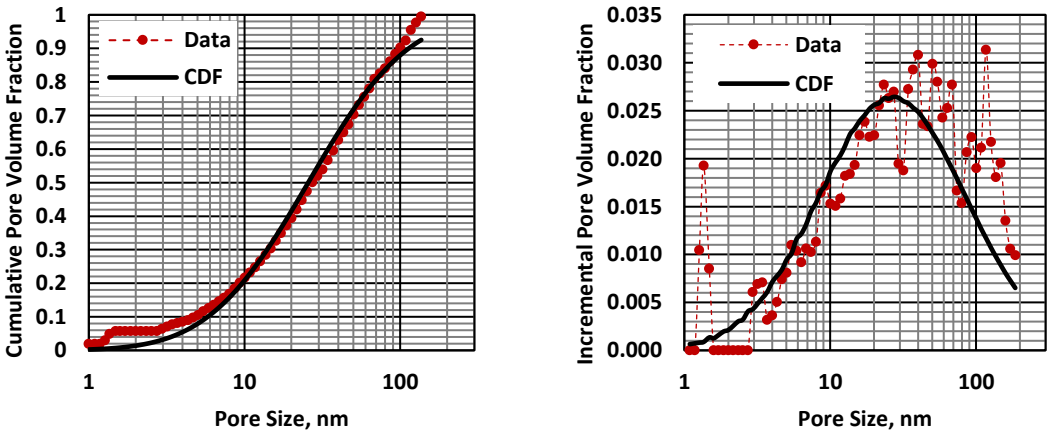

Fig. 13 Pore size distribution of sample (μ=3.245, σ=1.160)

As shown, CDF describes pore size distribution of this sample. To represent the cumulative pore size distribution in the Figs above using a finite number of pores, pore sizes must be assigned such that they match the specified cumulative distribution. Czernia

(2018) proposed to divide the cumulative pore size distribution by a number of pore size bins specified to produce equally spaced segments. And the midpoint probability value for each segment is selected to determine the corresponding pore size for that bin. An example with μ=2.708 and σ=0.63 using this method is shown in **Fig. 14**. This method will lead to a very small pore size for certain cases with a large number of small pores, such as the cases represented by the blue and green lines in **Fig. 14**. While such a small pore size, which is about less than 10nm may lead to an unstable bubble point pressure in our simulator. Thus, another representative pore sizes assignment method is introduced in this study. An example with a pore size distribution in using this new method is shown in **Fig. 15**.

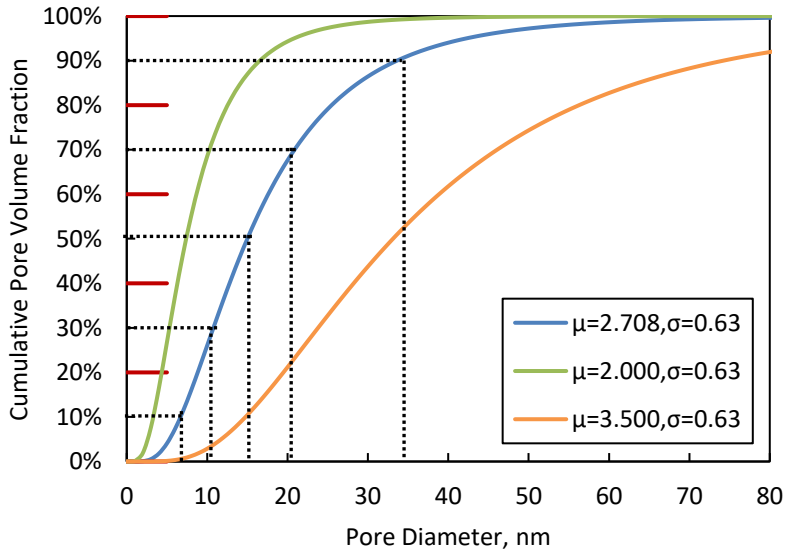

Fig. 14 Czernia (2018) assignment method of representative pore sizes for a lognormal distribution μ=2.708 and σ=0.63

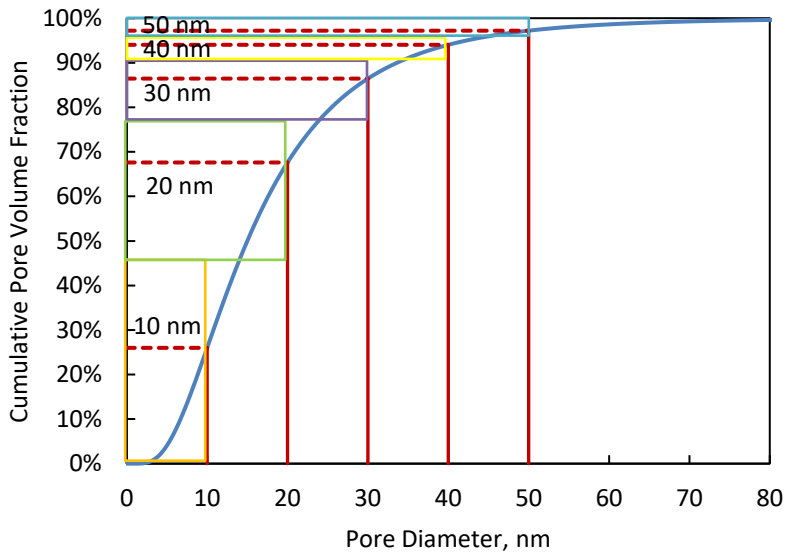

Fig. 15 New assignment method of representative pore sizes for a lognormal distribution μ=2.708 and σ=0.63

This method is to find the cumulative values of specified pore sizes first, and to arrange them from the smallest to the largest. Then to calculate the pore volume fraction for each pore sizes with the pore size distribution using the mathematical equations below:

$$f_1^V = \frac{1}{2}(CDF_1 + CDF_2) \tag{4.28}$$

$$f_{np}^V = 1 - \frac{1}{2}\left(CDF_{np} + CDF_{np-1}\right) \tag{4.29}$$

$$f_i^V = \frac{1}{2}(CDF_{i+1} - CDF_{i-1}) \qquad for \;\; 1 < i < np \tag{4.30}$$

The pore volume fractions occupied by the smallest pore size (f_1^V) is a half of the sum of cumulative volume fraction of the smallest pore size (CDF_1) and the secondly smallest pore size (CDF_2). And the pore volume fraction occupied by the largest pore size

(f_{np}^{V}) is the difference between 1 and a half of the sum of the largest pore size cumulative volume fraction (CDF_{np}) and the second largest pore size cumulative volume fraction (CDF_{np-1}). For the pore sizes between the smallest and the largest, the pore volume fractions occupied by that size of pores (f_{i}^{V}) are calculated as a half of the difference between the cumulative volume fractions of two nearest pore sizes, one is larger (CDF_{i+1}) and the other is smaller (CDF_{i-1}). As shown in **Fig. 15**, different boxes with different colors represent the pore volume fractions occupied by these five different pore sizes.

New assignment method of representative pore sizes is also used to determine pore size distribution models with different number of pore sizes. The smallest pore size used in this study is 10 nm, and the largest pore size used in this study is 200 nm. In order to investigate the effect of the number of pore sizes used in the simulation, several pore size models with different number of pore sizes are conducted as shown in the following table.

Table 12 Pore size models with different number of pore sizes

Types	1-pore-size	2-pore-size	3-pore-size	5-pore-size
Pore size and Pore volume fraction	26 nm (100%)	10 nm (54.4%)	10 nm (38.1%)	10 nm (31.2%)
		100 nm (45.6%)	30 nm (33.6%)	20 nm (17.3%)
			100 nm (28.3%)	30 nm (15.1%)
				50 nm (20.4%)
				200 nm (16.0%)

Table 12 continue

Types	10-pore-size	15-pore-size
Pore size and Pore volume fraction	10 nm (26.5%)	10 nm (26.5%)
	15 nm (10.3%)	15 nm (10.3%)
	20 nm (8.5%)	20 nm (8.5%)
	25 nm (6.9%)	25 nm (6.9%)
	30 nm (7.9%)	30 nm (5.7%)
	40 nm (8.2%)	35 nm (4.8%)
	50 nm (9.4%)	40 nm (4.0%)
	80 nm (8.1%)	45 nm (3.4%)
	100 nm (6.3%)	50 nm (4.1%)
	200 nm (7.9%)	60 nm (4.5%)
		70 nm (3.4%)
		80 nm (3.7%)
		100 nm (5.0%)
		150 nm (4.1%)
		200 nm (5.1%)

As shown in **Table 12**, the values in red are the pore sizes less than 50 nm, which are the majority of the pore sizes in the tight and shale plays, while the values in blue are the pore sizes larger than 50 nm, which are classified as macro pores. Since the nanopores occupied a large amount volume fraction in this sample, we increase the number of representative pore sizes for the nanopores firstly. And we increase the number of representative macropores later as the total number of representative pore sizes increases, which would result in a better description of the pore size distribution of this sample.

With the number of pores calculation mentioned in Chapter 3, for a 1 cm^3 sample with 1cm height, the pore numbers and pore volumes with the 3-pore-size model are shown in **Table 13**.

Table 13 Number of pores and pore volumes of a 1 cm^3 sample with 1cm height using the 3-pore-size model

Pore size	Pore volume, cm^3	Number of pores
10 nm	0.381	1.213×10^{13}
30 nm	0.336	1.189×10^{10}
100 nm	0.283	9.013×10^{10}

CHAPTER V

SENSITIVITY ANALYSIS OF MECHANISTIC MODEL

This chapter conducts sensitivity analysis for both depletion and injection to investigate the impacts of the depletion variables, such as effect of capillary pressure, pore size distribution, pressure decline steps and wettability angle, and injection variables, such as pore size distribution, injection dose per step, bottom-hole pressure (BHP) and injection fluid distribution. First of all, an analysis for the phase behavior and relative permeability under confinement were conducted.

5.1. Analysis for the Phase Behavior and Relative Permeability

Fig. 16 shows the computed phase envelopes of the 6-component fluid model in bulk and in confined spaces calculated by the VLE coupled with capillary pressure for different pore diameters. The solid lines in the figure represent bubble point curves while the dash lines represent dew point curves, the critical point is not affected by confinement unlike the shift method. As shown, the bubble point pressure is decreasing as the pore size decreases for a constant temperature, which is following the same trend in the experimental studies of the confinement effect. For example, the bubble point pressure of 10nm pores is about 1000 psia lower than that of the bulk at 165 °F (difference between cross point A and cross point B in **Fig.16**). And the dew point pressure is increasing insignificantly as the pore size decreases for a constant temperature.

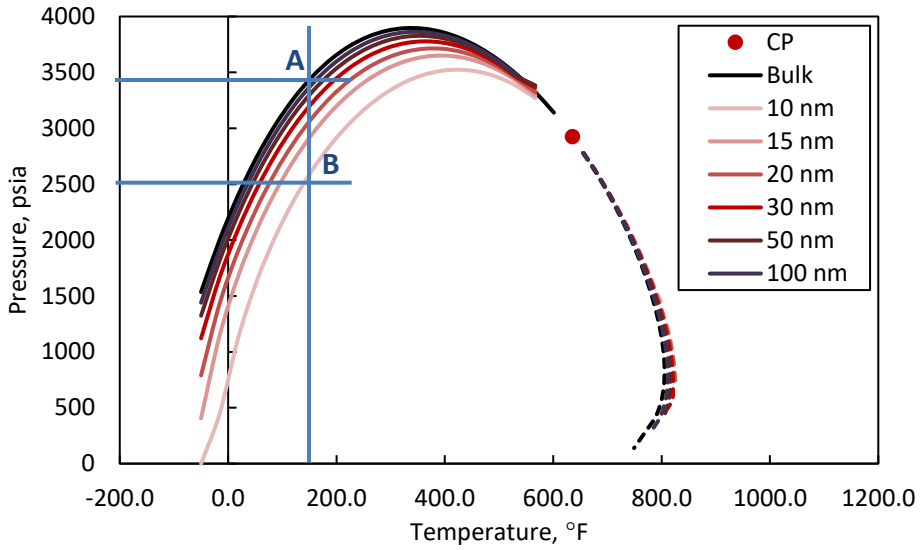

Fig. 16 Phase envelopes of the fluid in bulk and in confined spaces (solid lines represent bubble point curves, dash lines represent dew point curves).

In this study, since capillary pressure is calculated and updated coupling with the VLE calculation, the curves of capillary pressure versus oil saturation can be obtained for the depletion process. The curves generated here are based on a depletion from 3600 psia to 500 psia with a 31 psia pressure drop per step, and the regression model to fit the capillary pressure data is a rational polynomial model as indicated below:

$$P_c = \frac{a_1 + a_2 S_o^* + a_3 (S_o^*)^2 + a_4 (S_o^*)^3}{b_1 + b_2 S_o^* + b_3 (S_o^*)^2 + b_4 (S_o^*)^3 + b_5 (S_o^*)^4} \tag{5.1}$$

The relative permeability curves calculated using Eq.2.26-2.27 with this regression model usually converge after 4 iterations. With this relative permeability curve generation method, the relative permeability curves for each pore size distribution model with 6-component fluid model are calculated, as shown in the **Fig. 17**. The solid lines in represent oil relative permeability curves, while the dash lines represent gas relative permeability

curves. It is observed that the relative permeability curves using 1-pore-size model are quite different from the models with more pore sizes. This may because that the 1-pore-size model only has one nano-scale pore size while other models have at least one macro-scale pore size, which has impacts on both the phase behavior and depletion process. And it can be observed that at a higher oil saturation such as 0.98, the oil relative permeability with 2-pore-size model is larger than that with 1-pore-size model, indicating the oil is more mobile and much easier to be depleted when macro-scale pores exist. And at a lower oil saturation such as 0.88, the gas relative permeability with 2-pore-sizie model is smaller than that with 1-pore-size model, indicating that gas is less mobile and harder to be depleted when macro-scale pores exist. The curves for 2-pore-size and 3-pore-size overlapped each other. And beyond 5-pore-size models, there is no significant differences.

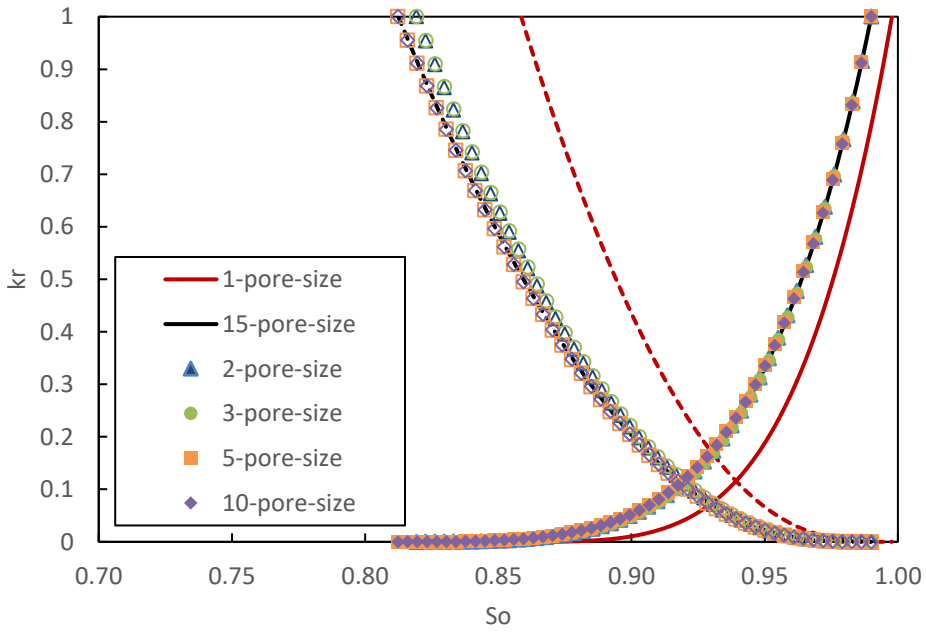

Fig. 17 Relative permeability curves for different pore size models

5.2. Analysis for the Depletion

5.2.1 Effect of Capillary Pressure and Production Modes

Depletion for the 6-component fluid model is conducted from an initial pressure (3600 psia) to a bottom-hole pressure (2000 psia) at a constant reservoir temperature (165 °F) with a pressure decline step (16 psia/step) under the three different production modes described before: constant composition (**CC**), preferential gas (**PG**) and relative permeability (**RP**). For the cases considering capillary pressure, the wettability angle is set to be 30°, which is a typical value in the literatures. For cases without capillary pressure, the relative permeability curves generated with the capillarity are used as a comparison. Only the two extreme pore size distribution models (1-pore-size model and 15-pore-size model) were used here, which are shown in **Fig. 18** and **Fig. 19**. Both figures show the effect of capillary pressure on oil recovery factor (oil RF), gas recovery factor (gas RF), gas-oil ratio (GOR) and residual oil composition under different production modes.

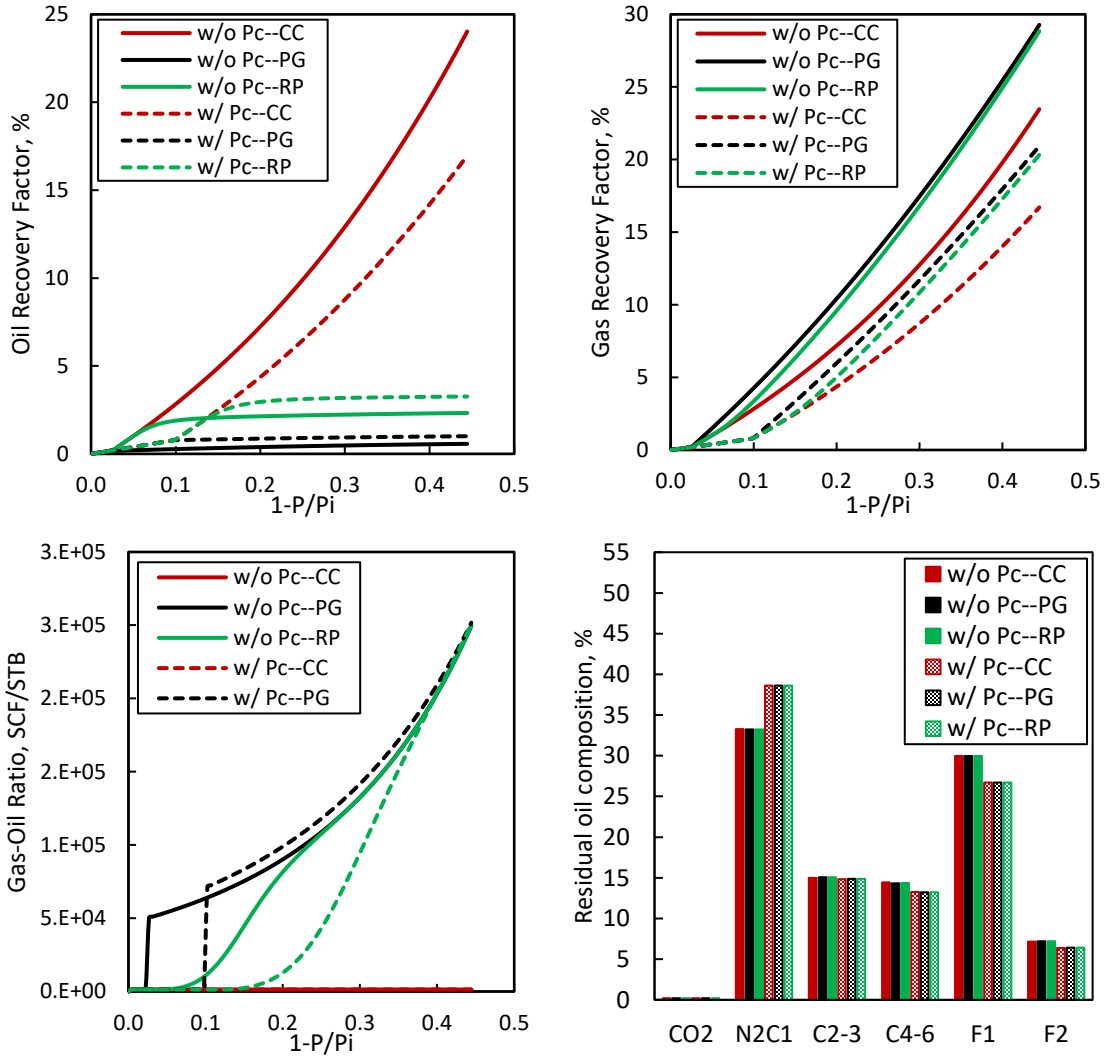

Fig. 18 Effect of capillary pressure on oil recovery factor, gas recovery factor, gas-oil ratio and residual oil composition using 1-pore-size model under different production modes.

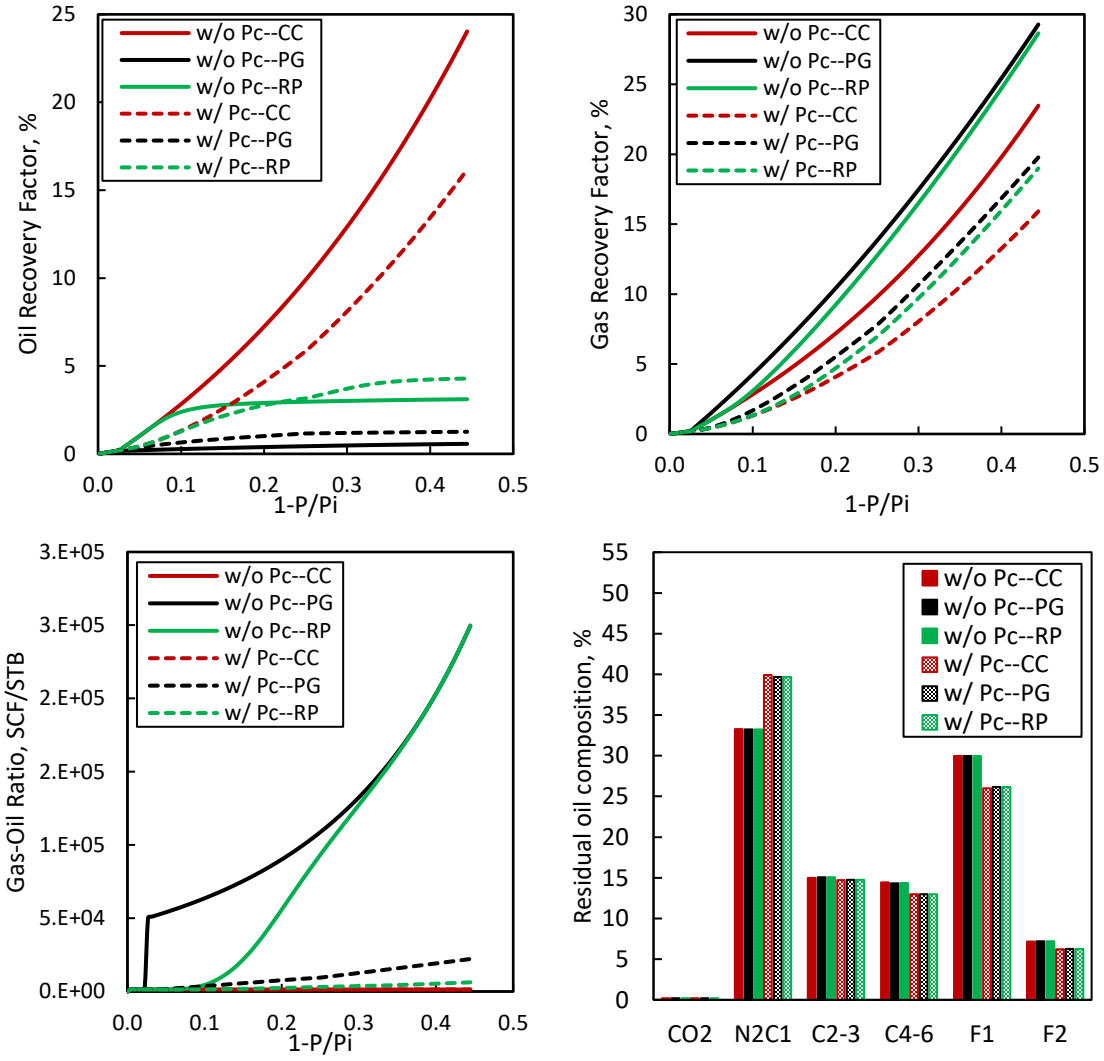

Fig. 19 Effect of capillary pressure on oil recovery factor, gas recovery factor, gas-oil ratio and residual oil composition with 15-pore-size model under different production modes.

The plots with 1-pore-size model and 15-pore-size model show the same trends for the effect of capillary pressure and different production mode on the oil RF, gas RF and residual oil composition, except the GOR. It is observed that the oil RF with capillary pressure is lower than that without capillary pressure under CC production mode, which is the most optimistic production mode, while the oil RF with capillary pressure is a little

higher than that without capillary pressure under PG production mode, which is the most pessimistic production mode. And under RP production mode, the oil RF with capillary pressure is lower than that without capillary pressure when the pressure drop is small, however as the pressure drop increases and $p < p_{bubble}$, the oil RF considering capillary pressure is higher than when it is neglected. The gas RF with capillary pressure is always lower than that without capillary pressure regardless which production mode is used. Additionally, a larger percentage of lighter-component (N2C1) and lower percentage of heavier-components (F1, F2) are remaining in place at the end of the depletion when capillary pressure is considered.

Huang et al. (2019) investigated the capillary pressure effect and pore size distribution on the well performance using compositional simulation coupled multi-porosity and EDFM method with the same reservoir fluid sample and pore size distribution data. Their results showed the same trend as the relative permeability production mode used in this study.

The CC mode and PG mode illustrate the two extreme boundaries of the production performance, and RP mode is located between these two boundaries and moving with different relative permeability curves.

The difference in GOR performance with 1-pore-size model and 15-pore-size model mainly due to the difference in vapor phase appearance condition which will be discussed in the following content.

5.2.2 Effect of Pore Size Distribution Model

Depletion conducted at the same condition in Chapter 5.2.1. All six different pore size distribution models developed in **Table 12** are used for this analysis. And the cases in this part are all conducted with capillary pressure at 30° wettability angle. For the relative permeability production mode, the relative permeability curves for each pore size distribution models generated in **Fig. 17** are used. The production performance with different pore size distribution models under CC, PG and RP modes are shown in **Fig. 20**, **Fig. 21**, and **Fig. 22**, respectively.

As shown in **Fig. 20**, both the oil RF and gas RF are changing slightly as number of pore sized increases until they converge, which resulting in a converged GOR and residual oil composition under CC production mode. However, the oil RF changes significantly while the gas RF is not as number of pore sizes increases until they converge, which also resulting in a converged GOR and residual oil composition under both PG and RP production mode as shown in **Fig. 21** and **Fig. 22**. Thus, it can be concluded that 5-pore-size model is sufficient to represent the pore size distribution for the reservoir sample in this study. It also observed that the performance with 1-pore-size model is with great difference comparing to other models, indicating that only one pore size to represent the reservoir is not reasonable.

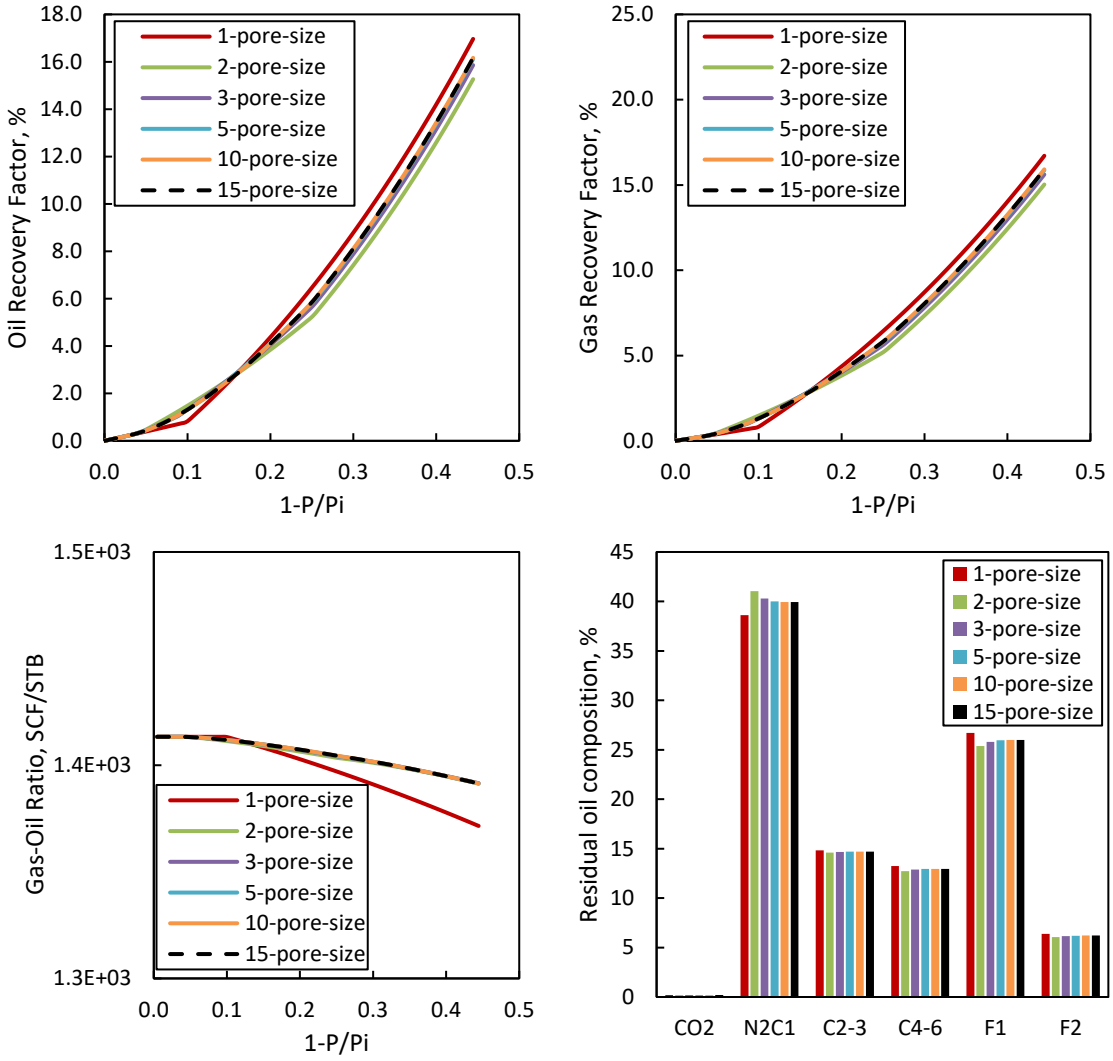

Fig. 20 Effect of number of pore sizes on oil recovery factor, gas recovery factor, gas-oil ratio and residual oil composition under constant composition production mode.

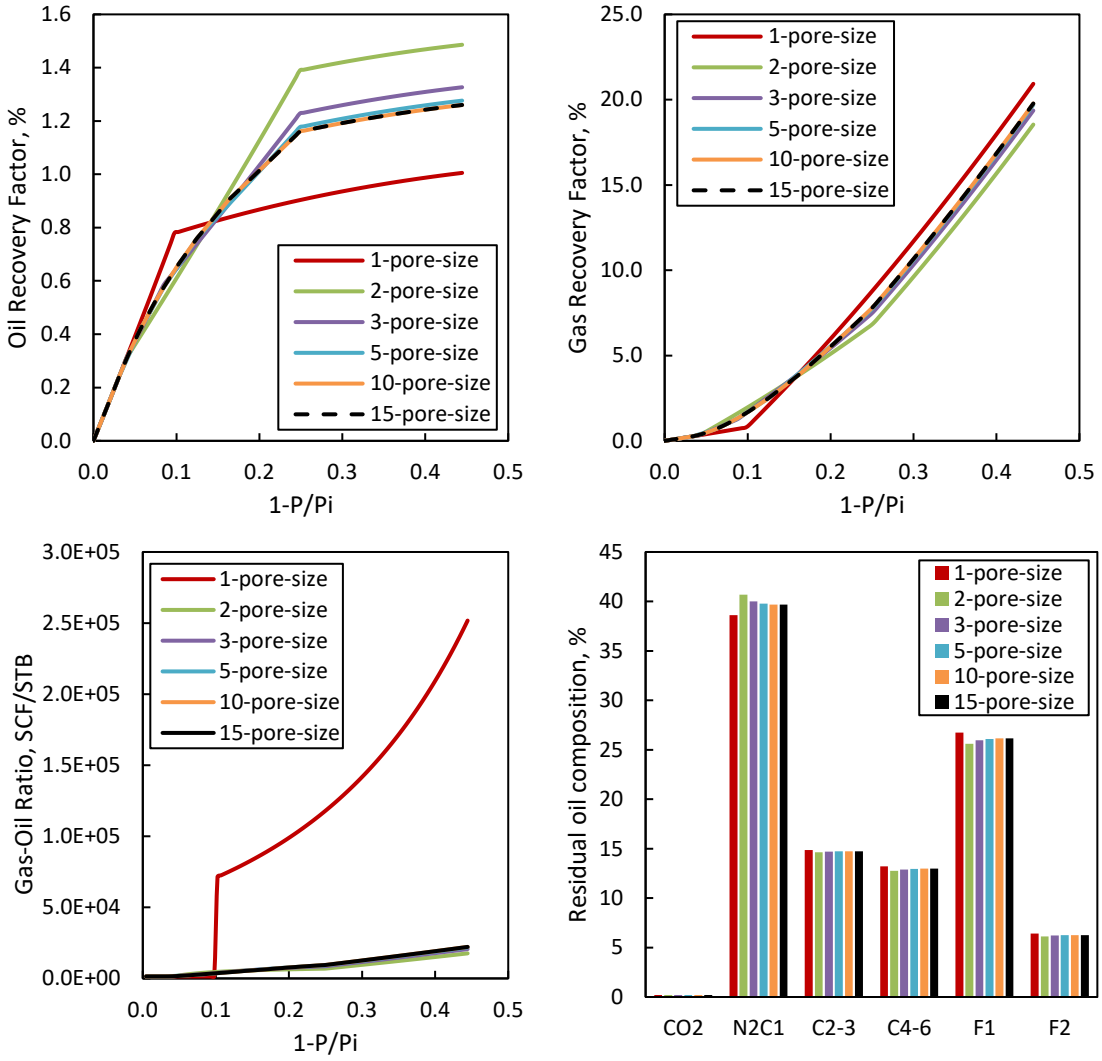

Fig. 21 Effect of number of pore sizes on oil recovery factor, gas recovery factor, gas-oil ratio and remaining moles in place under preferential gas production mode.

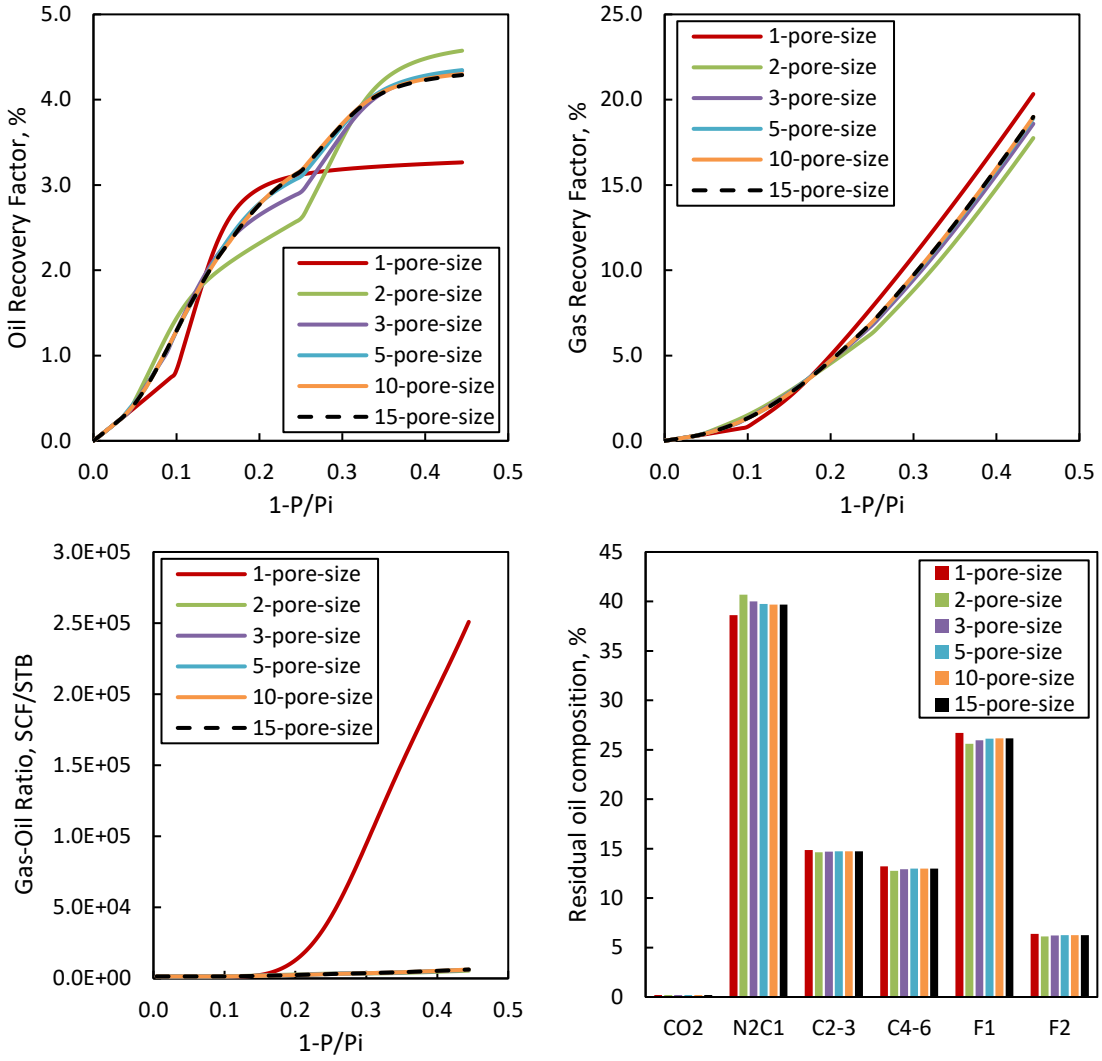

Fig. 22 Effect of number of pore sizes on oil recovery factor, gas recovery factor, gas-oil ratio and remaining moles in place under relative permeability production mode.

Fig. 23 shows the changes of oil RF, gas RF, GOR and residual oil composition in each size of pores with 5-pore-size model under RP production mode. It already observed that the bubble point pressure is decreasing as pore size decreases at constant temperature in **Fig. 16**. Thus, the fluid in smaller pores remains in liquid phase for a long time (larger pressure drops). As fluid in pores down into two-phase region, the excess volume is

increasing dramatically, resulting in a significant increase in oil production. **Fig. 23** also indicate that smaller pores achieve higher oil RF and lower gas RF. The residual oil in smaller pores are lighter than those in larger pores. The changes of the fluid composition during the depletion could be an important reason causing the differences in the production performance. Additionally, the observation with the mechanistic model in this study is following the same trend of that with compositional simulation for the same fluid sample and reservoir condition (Huang et al. 2019).

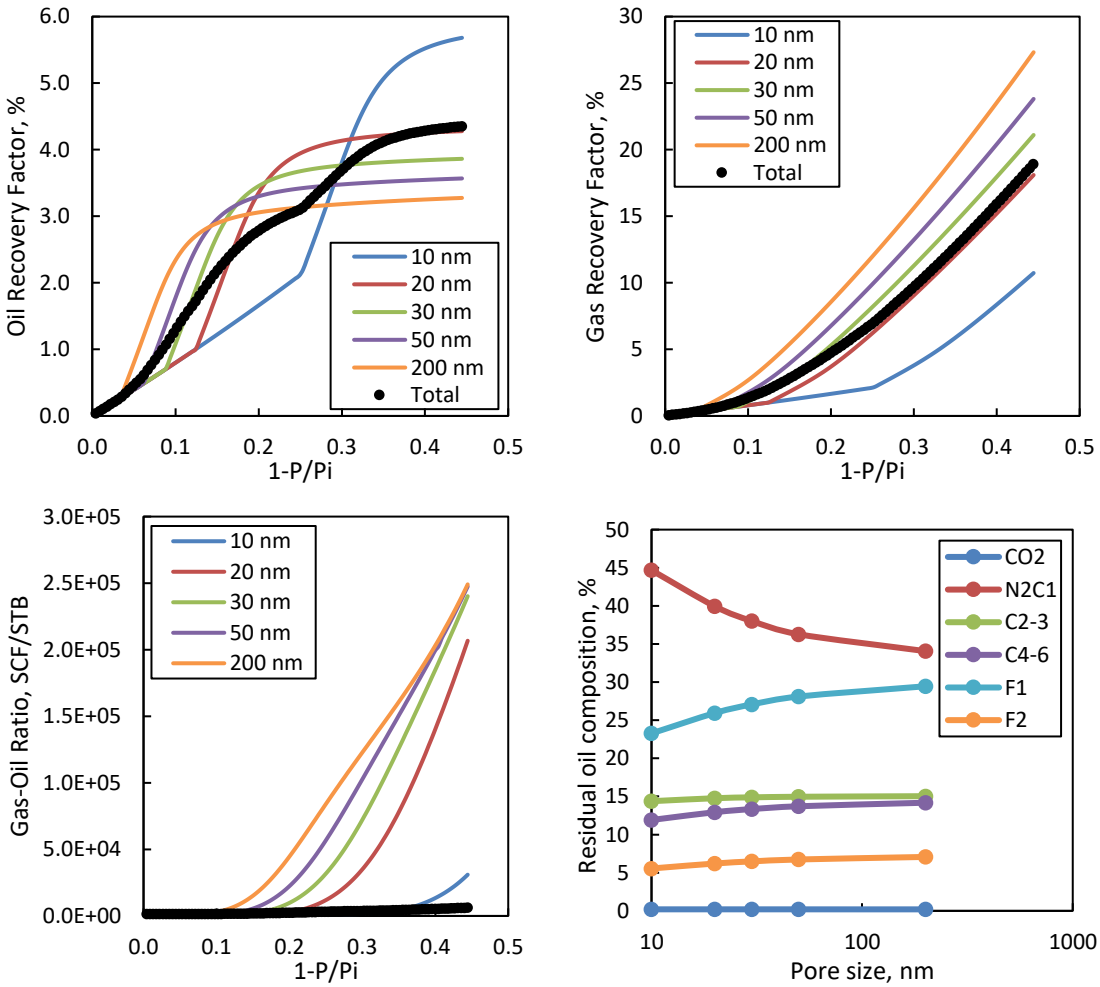

Fig. 23 Oil recovery factor, gas recovery factor, gas-oil ratio and residual oil composition in each size of pores with 5-pore-size model under relative permeability production mode

5.2.3 Effect of Pressure Decline Steps

Depletion for the 6-component fluid model is conducted with various pressure decline steps under relative permeability (RP) production mode with capillary pressure. Based on the discussion above, 5-pore-size model is in use for the analysis. Other conditions are as same as those in Chapter 5.2.1. The different pressure decline steps coincide with the number of depletion steps are shown in **Table 14** calculated using eq. 5.2.

$$\Delta p_{step} = \frac{p_i - BHP}{number\ of\ steps} = \frac{3600 - 2000}{number\ of\ steps} \tag{5.2}$$

Table 14 Pressure decline steps with different number of depletion steps

Number of Steps	**1**	**2**	**3**	**4**	**5**	**6**	**10**	**15**	**20**	**30**	**50**	**80**	**100**
Δp_{step} **(psia/step)**	1600	800	533	400	320	267	160	107	80	53	32	20	16

The production performance with different pressure decline steps with 5-pore-size model under RP mode with capillary pressure are shown in **Fig. 24**. As shown, the oil RF is increasing as the pressure decline step decreases until it converges to a maximum. While the gas RF decreases as the pressure decline step decreases, but the difference in the gas RF is negligible.

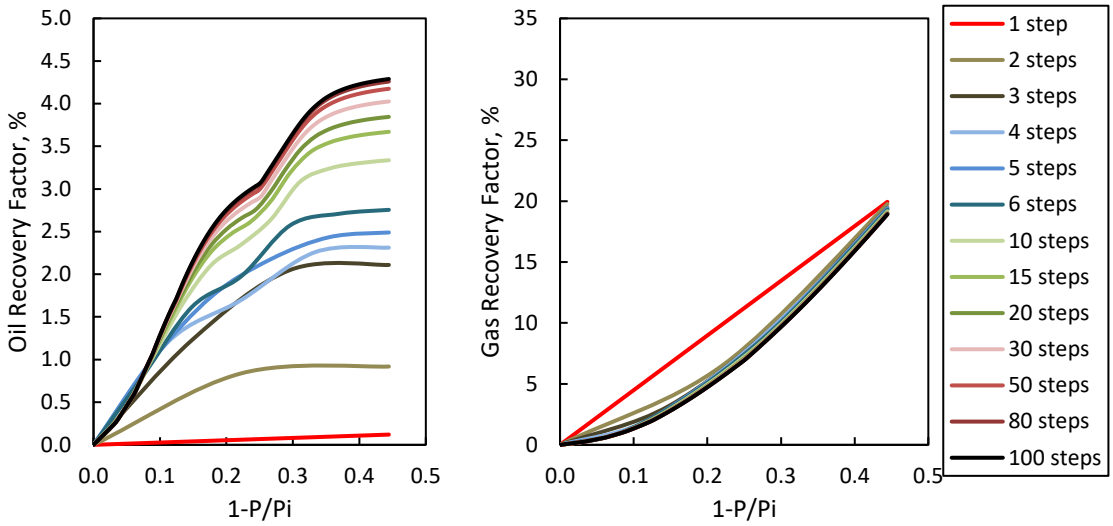

Fig. 24 Effect of number of depletion steps on oil recovery factor and gas recovery factor with capillary pressure (5-pore-size model) under relative permeability production mode.

5.2.4 Effect of Wettability Angle

Depletion for the 6-componet fluid model with capillary pressure is conducted at the same condition as Chapter 5.2.1. The wettability angle studied here are 30° and 60°. The relative permeability curves for the 1-pore-size model and 10-pore-size model with different wettability angle are shown in **Fig. 25**.

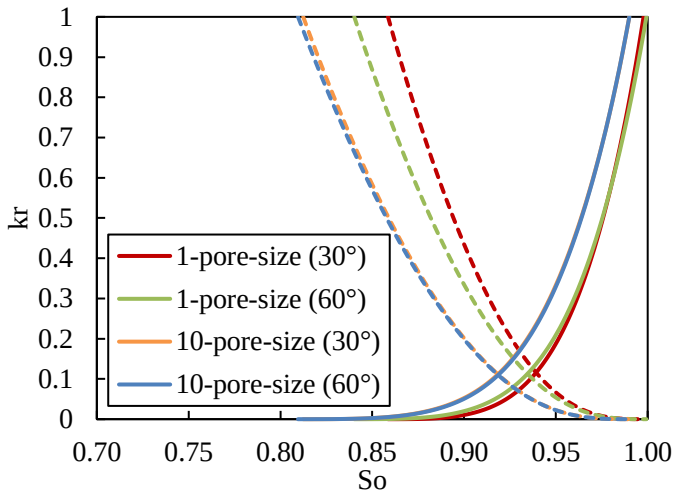

Fig. 25 Relative permeability curves for 1-pore-size and 10-pore-size models with different wettability angles (solid lines represent oil relative permeability curves; dash lines represent gas relative permeability curves).

As shown, for the 1-pore-size system, gas relative permeability is decreasing with increasing wettability angle at a constant saturation, which illustrates the gas become less mobile, while oil relative permeability is not affected by the changing wettability angle. However, the relative permeabilities for the 10-pore-size are almost the same with different wettability angle. The production performance with 1-pore-size model and with 10-pore-size model under RP production modes considering capillary pressure are shown in **Fig. 26**. Both results with 1-pore-size model and 10-pore-size model show the same trend for the effect of wettability angle. That is, as wettability angle increases, the oil RF is decreasing, and the gas RF is increasing. These results are following the similar trends as those with compositional simulation of Huang et al. (2020). The big difference is the GOR with different pore size distribution model, which mainly caused by the existence of macro pores in 10-pore-size model that counteract the confinement effect. Additionally, a

lower percentage of lighter-component such as N2C1, and larger percentage of heavier-component such as F1 and F2, are remaining in place as the wettability angle increases. That is, the residual oil become heavier as wettability angle increases.

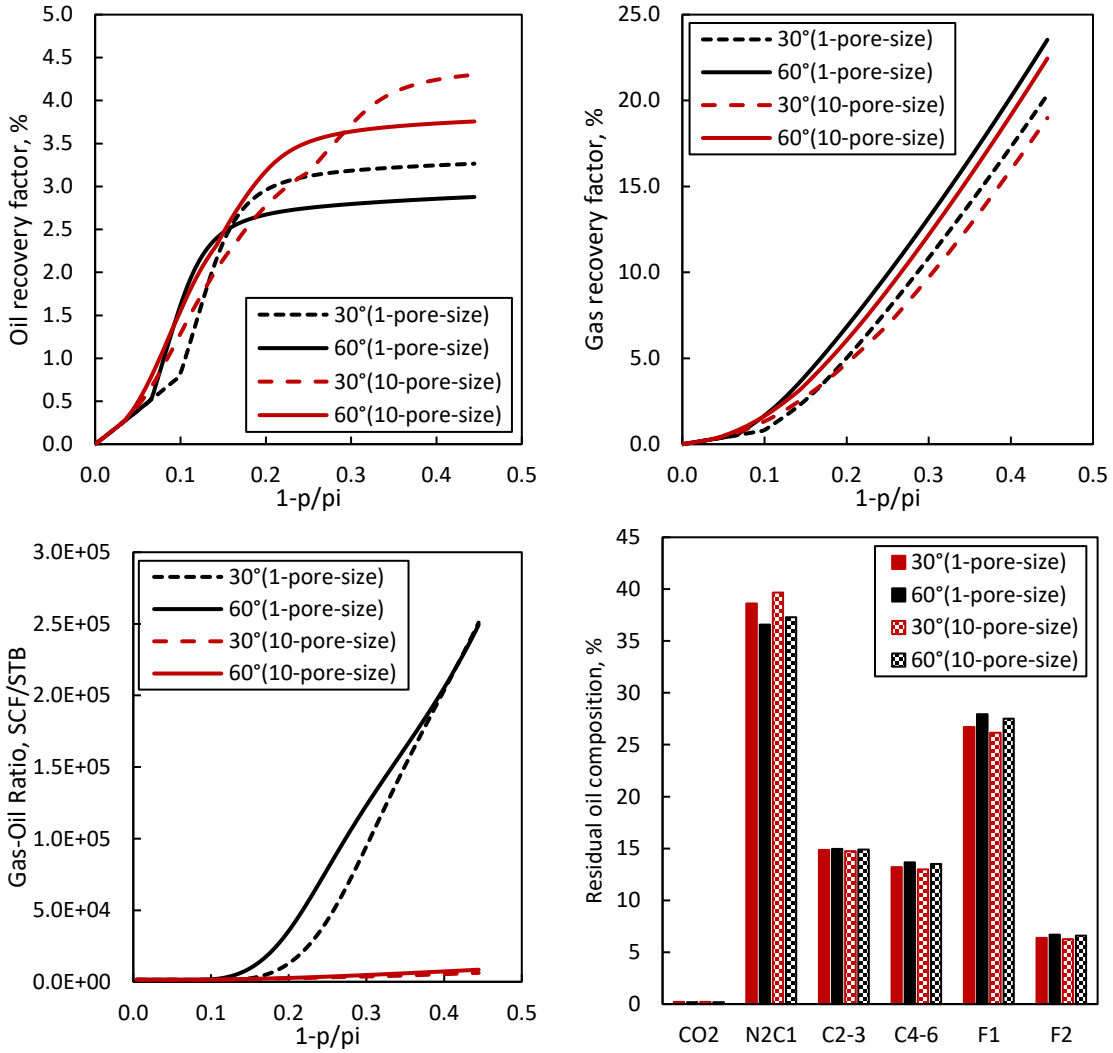

Fig. 26 Effect of wettability angle on oil recovery factor, gas recovery factor, gas-oil ratio and residual oil composition with 1-pore-size and 10-pore-size models under relative permeability production mode

5.3. Analysis for the Injection

5.3.1 Effect of Capillary Pressure and Production Modes

CO_2 injection for the 6-component fluid model is conducted after depletion with a constant reservoir temperature (165 °F) to investigate the effect of capillary pressure and production modes on the production performance. Depletion was conducted under relative permeability production mode. And the injection pressure is the end pressure at which depletion. Since the mechanistic model in this study is to simulate fluid huff-n-puff injection process, a prescribed proportion (dose) of injection fluid mixed with the fluid in place firstly. Then the excess volume with constant pressure (2000 psia) is depleted out. After that, a new dose (injection step) is conducted and repeated until the specified total injection amount is achieved. The pore volume injection distribution is used here. The relative permeability curves generation method for injection is meaningless due to the existing miscible conditions. Thus, only the two extreme production modes: constant composition (CC) or preferential gas (PG) are used for the injection to establish boundaries of the production performance. For the cases considering capillary pressure, the wettability angle is set to be 30°. And the injection rate is about 0.12 pore volume (PV) per step with 10 injection steps. Thus, the total pore volume injected into the system is about 1.2, which is the normal limit for the injection in the industry.

Note that since the initial fluid contains negligible percentage of CO_2, the gas recovery factor is calculated using the cumulative gas production excluding CO_2 from the produced gas.

Both 1-pore-size and 15-pore-size models were conducted for this analysis. The results with 1-pore-size model and 15-pore-size model are almost the same, thus only the results with 1-pore-size model are shown in **Fig. 27**. Under CC mode, the oil RF with capillary pressure is barely higher than that without capillary pressure, while the oil RF with capillary pressure is much higher than that without capillary pressure under PG mode. The gas RF with capillary pressure is always lower than that without capillary pressure under both production modes. In addition, a larger percentage of N2C1 and lower percentage of CO_2 and heavier components (F1, F2) are remaining in place when capillarity is considered. Pu et al. (2016) conducted a numerical simulation considers capillarity and adsorption effect of the small pores for shale reservoirs and found that model with capillarity would predict higher oil recovery by CO_2 injection than that without capillarity. The results with the mechanistic model in this study follow the same trend as the numerical simulation. Also as mentioned before in this chapter, the constant composition production mode is the most optimum condition, resulting in the highest oil RF and the lowest gas RF. While the preferential gas production mode is the most unfavorable condition, resulting in the lowest oil RF and the highest gas RF. In the reality, the production performance for gas injection to the unconventional reservoir is much more like the preferential gas production mode, since the low permeability make it hard for CO_2 moving far away from the injection well resulting most injected CO_2 will be depleted during the production.

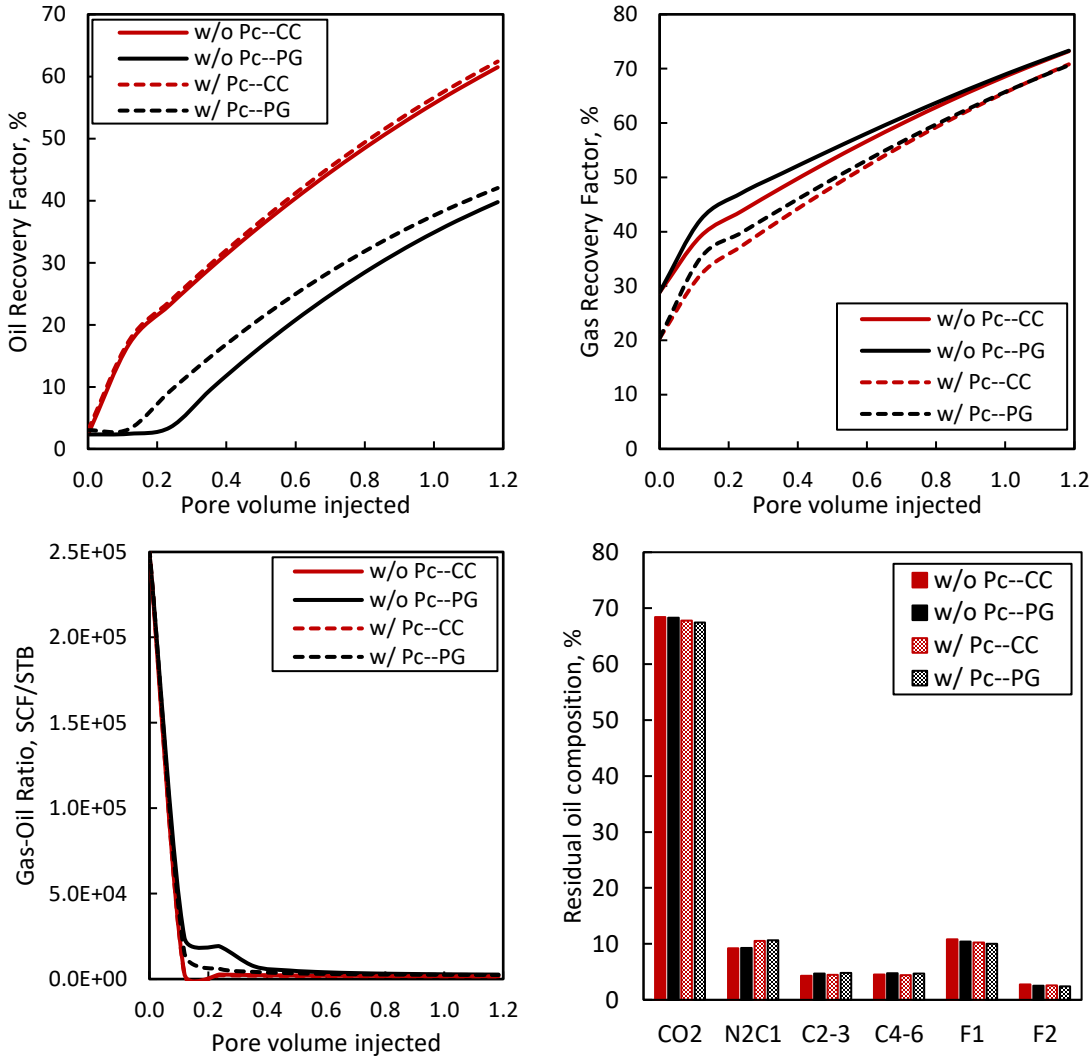

Fig. 27 Effect of capillary pressure on oil recovery factor, gas recovery factor, gas-oil ratio and residual oil composition with 1-pore-size model under different production modes (injection pressure is 2000 psia, injection fluid is CO_2)

Beside CO_2, CH_4 injection is also conducted here with the same condition as CO_2 injection. The results are shown in **Fig. 28**. Note that since produced gas contains injected CH_4, the gas recovery factor is larger than 100% here. It shown that when capillary pressure is considered, both oil and gas recovery factors are lower, and the residual oil becomes lighter as 1.2 pore volume CH_4 injected.

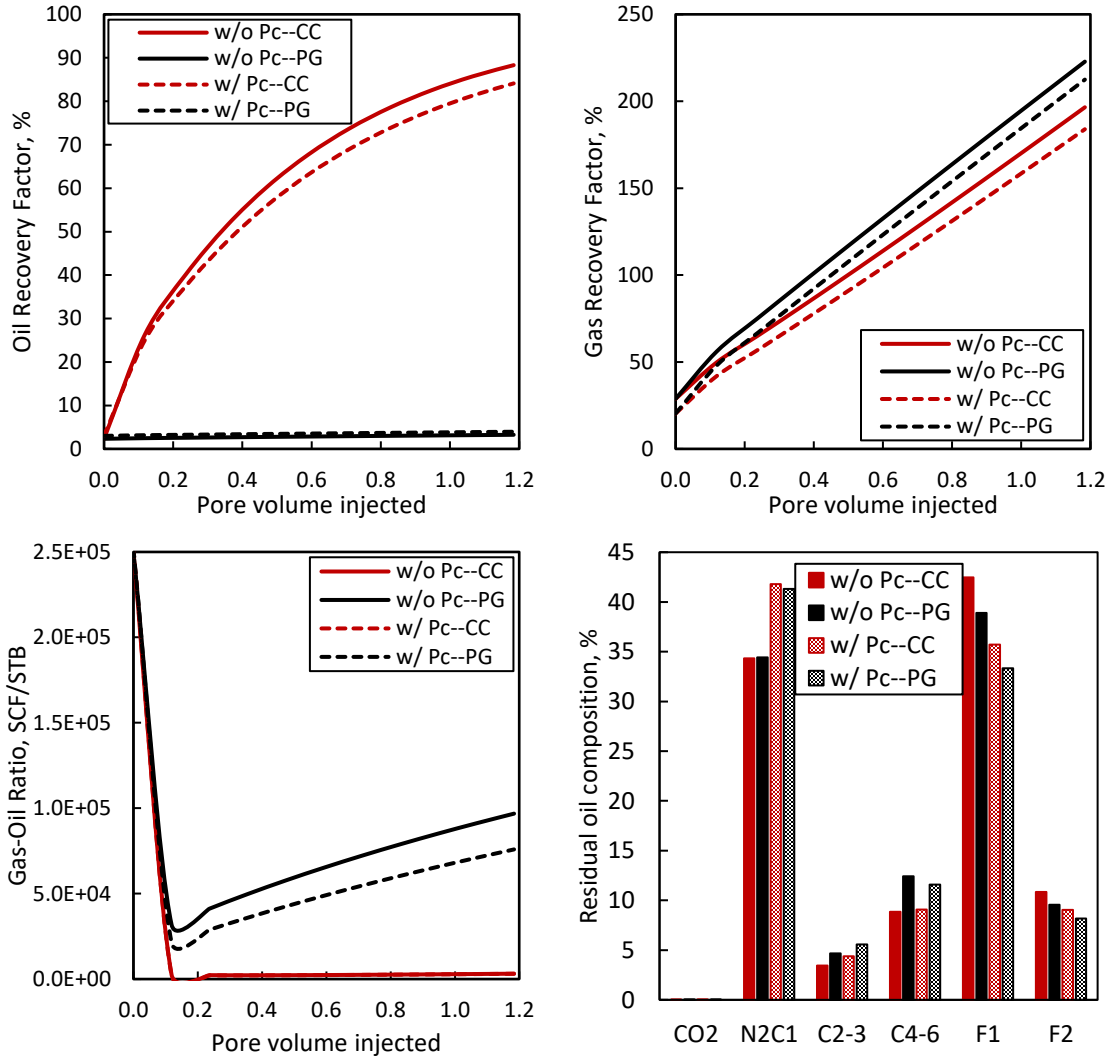

Fig. 28 Effect of capillary pressure on oil recovery factor, gas recovery factor, gas-oil ratio and residual oil composition with 1-pore-size model under different production modes (injection pressure is 2000 psia, injection fluid is CH_4)

5.3.2 Effect of Pore Size Distribution Model

CO_2 injection for the 6-component fluid model is conducted at the same initial conditions as Chapter 5.3.1, while the bottom-hole pressure here is 1500 psia. Only the cases with capillary pressure are conducted with different pore size distribution models developed in **Table 12** here to investigate the effect of pore size distribution model on the

production performance for injection. The production performance under CC mode shows no differences with different pore size distribution models, so only the results under PG mode is shown in **Fig. 29**.

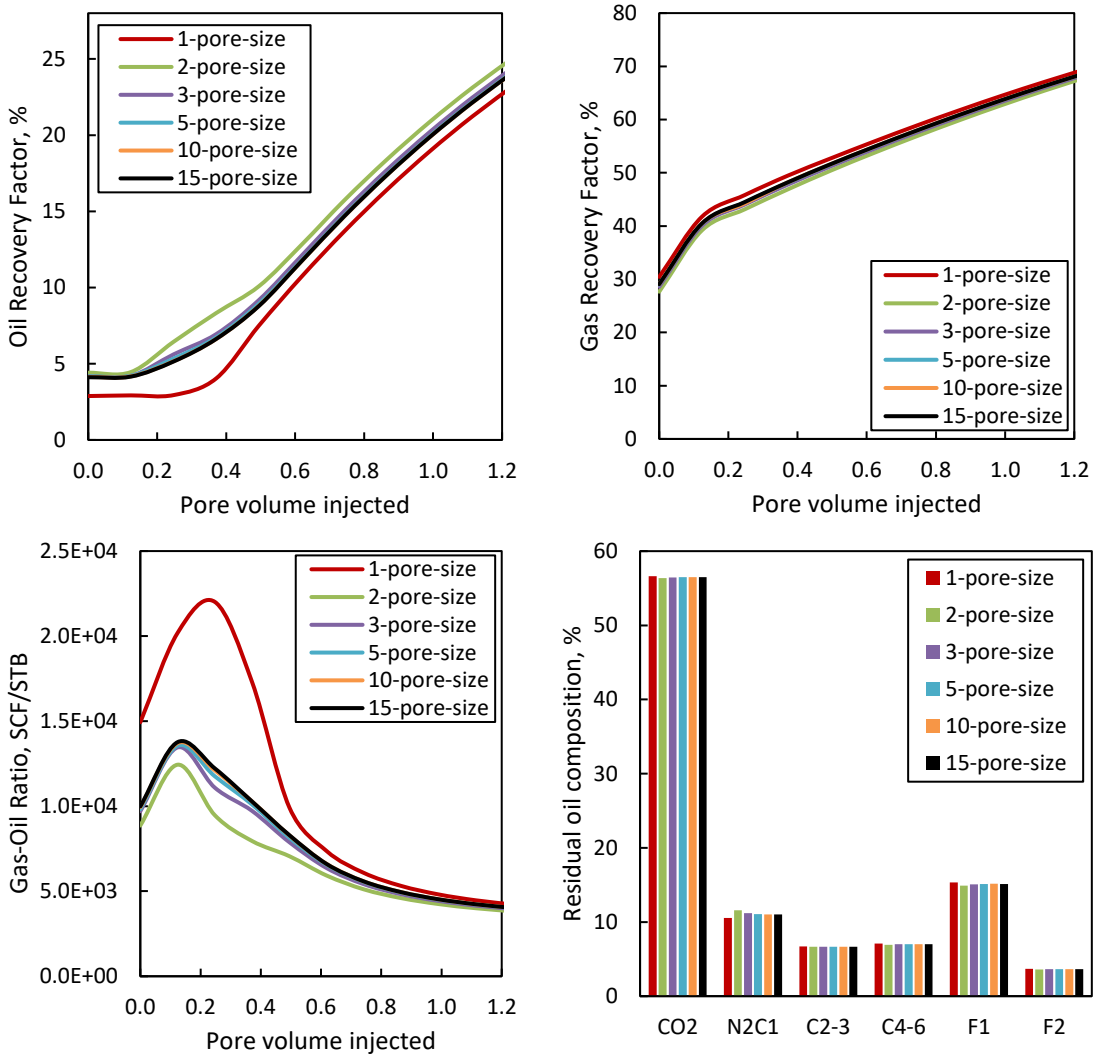

Fig. 29 Effect of number of pore sizes on oil recovery factor, gas recovery factor, gas-oil ratio and residual oil composition under PG mode (injection pressure is 1500 psia)

As shown above, the difference of the oil RF between these pore size distribution models at the end of injection is almost the same as that at the beginning of the injection.

And the oil production delay under PG mode becomes insignificantly as number of pore sizes increases. The number of pore sizes has no effect on the gas RF. Thus, the residual oil composition does not change significantly with increasing number of pore sizes. This phenomenon indicates similar miscibility between the residual fluid and CO_2 for all pore sizes, which suppresses the differences of capillary pressure impacts between different pore size distribution models. Thus, the pore size distribution has trivial impact on the production performance if pressure is close to above MMP. In this study, 5-pore-size model is sufficient to represent the pore size distribution of the sample.

Fig. 30 shows the changes of oil RF, gas RF, GOR and residual oil composition in each size of pores with 5-pore-size model under PG production mode. It is observed that the oil RF under PG mode is higher in smaller pores than that in larger pores while the gas RF is lower. And the oil production delay under PG mode becomes more significantly with the increasing pore sizes. Thus, the GOR in the larger pores changes dramatically than that in the smaller pores. Under PG mode, the residual fluid in smaller pores is lighter than that in larger pores. The observations at the end of the injection follows the same trend as those at the end of the depletion. Thus, the changes in the residual oil composition among the pores during the depletion could be an important reason causes the differences in the production performance of injection.

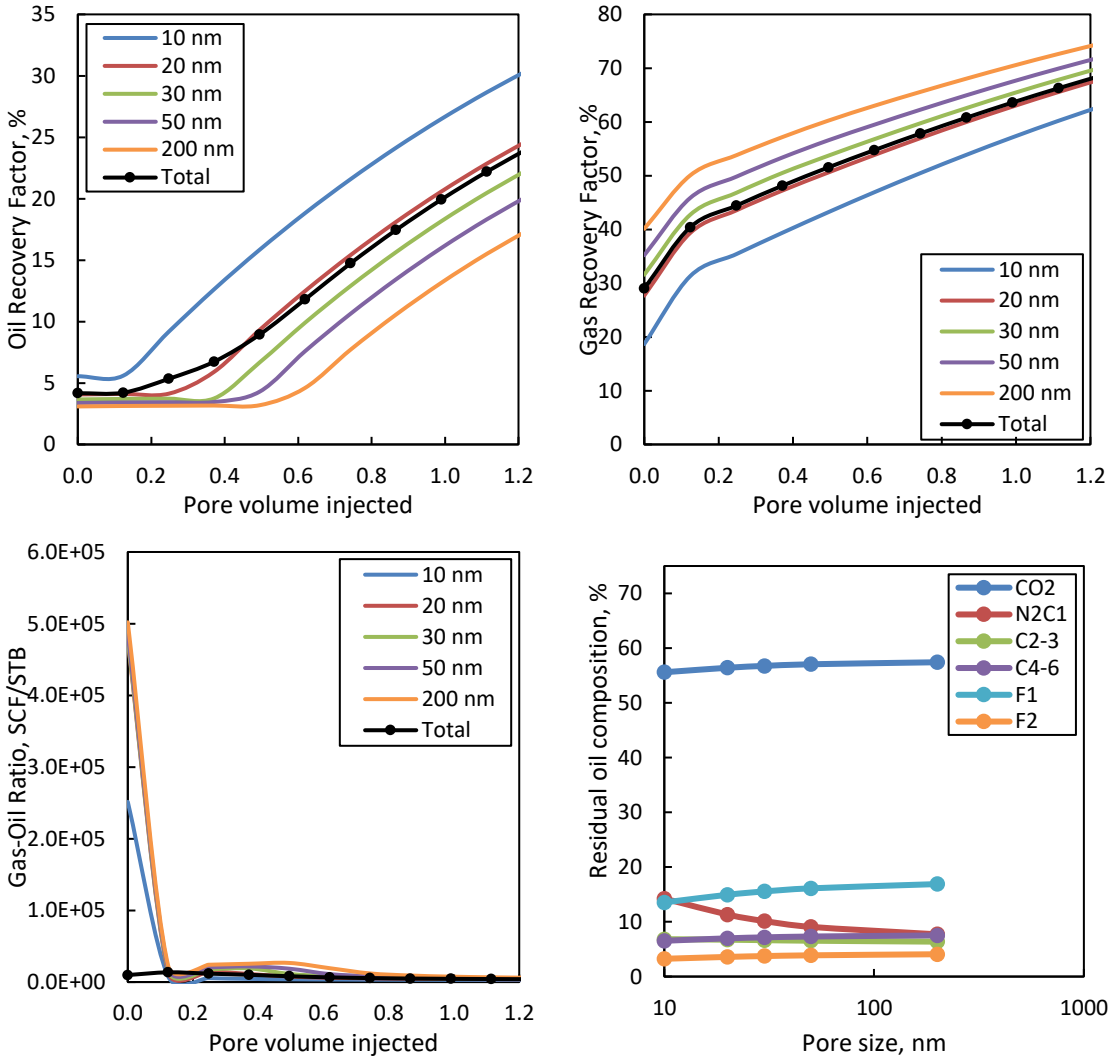

Fig. 30 Oil recovery factor, gas recovery factor, gas-oil ratio and residual oil composition in each size of pores with 5-pore-size model under PG mode (injection pressure is 1500 psia)

5.3.3 Effect of Injection Dose per Step

CO_2 injection for the 6-component fluid model is conducted with 5-pore-size model with capillary pressure at the same conditions in Chapter 5.2.1. The only changing variable is the injection dose per step. The injection dose per step definition here is molar ratio of the injection fluid versus initial fluid in place. The injection dose per step and the

number of injection steps changes simultaneously, keeping the total amount of injection fluid as a constant. The different injection dose per step coincide with the number of injection steps are shown in **Table 15**.

Table 15 Injection dose per step with different number of injection steps (total 1.2 pore volume CO_2 injected)

Case	Number of injection steps	Injection Dose (mol/mol of initial fluid)
2*0.60	2	0.600
5*0.24	5	0.240
10*0.12	10	0.120
20*0.06	20	0.060
50*0.024	50	0.024

The oil RF, gas RF, GOR and residual oil composition with different injection doses per step are shown in **Fig. 31**. It can be observed that the oil RF is increasing, and the gas RF is also increasing as injection dose per step decreases. And as the injection dose per step decreases to a specific value, both the oil RF and gas RF achieve convergence, which are the maximum of the RFs. As shown, with smaller injection dose per step, the gas production increases dramatically when CO_2 injection began, which illustrates that lighter components in place was displaced by the injected CO_2 at beginning of the injection. Thus, the GOR is increasing first and then decreasing as more CO_2 injected. Also, from the residual oil composition distribution, as injection dose per step decreases, the percentage of CO_2 in the residual oil is increasing, while the percentage of other components are decreasing. And the changes of residual oil composition are becoming insignificant as the injection dose per step decreases. It indicates that the lower injection rate of CO_2 could achieve higher oil and gas production and CO_2 sequestration.

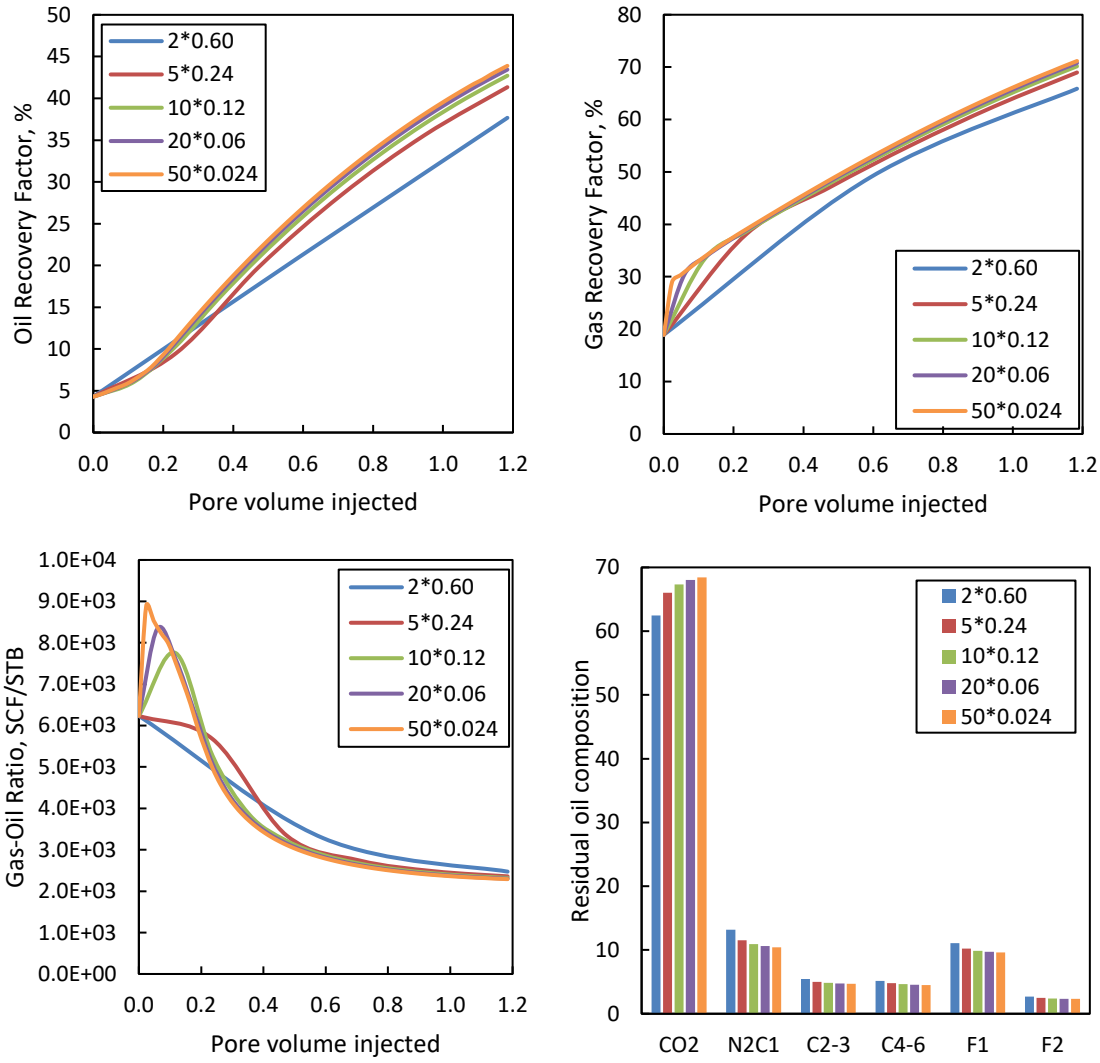

Fig. 31 Effect of injection dose per step on oil recovery factor, gas recovery factor, gas-oil ratio and residual oil composition with capillary pressure under PG mode (injection pressure is 2000 psia)

5.3.4 Effect of BHP/Injection Pressure

CO_2 injection for the 6-component fluid model is conducted with 5-pore-size model with and without capillary pressure at the same conditions as above. The primary changing variable in this part is the bottom-hole pressure, which is also the injection

pressure. The total pore volumes injected into the reservoir and pore volumes injected per injection step remains the same, but the mass injected as well as injection dose per step (moles injected/moles of initial fluid) is higher with higher bottom-hole pressure due to the dependence of the injection fluid phase behavior on the pressure. The number of injection steps is 10 and the pore volume injected per step is set to be around 0.12. Thus, the injection dose per step for BHP of 1000 psia, 2000 psia and 3000 psia are 0.05, 0.12 and 0.2, with a unit as mol/mol of initial fluid, respectively. For the case with 100 moles of initial fluid, the total injection moles of CO_2 for 1000 psia, 2000 psia and 3000 psia are 50 moles, 120 moles and 200 moles.

Table 16 shows the ultimate oil recovery factor with different bottom-hole pressure for the cases with or without capillary pressure under different production modes. At the end of depletion, the oil recovery factor is a little higher with lower BHP than those with lower BHP. And the cases with capillary pressure achieve higher oil recovery factor than those without capillary pressure with lower BHP (1000 psia and 2000 psia), while the case with capillary pressure achieve a little lower oil recovery factor than those without capillary with high BHP (3000 psia) mainly due to the BHP is located between the bubble point pressure without capillary pressure and that with capillary pressure. However, comparing to the improvement of the oil RF with injection, the difference in the oil RF at the end of depletion with different BHP is nearly negligible.

The cases under constant composition production mode for the injection achieve similar ultimate oil recovery factor as 1.2 pore volume CO_2 is injected when the BHP is increasing as expected. However, the ultimate oil recovery factor without capillary

pressure is not monotonic changing with the increasing BHP while that with capillary pressure is monotonic increasing as the BHP is increasing. This is probably due to the compositional changes during the phase transient, which is acceptable. As shown in **Fig. 32**, the residual oil when 1.2 pore volume CO_2 injected becomes lighter as BHP increases.

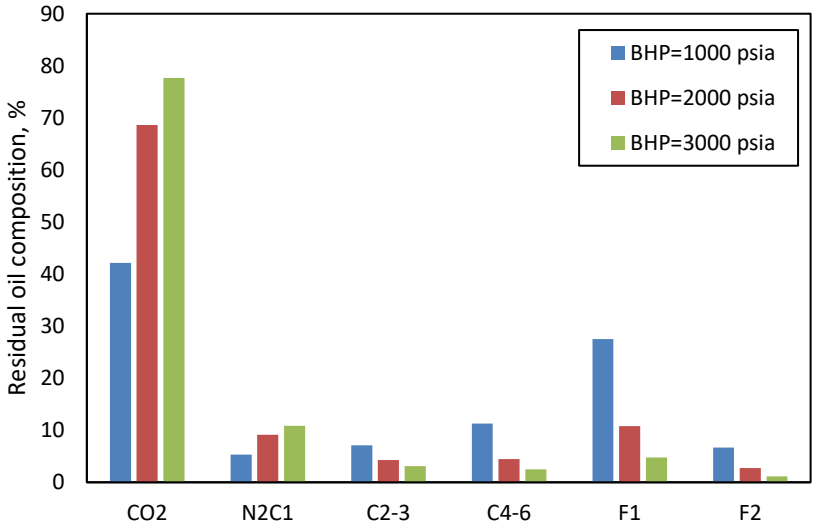

Fig. 32 Residual oil composition when 1.2 PV CO_2 injected with different BHP without capillary pressure under CC mode

For the cases under preferential gas production mode of the injection, the ultimate oil recovery factor as 1.2 pore volume CO_2 is injected is increasing dramatically as BHP increases. The significance of capillary pressure can only be appreciated at pressures lower than MMP, such as BHP is 1000 psia, while for higher pressures (2000 psia and 3000 psia), miscibility takes over.

Table 16 Ultimate oil recovery factor (RF) with different bottom-hole pressure (BHP), depletion was conducted under RP mode for all cases

BHP, psia	Production mode	Pc	Oil RF @end of depletion, %	Oil RF @ 1.2PV injection, %
1000	CC	w/o	3.22	64.22
2000			3.14	62.19
3000			2.85	65.93
1000		w/	4.39	53.37
2000			4.29	63.16
3000			2.40	66.35
1000	PG	w/o	3.22	3.28
2000			3.14	39.96
3000			2.85	64.68
1000		w/	4.39	8.00
2000			4.29	42.89
3000			2.40	65.94

Fig. 33 shows the oil saturation changes as CO_2 injected with different BHP under constant composition and preferential gas production mode, respectively. As shown, oil saturation changes are with great differences between two production modes, which reflect dramatic differences in the phase behavior under two production modes. When BHP is higher (2000 psia and 3000 psia), the mixtures of injection CO_2 and residual oil are almost in single phase (supercritical) along the injection under both production mode. Therefore, the oil recovery factor greatly improved after injection under preferential gas production mode. While for a low BHP (1000 psia), the oil recovery factor has little increasing after injection under preferential gas production mode.

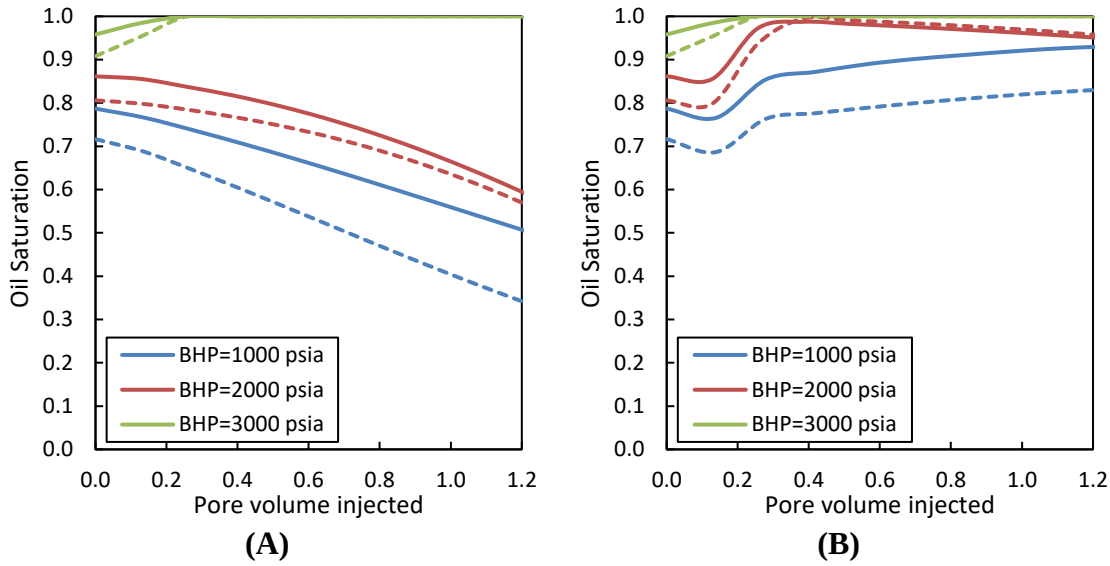

Fig. 33 Oil saturation vs. pore volume injected with different BHP under (A) constant composition and (B) preferential gas production mode, respectively (Solid lines are including Pc, and dashed lines without Pc)

Fig. 34 shows the oil density changes as CO_2 injected with different BHP under constant composition and preferential gas production mode, respectively. The oil density is increasing as more CO_2 injected. And the oil density with lower BHP is larger than that with higher BHP, as well as the oil density without capillary pressure is larger than that with capillary pressure. The oil density under both production modes has no significant difference.

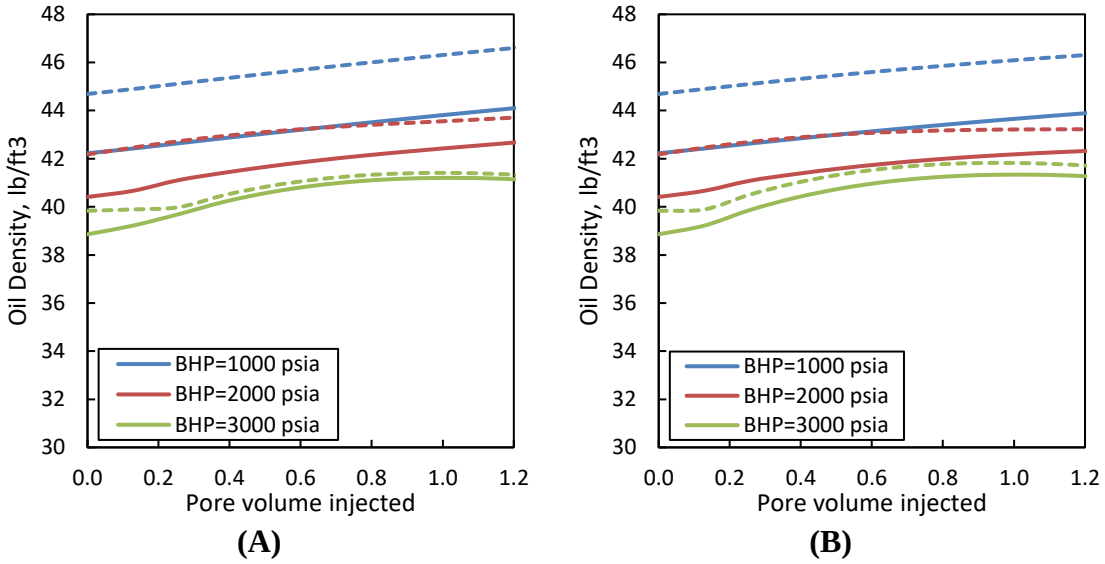

Fig. 34 Oil density vs. pore volume injected with different BHP under (A) constant composition and (B) preferential gas production mode, respectively (Solid lines are including Pc, and dashed lines without Pc)

The effect of injection pressure/BHP on oil recovery factor with 5-pore-size model for both depletion and injection are shown in **Fig. 35**. The difference of oil RF between two production modes is decreasing as BHP increases, which indicates that high BHP could suppress the impact of phase behavior changing and force miscibility between injection CO_2 and fluid in place.

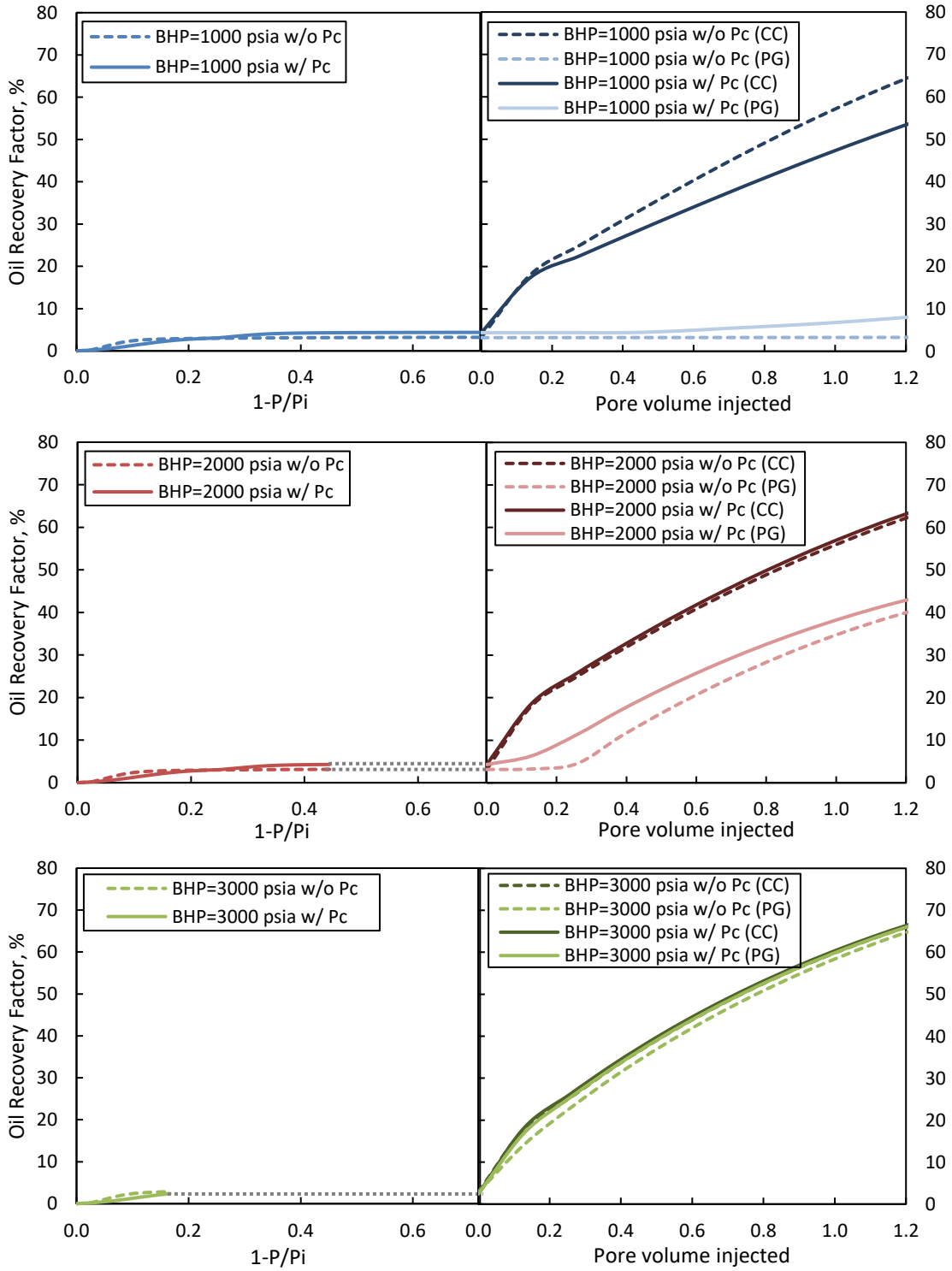

Fig. 35 Effect of injection pressure/BHP on oil recovery factor with 5-pore-size model, depletion was conducted under RP mode for all cases

Table 17 shows the ultimate gas recovery factor with different bottom-hole pressure for the cases with or without capillary pressure under different production modes. Distinct from the oil RF, the decreasing gas RF of the depletion with increasing BHP is not negligible. As shown, the gas RF decreases about 50% as the BHP increases 1000 psia in this study. Thus, the effect of BHP on the gas RF for the depletion should be take into consideration to analyze that for the injection. It observed that the ultimate gas RF at the end of injection is decreasing as BHP increases for the cases without capillary pressure. While the ultimate gas RF with capillary pressure has a trivial increase with the increasing BHP. And the difference of gas RF between the cases without and with capillary pressure is decreasing as BHP increases. The efficiency of the injection to improve the gas recovery, defined as the difference between the ultimate gas RF at end of injection and the gas RF at end of depletion, is increasing as BHP increases, which is about 26%, 51% and 67% when BHP are 1000 psia, 2000 psia and 3000 psia, respectively. **Fig. 36** shows the effect of injection pressure/BHP on oil recovery factor with 5-pore-size model for both depletion and injection.

Table 17 Ultimate gas recovery factor (RF) with different bottom-hole pressure (BHP), depletion was conducted under RP mode for all cases

BHP, psia	Production mode	Pc	Gas RF @end of depletion, %	Gas RF @ 1.2PV injection, %
1000	CC	w/o	56.80	82.05
2000			28.64	73.48
3000			7.01	71.17
1000		w/	39.78	69.02
2000			18.92	70.67
3000			3.41	70.63
1000	PG	w/o	56.80	78.48
2000			28.64	73.57
3000			7.01	72.03
1000		w/	39.78	65.99
2000			18.92	70.42
3000			3.41	70.91

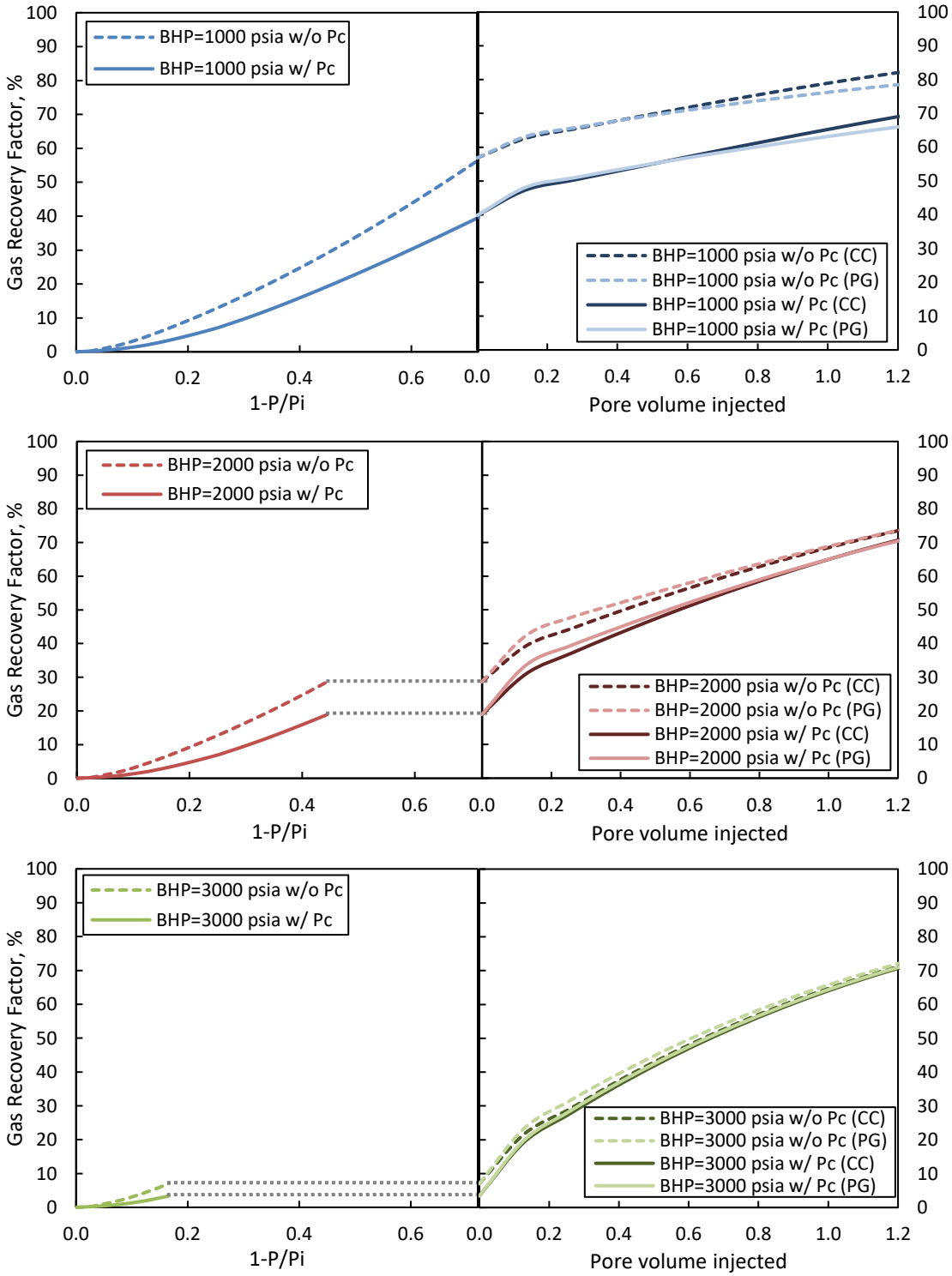

Fig. 36 Effect of injection pressure/BHP on gas recovery factor with 5-pore-size model, depletion was conducted under RP mode for all cases

5.3.5 Effect of Injection Fluid Distribution Model

The cases studied before are all using pore volume injection fluid distribution model, which assumes the volumetric amount of injection fluid into each size of pores is based on the pore volume fraction of that size of pores. In this chapter, the pore opening model is also studied with 6-component fluid model and 10-pore-size model at the same condition as Chapter 5.3.1 with capillary pressure.

The injection CO_2 distribution in each size of pores for 10-pore-size model with two different injection fluid distribution models is shown in **Fig. 37**.

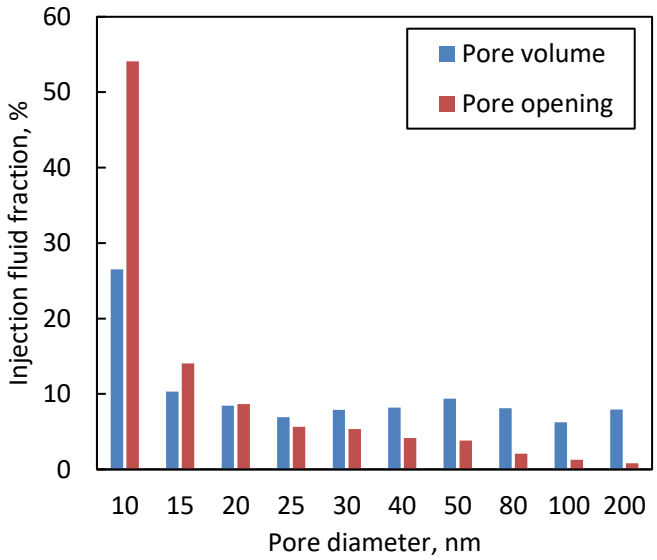

Fig. 37 Injection CO_2 distribution in each size of pores for 10-pore-size model with pore volume distribution model and pore opening distribution model, respectively

As shown, more CO_2 is injected into the smaller pores with pore opening distribution model since a larger number of smaller pores exists in the system. **Fig. 38** shows the effect of injection fluid distribution models on oil RF, gas RF, GOR and residual oil composition with 10-pore-size model under PG production mode. As shown, the oil

RF with pore volume distribution model is much higher than that with pore opening model. And the gas RF with pore volume model is a little higher than that with pore opening model. A larger percentage of CO_2 and lower percentage of other components are remaining in place with pore volume model comparing to those with pore opening model.

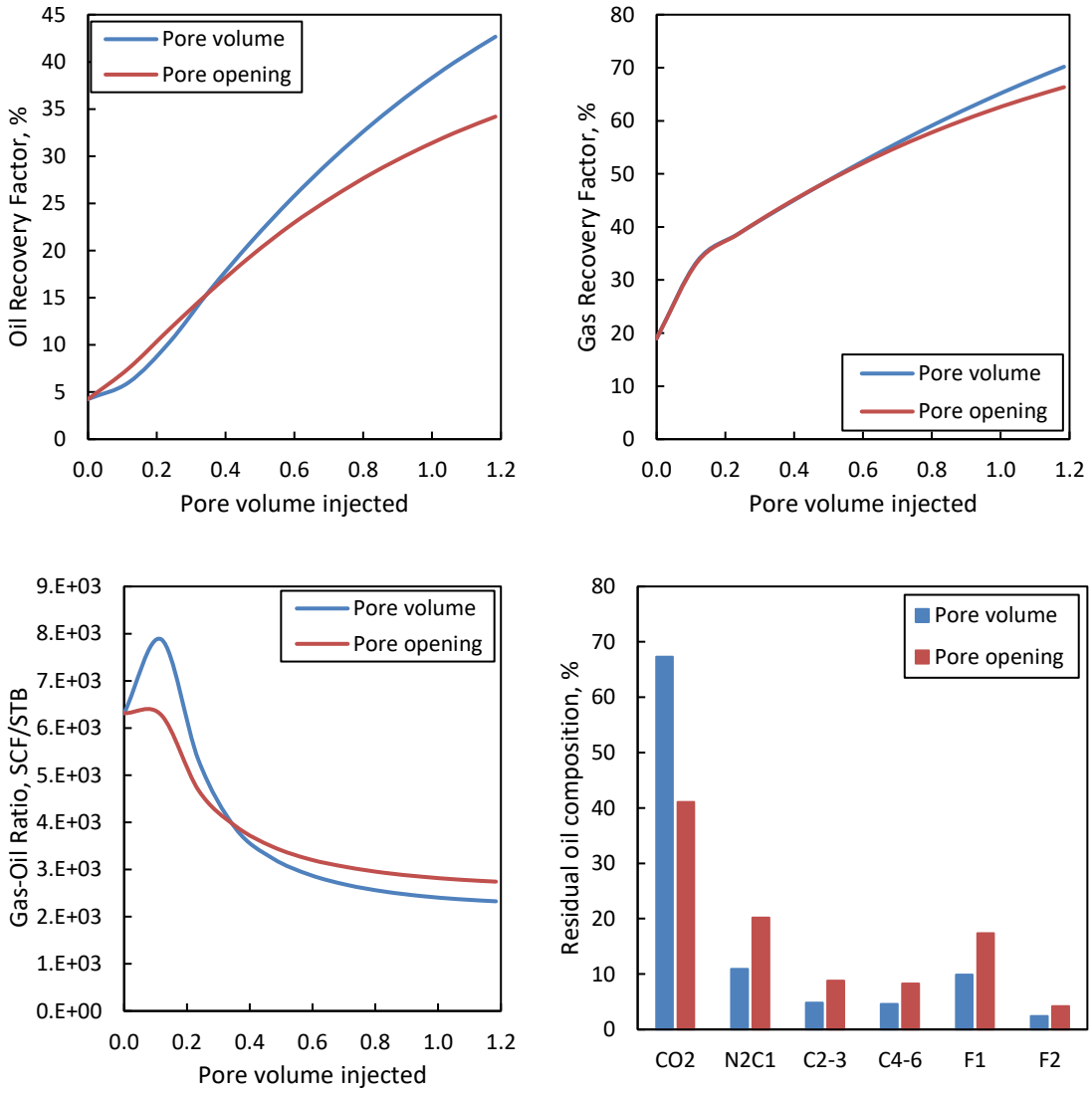

Fig. 38 Effect of injection fluid distribution models on oil recovery factor, gas recovery factor, gas-oil ratio and residual oil composition with 10-pore-size model under preferential gas production mode (injection pressure is 2000 psia)

Additionally, the residual oil composition with different injection fluid distribution models for each size of pores are shown in **Fig. 39**. It can be observed that the residual fluid composition with pore volume distribution model have trivial differences among all pore sizes, while those with pore opening distribution model have significant differences among the pores. Since different injection fluid distribution model causes different mixing ratio between the injection fluid and residual fluid, which further affects the miscibility and phase behavior of the mixtures in the pores. Thus, the production performance and remaining fluid for each step of injection are different. And the effect of the injection fluid distribution model will be cumulated to the next step of injection until the end of the process.

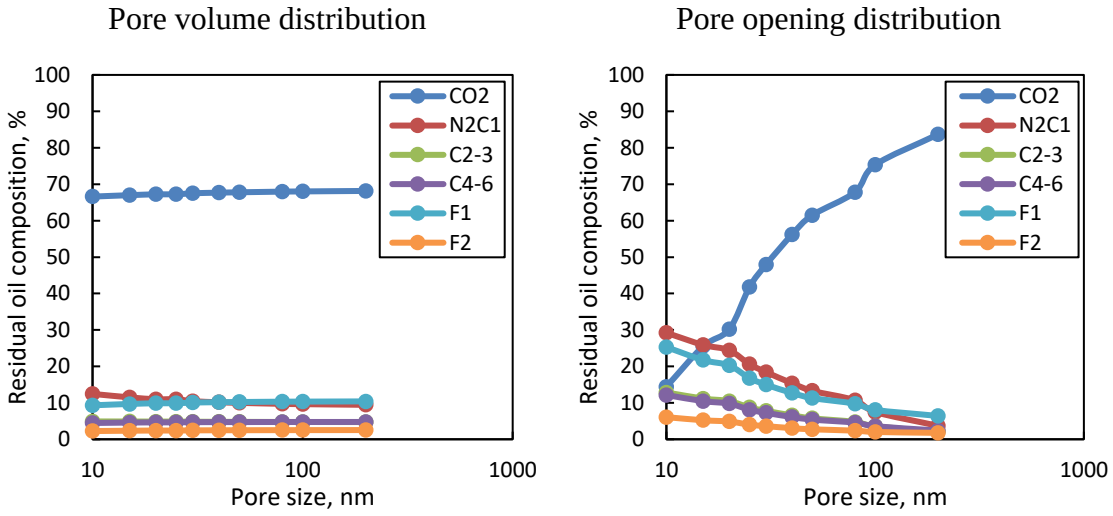

Fig. 39 Effect of injection fluid distribution modes on residual oil compositional distribution with 10-pore-size model under preferential gas production mode (injection pressure is 2000 psia)

CHAPTER VI

APPLICATIONS OF THE MECHANISTIC MODEL

The mechanistic model developed in this study has been introduced and analyzed in the previous chapters. This chapter is to discuss the application of this mechanistic model for the field use.

6.1. Ultimate Recovery Prediction

First of all, the mechanistic model for depletion could predict the ultimate oil and gas recovery as the average pressure of the whole reservoirs declines from the initial pressure to the bottom-hole pressure. A simple homogeneous square reservoir model is shown in **Fig. 40** with the basic parameters described in **Table 18**. **Fig. 41** shows a comparison of the oil and gas recovery factors predicted by the mechanistic model and Eclipse compositional simulator (E300) for this reservoir model with the reservoir fluid model developed in Chapter 4 taking capillary pressure into the consideration or not.

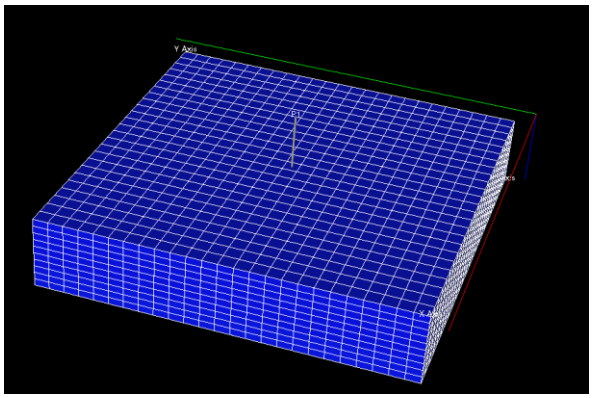

Fig. 40 A diagram of the structure and well location of the reservoir model

*Part of the data reported in this chapter is reprinted with permission from "Huang, J., Jin, T., Chai, Z., Barrufet, M. and Killough, J., 2019. Compositional simulation of fractured shale reservoir with distribution of nanopores using coupled multi-porosity and EDFM method. *Journal of Petroleum Science and Engineering*, *179*, pp.1078-1089" Copyright [2019] by Elsevier B.V.

Table 18 Basic parameters for the reservoir model

Initial Pressure (psia)	3600
Initial Temperature (°F)	165
Produced BHP (psia)	2000
Average Permeability (mD)	0.0185
Porosity	0.15
Grid number	25×25×10
Grid size (ft)	100×100×25

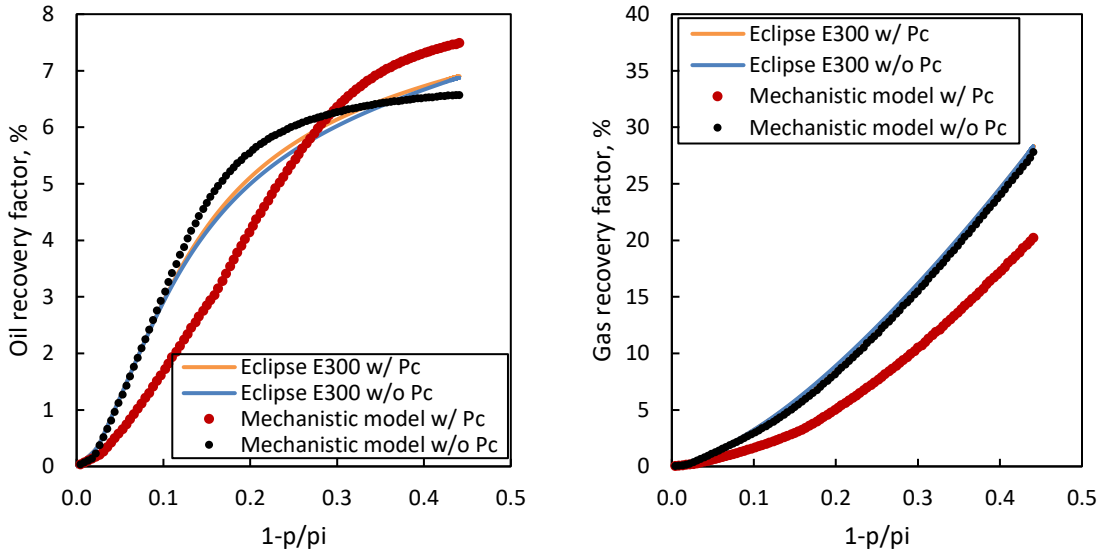

Fig. 41 Comparison of the predicted oil and gas recovery factors without or with capillary pressure by the mechanistic model and Eclipse E300 simulator, respectively.

As shown, the predicted ultimate recovery factors by mechanistic model are in a good match with those predicted by the commercial compositional simulator when capillary pressure is not taken into consideration. However, with the capillary pressure, the predicted results from mechanistic model is higher than that from the Eclipse E300. This is mainly because that Eclipse E300 only take the effect of the capillary pressure on the fluid flow rather than that on the phase behavior of the reservoir fluid. Thus, mechanistic model with capillary pressure and pore-size distribution into consideration is

much more reasonable to predict the production performance of the tight and shale reservoirs.

6.2. Well Production Performance Prediction

The mechanistic model developed in this study is a model which does not include the model to describe the fluid flow in the unconventional reservoir. To connect the mechanistic model with the field application, the correlations between the flowrate or pressure and time depending on the geological properties and well designs for the reservoirs, such as decline curves, some analytical models, or correlations regressed based on the field data were introduced into the mechanistic model here. Thus, the mechanistic model could predict the production performance for the specific reservoir with such fluid flow properties. Then the mechanistic model could give a rapid prediction and estimation of the performance changing with different operation conditions, which is of vital importance in the field operation to optimize the production process.

6.2.1 Decline Curves

Different decline curve analysis methods have been proposed to predict production performance of both conventional and unconventional reservoirs, which ranges from empirical to seme-empirical and theoretical. Arps (1944) published three empirical equations to predict production performance of wells, which are shown in **Table 19**. These equations were valid for production at constant bottom-hole pressure, assuming the reservoir and fluid properties were constant throughout the life of the well.

Table 19 Equation for exponential, hyperbolic and harmonic (Arps, 1944)

Exponential Decline	Hyperbolic Decline	Harmonic Decline
$q = q_i e^{-D_i t}$	$q = q_i[1 + bD_i t]^{-1/b}$	$q = q_i[1 + D_i t]^{-1}$
$D = D_i$	$D = aq^b, D_i = aq_i^b$	$D = aq^b, D_i = aq_i^b$
$D = D_i$	$D = \frac{1}{\frac{1}{D_i} + bt}$	$D = \frac{1}{\frac{1}{D_i} + t}$

In the equations, q is production rate, q_i is initial production rate, t is time, D is the instantaneous decline rate, D_i is the initial decline rate, and b is the decline exponent.

Gupta et al. (2018) analyzed various proposed historical decline curve analysis methods and found that both the linear flow regimes and changes in fracture conductivity with time follow a power-law function. Thus, Arps Hyperbolic, Power-Law Exponential, Stretched-Exponential Decline and Duong methods achieved successful application. Thus, in this study Arps hyperbolic decline was fitted with the fluid flow data from the Eclipse compositional simulator in chapter 6.1, as shown in **Fig. 42**. With fitted decline curves, cumulative oil production could be calculated by integration of the oil flowrate. Then, the time for a certain cumulative oil production in the mechanistic model could be obtained. Thus, the production performance with decreasing pressure could be translated to the production performance with time. The comparison of the predicted oil recovery factors by the mechanistic model with Arps hyperbolic decline curve and Eclipse E300 are shown in **Fig. 43**. It can be observed mechanistic model with the Arps hyperbolic decline curve shows a good match with the commercial simulator for the early time, but the late time matching is not that good.

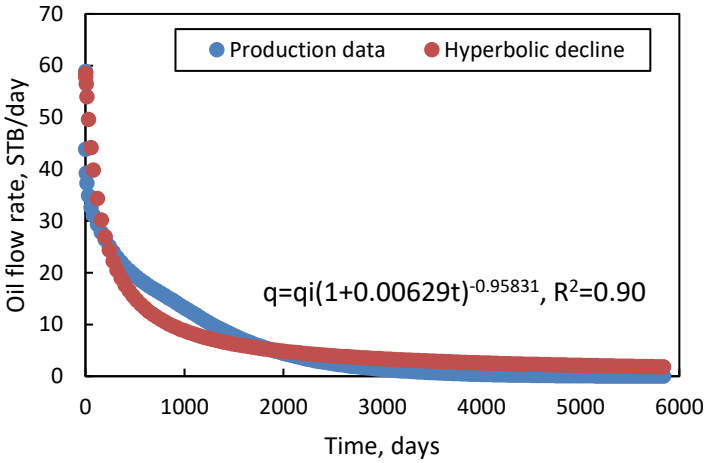

Fig. 42 Fitting plots of the relationship between the oil flowrate vs. time with Arps hyperbolic decline equation

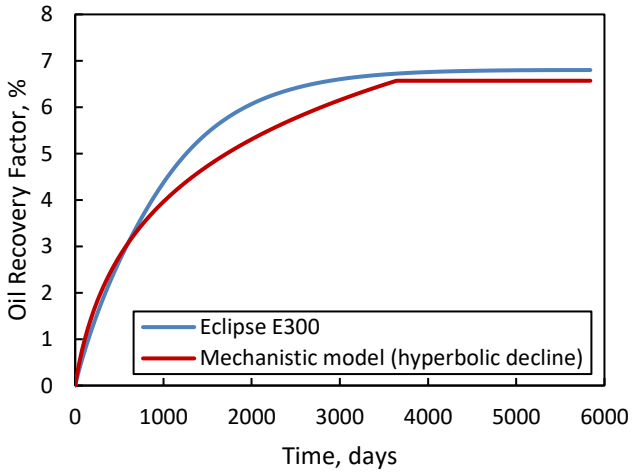

Fig. 43 Comparison of the predicted oil recovery factors by the mechanistic model and Eclipse E300 (time and flowrate for mechanistic model are calculated with fitted hyperbolic decline model in Fig. 41)

6.2.2 Regression Models

In this study, some relationships between the permeability, flowrate, pressure drop, and time have been studied based on simulated production data from Eclipse E300 for the

reservoir discussed above. The time required to reach a certain average reservoir pressure provided the same pressure drawdown is an inverse relationship between the permeability and time for a certain pressure drop as shown in Eq. 6.1.

$$t = \frac{a}{k^b} \tag{6.1}$$

Where, t represents time, k represents the average permeability. The fitting models for the given data are shown in **Fig.44**.

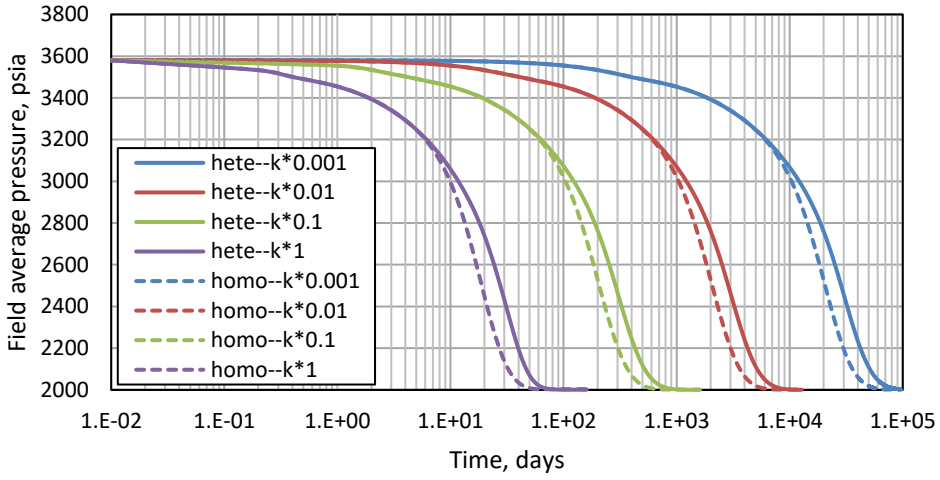

Fig. 44 Field average pressure versus time with different permeability systems

For the heterogeneous case, the value of parameter a is 2678 and b is 0.997, and the R-squared for the fitting model is 0.9873. For the homogeneous case, the value of parameter a is 2418 and b is 0.996, and the R-squared for the fitting model is almost 1.0.

I also found a correlation between the dimensionless flowrate and dimensionless pressure, and between the dimensionless pressure and time, which are shown below:

$$\frac{q}{q_i} = a \ln\left(1 - \frac{p}{p_i}\right) - b \tag{6.2}$$

$$1 - \frac{p}{p_i} = ct^2 + dt + e \tag{6.3}$$

The constant a, b, c, d and e in Eq. 6.2 and Eq. 6.3 are related to the permeability. The fitting plots are shown in **Fig. 45**, and the values of the constants for the fitting models are shown in **Table 20**.

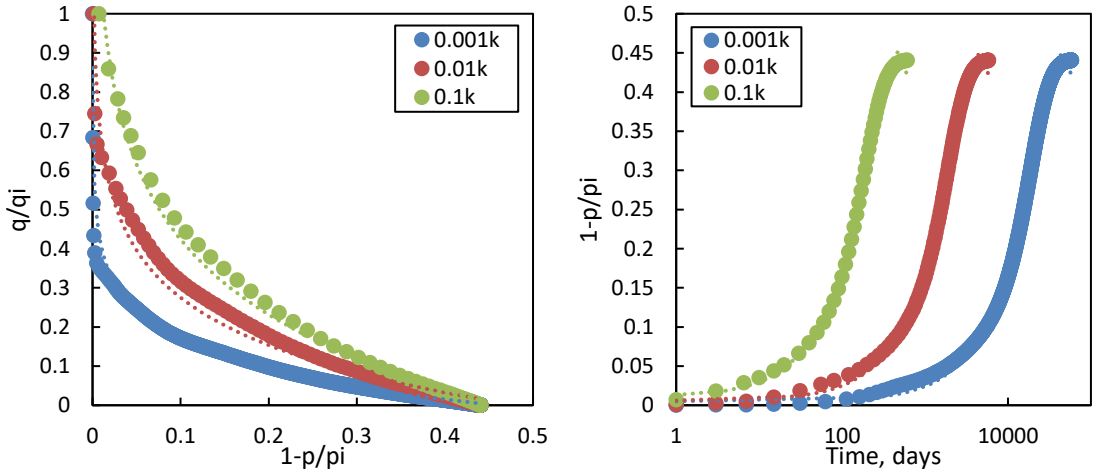

Fig. 45 Fitting plots of the relationship between the dimensionless flowrate, dimensionless pressure, and time (data for the cases without capillary pressure obtained from Eclipse compositional simulator)

Table 20 Values of the constants for the fitting models in Fig. 43

Case	*a*	*b*	*c*	*d*	*e*	R^2 *for Eq. 6.2 and 6.3*
#1(0.001k)	-0.277	0.2147	-2×10^{-10}	2×10^{-5}	0.005	0.99/0.99
#2(0.01k)	-0.175	0.1274	-2×10^{-8}	2×10^{-4}	0.006	0.97/1.00
#3(0.1k)	-0.106	0.0818	-2×10^{-6}	2×10^{-3}	0.011	0.98/0.99

By incorporating these fitting models into the mechanistic model, the production performance with decreasing pressure could be translated those with time. The comparison of the oil and gas recovery factors vs. time by the mechanistic model and Eclipse E300 for

these three cases are shown in **Fig. 46**. It can be observed mechanistic model with the regression models shows a good match with the commercial simulators.

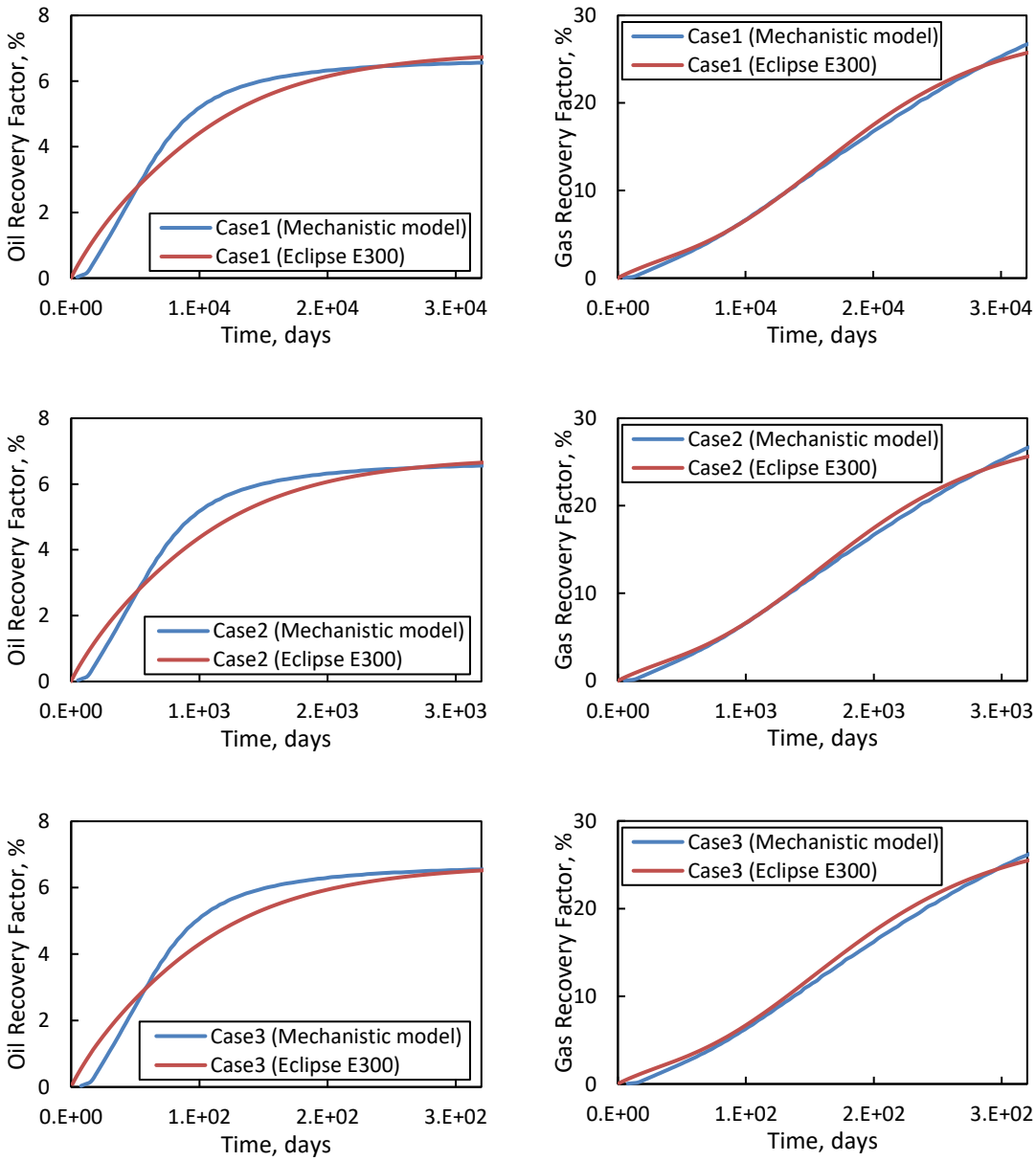

Fig. 46 Comparison of the predicted oil and gas recovery factors vs. time by the mechanistic model and Eclipse E300 for the cases with different permeability, respectively

6.2.3 Basic Fluid Flow Equation in Porous Media

In addition to the decline curves and regression correlations, another way to incorporate time and flowrates to the mechanistic model is by using the basic fluid flow equations in porous media. In this study, Darcy's Law is applied to the mechanistic model. Assuming the flowrate with a certain small pressure drop is a constant, the Darcy's Law can be written as follows:

$$q_o = 6.3282873 \times 10^{-3} \frac{k_{ro} k A \Delta p}{\mu_o} \tag{6.4}$$

$$q_g = 6.3282873 \times 10^{-3} \frac{k_{rg} k A \Delta p}{\mu_g} \tag{6.5}$$

With the mechanistic model, the excess volume, oil and gas viscosities and relative permeabilities for each depletion step have been calculated or obtained. Thus, the time for each depletion step can be calculated with the equations below.

$$V_{excess} = V_o + V_g = (q_o + q_g)t \tag{6.6}$$

$$t = \frac{V_{excess}}{q_o + q_g} \tag{6.7}$$

Here, the cases in Huang et al. (2019) were used to compare the results from our model and compositional simulator. The simulation is conducted in a fractured 1D stimulated reservoir model, and the well is located in the middle, which is constrained by a constant bottom-hole pressure, which is shown below.

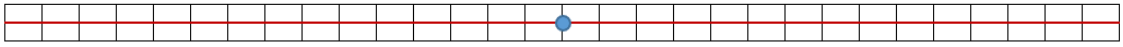

Fig. 47 Fractured shale reservoir model for case study (red line is hydraulic fracture, blue point is the well)

The basic parameters of this reservoir are shown in **Table 21.** A 3-pore-size model is used, and the porosity of each pore size is calculated based on its pore volume fraction, and permeability of each pore size is obtained by a correlation between pore size, porosity and permeability as following: (Aguilera, 2014).

$$k = 100\phi\left(\frac{0.001D_p}{5.33}\right)^{\frac{1}{0.45}} \tag{6.8}$$

Where, D_p is pore diameter. The petrophysical properties of these pores are summarized in **Table 22**.

Table 21 Basic parameters for fractured shale reservoir model

Initial Pressure (psia)	3500
Initial Temperature (°F)	165
Produced BHP (psia)	2000
Matrix	
Porosity	0.08
Grid number	30×1×1
Grid size (ft)	50×50×50
Hydraulic Fracture	
Fracture number	1
Fracture half length (ft)	750
Fracture permeability (mD)	10000
Fracture width (ft)	0.05

Table 22 Petrophysical properties of different pore sizes

Parameter	3-pore-size model		
Diameter/PV fraction	18.6nm (67%)	58.6nm (15%)	116.7nm (18%)
Porosity	0.0536	0.012	0.0144
Permeability (mD)	0.0001856	0.0005324	0.002953

The 5-component fluid model used here is calibrated from the same volatile oil sample in chapter 4. The properties of compositions and the binary interaction coefficients are shown below.

Table 23 Composition data of 5-component fluid model (Reprinted from Huang 2019)

Components	Mol%	MW	Tc, °F	Pc, psia	ω	Volume shifts	Parachor
CO_2	0.192	44.01	87.89	1069.87	0.22	-0.062	78.00
N_2+C_1	50.31	16.26	-120.18	661.78	0.01	-0.194	76.18
C_2-C_3	13.92	35.83	148.59	661.59	0.13	-0.126	130.62
C_4-C_6	10.47	69.32	371.24	492.99	0.24	-0.050	227.18
C_{7+}	25.10	198.88	811.47	277.38	0.76	0.047	785.52

Table 24 Binary interaction coefficient of 5-component fluid model (Reprinted from Huang 2019)

Components	CO_2	N_2+C_1	C_2-C_3	C_4-C_6	C_{7+}
CO_2	-	0	0	0	0
N_2+C_1	0	-	0	0	0
C_2-C_3	0	0	-	0	0
C_4-C_6	0	0	0	-	0.009
C_{7+}	0	0	0	0.009	-

The relative permeability curves for this case are shown in **Fig. 48**. Also, both cases are conducted with and without capillary pressure using a 30° wettability angle.

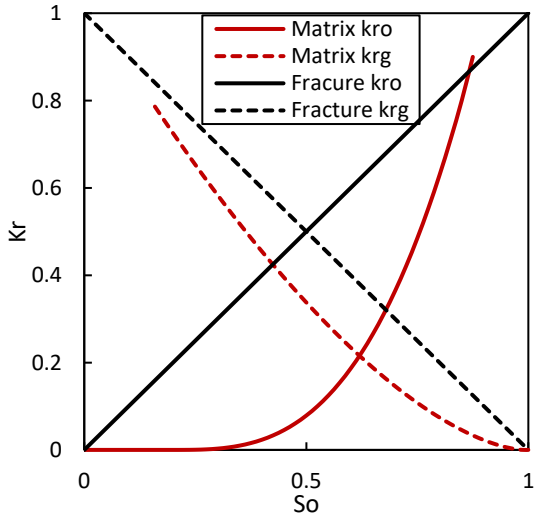

Fig. 48 Oil and gas relative permeability in matrix and fracture (Reprinted from Huang 2019)

The comparison of the oil and gas recovery factors by the mechanistic model (MM) and compositional simulation (CS) for this case are shown in **Fig. 49**.

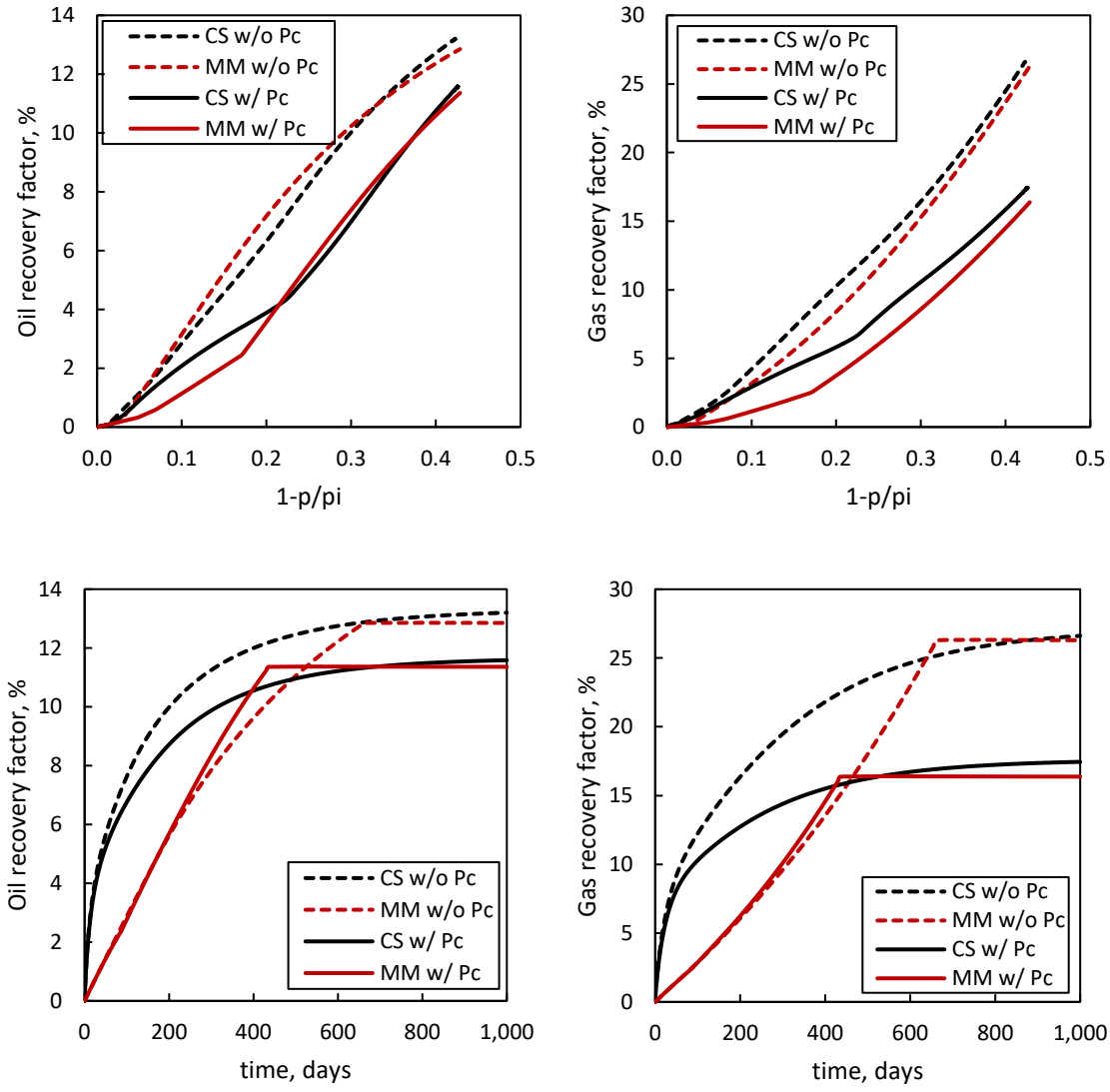

Fig. 49 Comparison of reservoir performance using mechanistic model (MM) and compositional simulator (CS) with 3-pore-size model with capillary pressure (solid line) and without capillary pressure (dash line), respectively. (The above two figures are in dimensionless pressure scale, and the bottom two figures are in time scale)

It can be observed that the results by mechanistic model are shown great match with those by compositional simulation when capillary pressure is considered or not in the dimensionless pressure scale. While in time scale, the oil recovery factors match better than the gas recovery factor, and both of them are good matched at late time. The time shifts between mechanistic model and compositional simulator is mainly coming from different pressure drawdown. For the mechanistic model, the pressure drawdown is a constant, while the pressure drawdown in the compositional simulator is very large at early time and becomes very smaller in the late time, which can be seen in the **Fig. 50**.

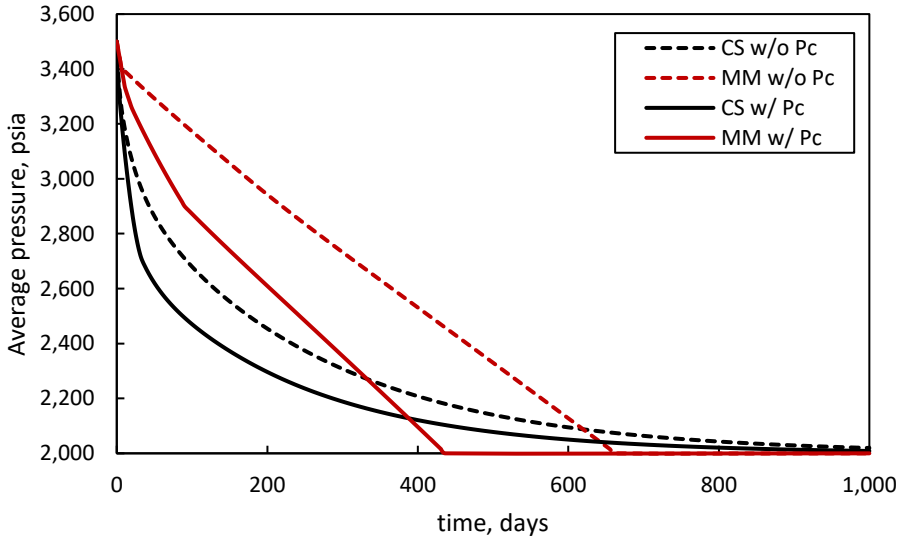

Fig. 50 Comparison of average pressure using mechanistic model (MM) and compositional simulator (CS) with 3-pore-size model with capillary pressure (solid line) and without capillary pressure (dash line), respectively.

CHAPTER VII

DISCUSSION AND CONCLUSIONS

Unconventional shale and tight reservoirs have contributed over 60% oil and 70% gas of total U.S. production these years. As well known, phase behavior of the fluid in unconventional reservoir is quite different from that in conventional reservoir. And the variation of the thermodynamic and transport properties of fluids has a significant impact on the well performance and ultimate recovery of unconventional reservoirs. Therefore, an effective and reliable method to investigate and predict the impact of confinement effect on well performance and ultimate recovery of unconventional reservoirs is necessary and of great importance.

In this study, we developed a mechanistic model of depletion and injection for well performance prediction of unconventional reservoirs in Chapter 3. We incorporated capillary pressure and pore size distribution to simulate confinement effect in unconventional reservoirs.

In Chapter 4, a new protocol for quality control test of differential liberation experiments was developed based on material balance, which included a forward scheme and a backward scheme and Hoffman consistence checks. Based on the results from this QC test, uncertainties of the experimental data were determined mostly in the plus fraction molecular weight and measurement of N_2. N_2 can be lumped with CH_4 as a pseudo-component to eliminate the uncertainty from the measurement of N_2 since N_2 usually comes from the sampling technique. And a proper description of the physical properties

of the plus fractions is essential for reliable phase behavior and compositional modelling studies. According to the hydrocarbon calibration procedures learned from the predecessors in this study, a 6-component fluid model was developed for a volatile oil from an anonymous oilfield in North America. Also, the pore size distribution models were developed with cumulative distribution function and a new assignment method of representative pore sizes for a sample from the same anonymous oilfield in North America.

With the developed mechanistic model, fluid model and pore size distribution models, we conducted a series of sensitivity analysis to investigate the impact of depletion and injection variables. The effect of capillary pressure, production modes and pore size distribution were investigated for both depletion and injection. Additionally, the effect of pressure decline steps, wettability angle for depletion, injection dose per step, bottom-hole pressure (BHP), and injection fluid distribution for injection were investigated. A summary of the conclusions from this analysis are shown below.

(1) Two extreme boundaries of the production performance were predicted by the mechanistic model: constant composition (CC) production mode is the most optimistic production mode, while the preferential gas (PG) production mode is the most pessimistic production mode. The relative permeability (RP) production mode is the realistic production mode with provided wettability angle, and the production performance under RP mode is located between these two boundaries and moving with different relative permeability curves. For depletion under RP production mode, the oil recovery factor with capillary

pressure is lower than that without capillary pressure when the pressure is still higher than the bubble point. However, as pressure fall below the bubble point for all pore sizes, the oil recovery factor considering capillary pressure is higher than when it is neglected. The gas recovery factor with capillary pressure is always lower than that without capillary pressure. And the residual oil is lighter when capillary pressure is considered.

(2) The oil recovery factor changes significant while the gas recovery factor is not as number of pore sizes increase until they converge for a number of pores of 5, indicating that only one pore size to represent the reservoir is not reasonable, while the number of pores required is usually lower than 5. The fact that bubble point pressure decreases as the pore size decreases at constant temperature, is resulting that the fluid in smaller pores remains in liquid phase for pressure lower than the bulk bubble point pressure. Once the fluid in pores fall into two-phase region, the excess volume increases dramatically, resulting in a significant increase in oil production. And smaller pores achieve higher oil recovery factor and lower gas recovery. The residual oil in smaller pores is lighter than the oil left in larger pores.

(3) Decreasing of the pressure decline steps results in a significant increase of the oil recovery factor and negligible decrease in the gas recovery factor until they converge to the ultimate recovery factor on a specified pressure. And when wettability angle changes from 30° to 60°, the mobility of the oil is not affected for both 1-pore-size and 10-pore-size models, and the mobility of the gas

decreases for 1-pore-size model while that is not affected for 10-pore-size model. The oil recovery factor decreases while the gas recovery factor increases as wettability angle increases. The big difference is the GOR due to the existence of macro pores which counteract the confinement effect. And the residual oil becomes heavier as wettability angle increases.

(4) The oil recovery factor increases, and the gas recovery factor decreases when capillary pressure is taken into consideration for the CO_2 injection. A larger percentage of N2C1 and lower percentage of CO_2 and heavier components in the residual oil when capillarity is considered. And the pore size distribution models have negligible effect on the oil and gas recovery factors for CO_2 injection due to the similar miscibility between the residual fluid and CO_2 among all the pore sizes, which suppresses the differences of capillarity impacts between different pore size distribution models. Under preferential gas production mode, higher oil recovery factor, lower gas recovery factor, and significant oil production delay are observed in smaller pores.

(5) Both oil and gas recovery factors increase as injection dose per step decreases until they converged to the ultimate recovery factors on a specified pressure. And the lower injection rate of CO_2 could achieve higher oil and gas production and CO_2 sequestration.

(6) Under preferential gas production mode, the ultimate oil recovery factor as 1.2 pore volume CO_2 is injected increases dramatically as BHP increases. However, more CO_2 is needed to achieve the same pore volume injection as

BHP increase. The ultimate gas recovery factor as 1.2 pore volume CO_2 is injected is barely affected by the increased BHP. But the efficiency of the injection to improve the gas recovery is increasing dramatically as BHP increases.

(7) Two different injection fluid distribution models, pore volume model and pore opening model, are built in the mechanistic model for injection. With the pore size distribution data in this study, more CO_2 is injected into the smaller pores with pore opening model than that with pore volume model since a larger number of smaller pores exists in the system. The oil recovery factor with pore volume model is much higher than that with pore opening model. And the gas recovery factor with pore volume model is a little higher than that with pore opening model. A larger percentage of CO_2 and lower percentage of other components in the residual oil with pore volume model comparing to those with pore opening model. But in reality, we do not really know which would be the distribution mode.

In Chapter 6, the application of this mechanistic model for the field use is discussed. First of all, the mechanistic model could provide a rapid prediction of the ultimate oil and gas recovery as the average pressure of the whole reservoirs declines from the initial pressure to the bottom-hole pressure for both conventional and unconventional reservoirs. Secondly, the mechanistic model can be applied for well production performance prediction with time scales by incorporating pressure-time-flowrate translating methods. Three different methods are introduced in this study, which are

decline curve method, regression model method, and basic fluid flow model method. With these methods, the production performance predicted by mechanistic model on pressure scale can be translated to time scale, which can be generally used for the oil industry.

The advantages of the developed mechanistic model are as following:

(1) It could give a rapid prediction and estimation of the production performance especially for unconventional reservoirs by incorporating the capillary pressure and pore size distribution.

(2) It also could give a rapid prediction and estimation of the production performance changing with different operation conditions, which is of vital importance in the field operation to optimize the production process.

(3) The sensitivity analysis with the mechanistic model could provide the selection of reasonable parameters for reservoir simulation rapidly, such as pore size distribution model, depletion decline steps, injection dose per step and BHP, etc.

(4) This mechanistic model could provide two extreme boundaries of the production performance, as well as provide two different injection fluid distribution model, which can be used as a guidance for other reservoir simulation method.

The main limitation of the developed mechanistic model is that it does not include fluid flow model depending on the geological properties and well designs for the reservoirs.

REFERENCES

Aktiengesellschaft, L., 2017. Miscible Solent Enhanced Oil Recovery. *Patent*, US20170292059A1

Alfarge, D., Wei, M. and Bai, B., 2017, April. IOR methods in unconventional reservoirs of North America: comprehensive review. In *SPE Western Regional Meeting*. Society of Petroleum Engineers.

Alfarge, D., Wei, M. and Bai, B., 2018. CO_2-EOR mechanisms in huff-n-puff operations in shale oil reservoirs based on history matching results. *Fuel*, *226*, pp.112-120.

Alfi, M., Nasrabadi, H. and Banerjee, D., 2016. Experimental investigation of confinement effect on phase behavior of hexane, heptane and octane using lab-on-a-chip technology. *Fluid Phase Equilibria*, *423*, pp.25-33.

Alfi, M., Nasrabadi, H. and Banerjee, D., 2017, October. Effect of confinement on bubble point temperature shift of hydrocarbon mixtures: Experimental investigation using nanofluidic devices. In *SPE Annual Technical Conference and Exhibition*. Society of Petroleum Engineers.

Alharthy, N.S., Nguyen, T., Teklu, T., Kazemi, H. and Graves, R., 2013, September. Multiphase compositional modeling in small-scale pores of unconventional shale reservoirs. In *SPE Annual Technical Conference and Exhibition*. Society of Petroleum Engineers.

Ambrose, R.J., Hartman, R.C., Diaz Campos, M., Akkutlu, I.Y. and Sondergeld, C., 2010, January. New pore-scale considerations for shale gas in place calculations. In *SPE unconventional gas conference*. Society of Petroleum Engineers.

Ball, P.C. and Evans, R., 1989. Temperature dependence of gas adsorption on a mesoporous solid: capillary criticality and hysteresis. *Langmuir*, *5*(3), pp.714-723.

Barbosa, G.D., Travalloni, L., Castier, M. and Tavares, F.W., 2016. Extending an equation of state to confined fluids with basis on molecular simulations. *Chemical Engineering Science*, *153*, pp.212-220.

Bashbush, J.L., 1981, January. A method to determine K-values from laboratory data and its applications. In *SPE Annual Technical Conference and Exhibition*. Society of Petroleum Engineers.

Behrens, R.A. and Sandler, S.I., 1988. The use of semicontinuous description to model the C7+ fraction in equation of state calculations. *SPE reservoir engineering*, *3*(03), pp.1-041.

Bustin, R.M., Bustin, A.M., Cui, A., Ross, D. and Pathi, V.M., 2008, January. Impact of shale properties on pore structure and storage characteristics. In *SPE shale gas production conference*. Society of Petroleum Engineers.

Carrott, M.R., Candeias, A.E., Carrott, P.J.M., Ravikovitch, P.I., Neimark, A.V. and Sequeira, A.D., 2001. Adsorption of nitrogen, neopentane, n-hexane, benzene and methanol for the evaluation of pore sizes in silica grades of MCM-41. *Microporous and mesoporous materials*, *47*(2-3), pp.323-337.

Czernia, B. and Barrufet, M., 2019, September. A Mechanistic Approach for Calculating Oil-Gas Relative Permeability Curves in Unconventional Reservoirs. In *SPE Annual Technical Conference and Exhibition*. Society of Petroleum Engineers.

Derouane, E.G., 2007. On the physical state of molecules in microporous solids. *Microporous and mesoporous materials*, *104*(1-3), pp.46-51.

Devegowda, D., et alet. al., 2012. *Phase Behavior of Gas Condensates in Shales Due to Pore Proximity Effects: Implications for Transport, Reserves, and Well Productivity, Paper SPE, 160099*.

Dong, X., Liu, H., Hou, J., Wu, K. and Chen, Z., 2016. Phase equilibria of confined fluids in nanopores of tight and shale rocks considering the effect of capillary pressure and adsorption film. *Industrial & Engineering Chemistry Research*, *55*(3), pp.798-811.

Eberle, C.M., 2017. *An investigation into surfactant stabilized, non-aqueous and semi-aqueous foam for enhanced oil recovery* (Doctoral dissertation).

Evans, R., 1763. Marini Bettolo Marconi U and Tarazona P 1986 J. Chem. Phys, 84, p.2376.

Hoffman, A.E., Crump, J.S. and Hocott, C.R., 1953. Equilibrium constants for a gas-condensate system. *Journal of Petroleum Technology*, *5*(01), pp.1-10.

Huang, J., Jin, T., Chai, Z., Barrufet, M. and Killough, J., 2019. Compositional simulation of fractured shale reservoir with distribution of nanopores using coupled multi-porosity and EDFM method. *Journal of Petroleum Science and Engineering*, *179*, pp.1078-1089.

Huang, J., Jin, T., Chai, Z., Barrufet, M. and Killough, J., 2020. Compositional simulation of three-phase flow in mixed-wet shale oil reservoir. *Fuel*, *260*, p.116361.

Huang, J., Jin, T., Barrufet, M. and Killough, J., 2020. Evaluation of CO2 injection into shale gas reservoirs considering dispersed distribution of kerogen. *Applied Energy*, *260*, p.114285.

Iino, A., Onishi, T. and Datta-Gupta, A., 2019. Optimizing CO_2-and Field-Gas-Injection EOR in Unconventional Reservoirs Using the Fast-Marching Method. *SPE Reservoir Evaluation & Engineering*.

Jin, B. and Nasrabadi, H., 2016. Phase behavior of multi-component hydrocarbon systems in nano-pores using gauge-GCMC molecular simulation. *Fluid Phase Equilibria*, *425*, pp.324-334.

Jin, B., Bi, R. and Nasrabadi, H., 2017. Molecular simulation of the pore size distribution effect on phase behavior of methane confined in nanopores. *Fluid Phase Equilibria*, *452*, pp.94-102.

Jin, B. and Nasrabadi, H., 2018. Phase behavior in shale organic/inorganic nanopores from molecular simulation. *SPE Reservoir Evaluation & Engineering*, *21*(03), pp.626-637.

Jin, L., Ma, Y. and Jamili, A., 2013, September. Investigating the effect of pore proximity on phase behavior and fluid properties in shale formations. In *SPE Annual Technical Conference and Exhibition*. Society of Petroleum Engineers.

Jin, Z. and Firoozabadi, A., 2016. Phase behavior and flow in shale nanopores from molecular simulations. *Fluid Phase Equilibria*, *430*, pp.156-168.

Jin, Z. and Firoozabadi, A., 2016. Thermodynamic modeling of phase behavior in shale media. *SPE Journal*, *21*(01), pp.190-207.

Katz, D.L., 1983. Overview of phase behavior in oil and gas production. *Journal of Petroleum Technology*, *35*(06), pp.1-205.

Kittaka, S., Morimura, M., Ishimaru, S., Morino, A. and Ueda, K., 2008. Effect of Confinement on the Fluid Properties of Ammonia in Mesopores of MCM-41 and SBA-15. *Langmuir*, *25*(3), pp.1718-1724.

Kuila, U. and Prasad, M., 2013. Specific surface area and pore-size distribution in clays and shales. *Geophysical Prospecting*, *61*(2), pp.341-362.

Langmuir, I., 1918. The adsorption of gases on plane surfaces of glass, mica and platinum. *Journal of the American Chemical society*, *40*(9), pp.1361-1403.

Li, S., Zhang, K., Jia, N. and Liu, L., 2018. Evaluation of four CO_2 injection schemes for unlocking oils from low-permeability formations under immiscible conditions. *Fuel*, *234*, pp.814-823.

Li, Z., Jin, Z. and Firoozabadi, A., 2014. Phase behavior and adsorption of pure substances and mixtures and characterization in nanopore structures by density functional theory. *SPE Journal*, *19*(06), pp.1-096.

Liu, Y., Jin, Z. and Li, H.A., 2018. Comparison of Peng-Robinson equation of state with capillary pressure model with engineering density-functional theory in describing the phase behavior of confined hydrocarbons. *SPE Journal*.

Lohrenz, J., Bray, B.G. and Clark, C.R., 1964. Calculating viscosities of reservoir fluids from their compositions. *Journal of Petroleum Technology*, *16*(10), pp.1-171.

Luo, S., Nasrabadi, H. and Lutkenhaus, J.L., 2016. Effect of confinement on the bubble points of hydrocarbons in nanoporous media. *AIChE Journal*, *62*(5), pp.1772-1780.

Luo, S., Lutkenhaus, J.L. and Nasrabadi, H., 2016. Confinement-induced supercriticality and phase equilibria of hydrocarbons in nanopores. *Langmuir*, *32*(44), pp.11506-11513.

Luo, S., Lutkenhaus, J.L. and Nasrabadi, H., 2018. Use of differential scanning calorimetry to study phase behavior of hydrocarbon mixtures in nano-scale porous media. *Journal of Petroleum Science and Engineering*, *163*, pp.731-738.

Luo, S., Lutkenhaus, J.L. and Nasrabadi, H., 2019. Experimental study of pore size distribution effect on phase transitions of hydrocarbons in nanoporous media. *Fluid Phase Equilibria*, *487*, pp.8-15.

Luo, S., Jin, B., Lutkenhaus, J.L. and Nasrabadi, H., 2019. A novel pore-size-dependent equation of state for modeling fluid phase behavior in nanopores. *Fluid Phase Equilibria*.

Nelson, P.H., 2009. Pore-throat sizes in sandstones, tight sandstones, and shales. *AAPG bulletin*, *93*(3), pp.329-340.

Nojabaei, B., Johns, R.T. and Chu, L., 2013. Effect of capillary pressure on phase behavior in tight rocks and shales. *SPE Reservoir Evaluation & Engineering*, *16*(03), pp.281-289.

Parsa, E., Yin, X. and Ozkan, E., 2015, September. Direct observation of the impact of nanopore confinement on petroleum gas condensation. In *SPE Annual Technical Conference and Exhibition*. Society of Petroleum Engineers.

Pedersen, K.S., Thomassen, P. and Fredenslund, A., 1983. SRK-EOS calculation for crude oils. *Fluid Phase Equilibria*, *14*, pp.209-218.

Pedersen, K. S.; Fredenslund, Aa.; Thomassen, P., 1989. Properties of Oils and Natural Gases. *Book Published by Gulf Publishing Company, Houston*. pp. 1–252.

Peng, B. and Yu, Y.X., 2008. A density functional theory with a mean-field weight function: applications to surface tension, adsorption, and phase transition of a Lennard-Jones fluid in a slit-like pore. *The Journal of Physical Chemistry B*, *112*(48), pp.15407-15416.

Peng, D. and Robinson, D.B., 1976. A New Two-Constant Equation of State, *Industrial and Engineering Chemical Fundamentals*, vol. 15. pp. 59-64.

Pommer, M.E., 2014. *Quantitative assessment of pore types and pore size distribution across thermal maturity, Eagle Ford Formation, South Texas* (Doctoral dissertation).

Qiao, S.Z., Bhatia, S.K. and Nicholson, D., 2004. Study of hexane adsorption in nanoporous MCM-41 silica. *Langmuir*, *20*(2), pp.389-395.

Rachford, H.H. and Rice, J.D., 1952. Procedure for Use of Electrical Digital Computers in Calculating Flash Vaporization Hydrocarbon Equilibrium, *Journal of Petroleum Technology*, Technical Note 136, vol.19.

Ren, B., Ren, S., Zhang, L., Chen, G. and Zhang, H., 2016. Monitoring on CO_2 migration in a tight oil reservoir during CCS-EOR in Jilin Oilfield China. *Energy*, *98*, pp.108-121.

Russo, P.A., Carrott, M.R. and Carrott, P.J.M., 2012. Trends in the condensation/evaporation and adsorption enthalpies of volatile organic compounds on mesoporous silica materials. *Microporous and Mesoporous Materials*, *151*, pp.223-230.

Salahshoor, S., Fahes, M. and Teodoriu, C., 2018. A review on the effect of confinement on phase behavior in tight formations. *Journal of Natural Gas Science and Engineering*, *51*, pp.89-103.

Singh, S.K., Sinha, A., Deo, G. and Singh, J.K., 2009. Vapor− liquid phase coexistence, critical properties, and surface tension of confined alkanes. *The Journal of Physical Chemistry C*, *113*(17), pp.7170-7180.

Stimpson, B.C. and Barrufet, M.A., 2016. Thermodynamic modeling of pure components including the effects of capillarity. *Journal of Chemical & Engineering Data*, *61*(8), pp.2844-2850.

Stimpson, B.C. and Barrufet, M.A., 2016, September. Effects of confined space on production from tight reservoirs. In *SPE Annual Technical Conference and Exhibition*. Society of Petroleum Engineers.

Thommes, M. and Findenegg, G.H., 1994. Pore condensation and critical-point shift of a fluid in controlled-pore glass. *Langmuir*, *10*(11), pp.4270-4277.

Thommes, M., Köhn, R. and Fröba, M., 2002. Sorption and pore condensation behavior of pure fluids in mesoporous MCM-48 silica, MCM-41 silica, SBA-15 silica and controlled-pore glass at temperatures above and below the bulk triple point. *Applied surface science*, *196*(1-4), pp.239-249.

Tian, Y., Xiong, Y., Wang, L., Lei, Z., Zhang, Y., Yin, X. and Wu, Y.S., 2019. A Compositional Model for Gas Injection IOR/EOR in Tight Oil Reservoirs Under Coupled Nanopore Confinement and Geomechanics Effects. *Journal of Natural Science and Engineering*, *71*.

Travalloni, L., Castier, M., Tavares, F.W. and Sandler, S.I., 2010. Thermodynamic modeling of confined fluids using an extension of the generalized van der Waals theory. *Chemical Engineering Science*, *65*(10), pp.3088-3099.

Travalloni, L., Castier, M., Tavares, F.W. and Sandler, S.I., 2010. Critical behavior of pure confined fluids from an extension of the van der Waals equation of state. *The Journal of Supercritical Fluids*, *55*(2), pp.455-461.

Travalloni, L., Castier, M. and Tavares, F.W., 2014. Phase equilibrium of fluids confined in porous media from an extended Peng–Robinson equation of state. *Fluid Phase Equilibria*, *362*, pp.335-341.

Walton, J.P.R.B. and Quirke, N.P.R.B., 1989. Capillary condensation: a molecular simulation study. *Molecular Simulation*, *2*(4-6), pp.361-391.

Wang, L. and Yu, W., 2019. Mechanistic simulation study of gas Puff and Huff process for Bakken tight oil fractured reservoir. *Fuel*, *239*, pp.1179-1193.

Wang, S., Feng, Q., Javadpour, F., Xia, T. and Li, Z., 2015. Oil adsorption in shale nanopores and its effect on recoverable oil-in-place. *International Journal of Coal Geology*, *147*, pp.9-24.

Wang, Y., Yan, B. and Killough, J., 2013, September. Compositional modeling of tight oil using dynamic nanopore properties. In *SPE Annual Technical Conference and Exhibition*. Society of Petroleum Engineers.

Xiong*, Y., Winterfeld, P. and Wu, Y., 2014, August. Coupled geomechanics and pore confinement effects for modeling unconventional shale reservoirs. In *Unconventional Resources Technology Conference, Denver, Colorado, 25-27 August 2014* (pp. 2223-2233). Society of Exploration Geophysicists, American Association of Petroleum Geologists, Society of Petroleum Engineers.

Yang, Q., Jin, B., Banerjee, D. and Nasrabadi, H., 2019. Direct visualization and molecular simulation of dewpoint pressure of a confined fluid in sub-10 nm slit pores. *Fuel*, *235*, pp.1216-1223.

Yu, W., Lashgari, H.R., Wu, K. and Sepehrnoori, K., 2015. CO_2 injection for enhanced oil recovery in Bakken tight oil reservoirs. *Fuel*, *159*, pp.354-363.

Zarragoicoechea, G.J. and Kuz, V.A., 2004. Critical shift of a confined fluid in a nanopore. *Fluid phase equilibria*, *220*(1), pp.7-9.

Zhang, F., Adel, I.A., Park, K.H., Saputra, I.W.R. and Schechter, D.S., 2018, September. Enhanced Oil Recovery in Unconventional Liquid Reservoir Using a Combination of CO2 Huff-n-Puff and Surfactant-Assisted Spontaneous Imbibition. In *SPE Annual Technical Conference and Exhibition*. Society of Petroleum Engineers.

Zhang, Y., Civan, F., Devegowda, D. and Sigal, R.F., 2013, September. Improved prediction of multi-component hydrocarbon fluid properties in organic rich shale reservoirs. In *SPE Annual Technical Conference and Exhibition*. Society of Petroleum Engineers.

Zhou, X., Yuan, Q., Zhang, Y., Wang, H., Zeng, F. and Zhang, L., 2019. Performance evaluation of CO2 flooding process in tight oil reservoir via experimental and numerical simulation studies. *Fuel*, *236*, pp.730-746.

Zuloaga, P., Yu, W., Miao, J. and Sepehrnoori, K., 2017. Performance evaluation of CO_2 Huff-n-Puff and continuous CO2 injection in tight oil reservoirs. *Energy*, *134*, pp.181-192.